Fixed-scale statistics and the geometry of turbulent dispersion at high Reynolds number via numerical simulation

A Thesis
Presented to
The Academic Faculty

by

Jason F. Hackl

In Partial Fulfillment
of the Requirements for the Degree
Doctor of Philosophy

School of Aerospace Engineering
Georgia Institute of Technology
August 2011

Fixed-scale statistics and the geometry of turbulent dispersion at high Reynolds number via numerical simulation

Approved by:

Prof. Pui-Kuen Yeung, Advisor
School of Aerospace Engineering
Georgia Institute of Technology

Prof. Suresh Menon
School of Aerospace Engineering
Georgia Institute of Technology

Prof. Michael Schatz
School of Physics
Georgia Institute of Technology

Prof. Mitchell Walker
School of Aerospace Engineering
Georgia Institute of Technology

Prof. Donald Webster
School of Civil and Environmental Engineering
Georgia Institute of Techonology

Date Approved: 5 May 2011

ACKNOWLEDGEMENTS

This work was supported by the National Science Foundation through grant numbers CBET-0328314 and 0553867 as well as an International Research and Education in Engineering (IREE) supplement that enabled the author to spend three months at Monash University, Australia in the summer of 2008. We are deeply grateful for the supercomputing resources, which enabled all the computations reported in this work, provided by the National Center for Computational Science at Oak Ridge National Laboratory as well as the following partners in the TeraGrid consortium: the National Institute for Computational Sciences (NICS) at the University of Tennessee, the Texas Advanced Computing Center (TACC) at the University of Texas at Austin, the Pittsburgh Supercomputing Center (PSC), and the San Diego Supercomputer Center (SDSC) at the University of California, San Diego.

I thank Prof. P. K. Yeung for his years of kindness, diligent help and patient guidance in training me as a researcher. His discipline and attentiveness to detail are model traits that I aspire to in my daily life and work. He provided fantastic opportunities to meet and work with leaders in our field of research, notably Prof. Brian L. Sawford at Monash University. I am grateful to Prof. Sawford for his hospitality during my visit to Monash University. I thank him for his fine example as a scientist and patient interaction with me, which taught me so much about how to think my way through a research problem, understand the physics driving the statistical results, check the correctness of computations and derivations, and present them concisely and clearly to a broad audience. Publishing with him has been a pleasure and a great honor. Discussions with Drs. M. Borgas, E. Bodenschatz, and N. Ouellette were valuable and informative, and I thank them for their attention and time.

I thank Profs. S. Menon, M. Walker, D. R. Webster, and M. Schatz for taking the time to serve on my committee and review my work. I am very grateful for the companionship

and counsel of my coworkers during my time in graduate school especially Drs. M. Sanchez-Rocha, K. Kemenov, A. G. Gungor, B. Fryxell, and K. Miki, my labmate Kartik Iyer, and my predecessor Prof. D. Donzis. They all taught me a lot and added a great deal of joy to the experience. The funding and support of Prof. J. Jagoda was invaluable during some rough spots at the start of my graduate studies.

I gratefully acknowledge many people who gave a tremendous amount of support and comfort to sustain me personally during a period of great growth and change in my life and my attitude towards it. Dr. Nelson Binggeli of the Georgia Tech Counseling Center and Fr. Tim Hepburn of the Georgia Tech Catholic Center provided separate and invaluable insight into using tools I needed to grow. I have been blessed by the ministry and counsel of Frs. John Matejek and Charles Byrd of the Archdiocese of Atlanta.

My family turned to me even when I had trouble turning to them. My grandparents A. J. and Christine Hackl provided financial security during my graduate studies. I thank them for their love and understanding of this undertaking. My aunt Martha Smith and uncle Dr. Stephen Smith, MD, were an unshakable rock during my time at Georgia Tech, and I cannot overstate my gratitude for the safe place and open arms they always provided me. My parents, Fred and Marita, and my sister Karen always uplifted me with their love and concern, and never let my discouragement or worry outweigh their encouragement and hope.

Most of all, I cling to my wife Cathy. Her love has turned my night into day, opened my eyes and ears to the beauty and wonder around me, and given me a shining star on Earth, our daughter Christine Marie. I promise them that this thesis is only the beginning of what I hope to give them in gratitude for the life God gives me through them.

TABLE OF CONTENTS

LIST OF TABLES

LIST OF FIGURES

LIST OF SYMBOLS OR ABBREVIATIONS

$\langle\varepsilon\rangle$	Suitable average of spatial energy dissipation rate.
CLS	Cubed-local-slope.
η	Kolmogorov length scale $\left(\nu^3/\langle\varepsilon\rangle\right)^{1/4}$.
g	Richardson's constant.
M	Number of MPI tasks (processors).
N_P	Number of particles.
ν	Kinematic viscosity.
r_0	Initial separation distance along coordinate axes.
σ_u	Root-mean-square of one Eulerian velocity component.
t_0	Batchelor time scale $(r_0^2/\langle\varepsilon\rangle)^{1/3}$.
τ_η	Komogorov time scale $(\nu/\langle\varepsilon\rangle)^{1/2}$.
T_L	Lagrangian integral time scale.
$T_{\textbf{sim}}$	Simulation duration.

SUMMARY

The relative dispersion of one fluid particle with respect to another is fundamentally related to the transport and mixing of contaminant species in turbulent flows. The most basic consequence of Kolmogorov's 1941 similarity hypotheses for relative dispersion, the Richardson-Obukhov law that mean-square pair separation distance $\langle r^2 \rangle$ grows with the cube of time t^3 at intermediate times in the inertial subrange, is notoriously difficult to observe in the environment, laboratory, and direct numerical simulations (DNS). Inertial subrange scaling in size parameters like $\langle r^2 \rangle$ requires careful adjustment for the initial conditions of the dispersion process as well as a very wide range of scales (high Reynolds number) in the flow being studied. However, the statistical evolution of the shapes of clusters of more than two particles has already exhibited statistical invariance at intermediate times in existing DNS. This invariance is identified with inertial-subrange scaling and is more readily observed than inertial-subrange scaling for the seemingly simpler quantity $\langle r^2 \rangle$.

Results from dispersion of clusters of four particles (called tetrads) in large-scale DNS at grid resolutions up to 4096^3 and Taylor-scale Reynolds numbers R_λ from 140 to 1000 are used to explore the question of statistical universality in measures of the size and shape of tetrahedra in homogeneous isotropic turbulence in distinct scaling regimes at very small times (ballistic), intermediate times (inertial) and very late times (diffusive). Derivatives of $\langle r^2 \rangle^{1/3}$ with respect to time normalized by the characteristic time scale at the initial tetrad size r_0 constitute a powerful technique in isolating t^3 scaling in $\langle r^2 \rangle$. This technique is applied to the eigenvalues of a moment-of-inertia-like tensor formed from the separation vectors between particles in the tetrad. Estimates of the proportionality constant g in the Richardson-Obukhov t^3 law from DNS at $R_\lambda \approx 1000$ converge towards the value $g \approx 0.56$ reported in previous studies. The exit time taken by a particle pair to first reach successively larger thresholds of fixed separation distance is also briefly discussed and found to have unexplained dependence on initial separation distance for negative moments, but good

inertial range scaling for positive moments. The use of diffusion models of relative dispersion in the inertial subrange to connect mean exit time to g is also tested and briefly discussed in these simulations.

Mean values and probability density functions of shape parameters including the triangle aspect ratio w, tetrahedron volume-to-gyration radius ratio $V^{2/3}/R^2$ and normalized moment-of-inertia eigenvalues are all found to approach invariant forms in the inertial subrange for a wider range of initial separations than size parameters such as mean-square gyration radius. These results constitute the clearest evidence to date that turbulence has a tendency to distort and elongate multiparticle configurations more severely in the inertial subrange than it does in the diffusive regime at asymptotically late time. Triangle statistics are found to be independent of initial shape for all time beyond the ballistic regime.

The development and testing of different schemes for parallelizing the cubic spline interpolation procedure for particle velocities needed to track particles in DNS is also covered. A "pipeline" method of moving batches of particles from processor to processor is adopted due to its low memory overhead, but there are challenges in achieving good performance scaling.

CHAPTER I

INTRODUCTION

1.1 Background

The natural world and technological devices are replete with turbulent flows of fluids under conditions in which compressibility may be neglected. Examples in planetary atmospheres, bodies of water, low-speed flows around terrain, cities and vehicles, and inside engines, pumps and pipes are almost unavoidable. The turbulence of these flows greatly enhances the rate at which contaminants spread out into the environment as well as the mixing of diffusive species in industrial machinery and environmental flows.

Turbulent flows are characterized by a range of fluctuating scales of motion whose dynamic behavior and interactions with one another appear to be random or chaotic, yet are clearly statistically repeatable [3, 4]. The same is true for the scalar transport and mixing these flows accomplish. Statistical repeatability does not imply predictability; there is not yet a reliable, mathematically closed statistical theory of turbulence that produces distributions and moments of any turbulent quantity without appeals to empirically derived models whose applicability is limited to particular flows.

The nonlinearity of the equations of motion for an incompressible fluid, the Navier-Stokes equations, allows instabilities to break large eddies into progressively smaller scales of motion, a cascading process attenuated by viscous dissipation. The Reynolds number $Re = ul/\nu$ may be defined for a given flow characterized by a length and velocity scales l and u (respectively) of a fluid with kinematic viscosity ν. The higher the Reynolds number associated with the scales l and u, the less effective viscous stresses will be at damping motions at these scales. Since viscosity is the principal mechanism inhibiting the cascade of turbulence down to successively smaller scales, the Reynolds number quantifies the range of scales in a turbulent flow. High Reynolds numbers are the rule rather than the exception in almost all turbulent flows in the natural world and in engineering application,

guaranteeing that most of the turbulence will have a very wide range of scales, impairing measurement and defying complete prediction. However, in 1941 Kolmogorov [5] first proposed the hypotheses of local isotropy and statistical universality at the small scales at high Reynolds number. His first hypothesis that, at increasingly higher Reynolds numbers, the small scales of turbulence, regardless of the macroscopic boundary conditions that generate it, tend towards a universal statistical state that is isotropic and determined entirely by the mean dissipation rate and kinematic viscosity has guided turbulence research for seventy years. Kolmogorov's second similarity hypothesis of the existence of the inertial subrange, a regime of intermediate scales in which turbulent statistics, under a similarity transformation, depend only on the mean dissipation rate, has attracted a great deal of attention. The postulated existence of inertial subrange scaling depends on the locality of the cascade of turbulent kinetic energy. Should the inertial subrange exist in actual turbulence at arbitrarily high Reynolds number, it will cover those scales much larger than the small dissipative scales and, simultaneously, much smaller than the energy-containing scales set up by the boundary conditions. If any algebraic statistical relationships in the inertial subrange were universal for all flows at very high Reynolds number, they would greatly simplify the analysis and prediction of these flows.

The Navier-Stokes equations are usually written in an Eulerian framework with respect to a fixed coordinate system through which the fluid moves. It is also possible to study fluid mechanics using a Lagrangian description in which coordinates are attached to labeled volumes of the fluid that are sufficiently small to undergo at most infinitesimal deformations, yet large enough to contain a very large number of molecules [6]. These parcels are referred to as fluid particles, and their contents may be marked and interpreted as a hypothetical scalar admixture in the absence of molecular diffusion. Turbulent mixing of passive scalar contaminants at high Reynolds numbers and high Schmidt numbers $Sc = \nu/D$ (where D is the molecular diffusivity of the passive scalar) is particularly amenable to this Lagrangian description [7]. A fluid particle moves with the Eulerian velocity at the points along its trajectory [8, 9, 10]. Both Eulerian and Lagrangian variables have statistics that exhibit universal scaling under Kolmogorov's hypotheses, and it is interesting to note that some

of the earliest signs of self-similarity in turbulence were observed in Lagrangian statistics well before Kolmogorov's theory of statistical universality was first published [11, 12]. The trajectories of fluid particles are related to the kinematics of the Eulerian field. An interesting mathematical treatise on this matter was presented by Lumley [13] after some specific connections between Eulerian and Lagrangian statistics were made, which we now review along with other important consequences of these connections for the Lagrangian approach to turbulent mixing.

Taylor [11] was the first to consider the problem of turbulent transport of admixtures from the Lagrangian point of view, introducing the Lagrangian velocity autocorrelation function as the diffusion coefficient for the mean-square displacement of independently moving particles taken singly. Later study of backward relative dispersion further demonstrated the relevance of Lagrangian statistics to contaminant mixing problems. Backwards dispersion is the problem of determining the original sources, at some earlier time, of two particles of different scalar concentration that have been observed to approach one another in the course of turbulent mixing. Batchelor [14] showed that the statistical backwards relative dispersion of a single particle can determine the mean field of a contaminant's concentration. Two particles considered jointly can determine the variance of the concentration [15, 16] for arbitrary contaminant source distributions at high Reynolds numbers and low molecular diffusivity. Stochastic difference equations of particles under the action of a specified Eulerian velocity field with measured or otherwise known statistics may be applied as Lagrangian models of scalar contaminants. The Lagrangian stochastic models developed by Thomson [17], Borgas & Sawford [18], Kurbanmuradov & Sabelfeld [19] and Lamorgese *et al.* [20] serve as explanatory examples of work in this field (see also the review by Sawford [7]). Lagrangian stochastic modeling has proved to be a very powerful and flexible tool in environmental mixing problems as well as probability-density-function (PDF) methods in reacting flows (see the review by Pope [21]).

Determining successively higher moments of the concentration field requires joint statistics of more particles, and an illustrative Lagrangian model of high-order multipoint scalar correlations was presented by Frisch *et al.* [22]. Statistical analysis of clusters with more than

two particles provides more information about the shapes clouds of contaminant species will tend to take. Chertkov *et al.* [23] has related the statistics of four-particle clusters, called tetrads, to filtered velocity gradients in order to develop a Lagrangian stochastic model for the velocity gradient tensor. The shapes of multi-particle clusters are driven by the underlying geometric structure of the turbulent field in the Eulerian framework, and knowledge of one can illuminate the other [24, 25, 26].

1.2 Richardson-Obukhov scaling

1.2.1 Theoretical predictions for relative dispersion

There are several predictions that are consistent with Kolmogorov's similarity hypotheses that may be made for each of the Lagrangian configurations discussed in the preceding section. Among the most pivotal is the t^3 law for the mean-squared particle pair separation distance $\langle r^2 \rangle$,

$$\langle r^2 \rangle = g \langle \varepsilon \rangle t^3 \ , \tag{1.1}$$

which, as it was derived by Obukhov [27], is dimensionally consistent with Kolmogorov's hypothesis that statistical scaling relationships are wholly determined by the mean turbulent kinetic energy dissipation rate $\langle \varepsilon \rangle$ in the inertial subrange of intermediate time scales (see also Equation (24.36) in Monin & Yaglom [9]). The proportionality constant g is called Richardson's constant in honor of his 1926 paper [12] in which the cubic time dependence of mean-squared pair separation first emerged from a pioneering effort to model the spreading of atmospheric contaminants and clouds with a diffusion equation. Under Kolmogorov's similarity hypotheses, g is expected to be universal and independent of the large scales at sufficiently high Reynolds number.

Kolmogorov's original similarity hypotheses underpin Equation 1.1, which is henceforth referred to as Richardson-Obukhov scaling. These hypotheses have since been modified [3] to account for intermittency, which is the departure of the turbulent field from space-filling self-similarity. However, because of its linearity in the mean dissipation rate, Richardson-Obukhov scaling does not require corrections for intermittency [7, 28]. This simplifying circumstance has not removed the acute difficulties encountered in observing and assessing

Richardson-Obukhov scaling in environmental measurements, laboratory experiments, and computer simulations of relative dispersion.

1.2.2 How relative dispersion is studied

Dispersion and mixing phenomena in Earth's atmosphere and oceans are practically interesting for many reasons ranging from weather prediction to ecology. Since these environmental flows are the highest-Reynolds-number flows that permit direct measurement of Lagrangian statistics at the present time, they present the widest range of scales to test Kolmogorov's theoretical postulates of local isotropy and the existence of a universal inertial subrange. Satellite telemetry has enabled the collection of time series of the positions of weather balloons [29] in the atmosphere and instrumented buoys in the ocean [30, 31] for increasingly long durations. Further discussion of these fields may be found in the review by Salazar and Collins [32] and the textbook by Bennett [6]. Although the study of flows in the planetary environment is of obvious and immense importance, testing Richardson-Obukhov scaling in these flows is greatly complicated by the plethora of physical processes (such as buoyancy, multiphase phenomena and heat transfer due to solar radiation) that drive these flows. Furthermore, the Earth's surface and terrain impose complex boundary conditions on the atmosphere and oceans, most notably the disparity between small vertical thickness of these bodies and the equatorial and polar circumferences of Earth which make the largest scales in geophysical flows nearly two-dimensional. For these reasons, geophysical flows have persistent inhomogeneity and variability that interferes with the turbulence, even at high Reynolds numbers. Significant intervals of unambiguous t^3 scaling in mean-squared pair separation are not frequently encountered in nature [33, 34]. For this reason efforts to produce more idealized turbulence conditions in the laboratory are necessary to test Richardson-Obukhov scaling in the physical world.

Recent progress in laboratory measurements of relative dispersion has greatly improved the time resolution, particle seeding and labeling, and turbulent field generation of experimental apparatuses. Advanced high-speed imaging techniques developed by Ott & Mann [35] and Voth *et al.* [36] enable the accurate extraction of multiparticle statistics from

large ensembles of minimally-disruptive seed particles added to flows generated by moving grids (see Ott & Mann [35]), counter-rotating baffled disks (see Bourgoin *et al.* [37] and Xu *et al.* [38]) or propellers (described by Lüthi *et al.* [39]) in tanks of water. Trajectory measurements in fully developed turbulence inside these devices require extremely fine time resolution, applying sensing technology originally developed for experiments using subatomic particle accelerators [40]. The experiments reviewed by Toschi & Bodenschatz [41] collected histograms representing probability density functions of several Lagrangian quantities. Measurement of particle trajectories across the full range of time scales in these flows is still a significant challenge, requiring careful attention to noise at the small scales and inhibited by the finite domains of the water tanks at the large scales. As a result, laboratory measurements of turbulent relative dispersion have either been confined to insufficiently large domains or insufficiently long durations for adequate tests of t^3 scaling of mean-squared pair separation distance in three-dimensional turbulence.

The investigative technique used in this work is direct numerical simulation (DNS) on massively parallel supercomputers. Numerical integration of the incompressible Navier-Stokes equations on grids resolving the dissipative scales of turbulence has proved to be a powerful tool (see the review by Moin & Mahesh [42]) that is particularly suitable for extracting Lagrangian data through particle tracking [10]. There is no difficulty in maintaining distinct particle labeling, and particle trajectories may be integrated with the same time accuracy as the scheme for the turbulent velocity field. The most common computational techniques for turbulent flows produce solutions for the Eulerian velocity field at fixed grid points, so the Lagrangian particle velocity must be obtained by interpolating the velocity at grid points onto the position of the particle at each time step. This source of spatial error is straightforward to manage once a robust and accurate numerical method for solving the Navier-Stokes is available. The fine resolution of the small scales in DNS ensures that the motion of tracked particles is driven by the full range of scales in the turbulent flow.

Since the significant difficulties in measuring Lagrangian statistics in actual flows in nature and the laboratory are only now becoming tractable, particle data from computer

simulations have played a key role in the study of Lagrangian statistics starting with some of the very earliest DNS by Riley & Patterson [43]. The DNS of Yeung [44] is a particularly early source of particle data for relative dispersion in isotropic three-dimensional turbulence. Likewise, computed statistics for tetrads of fluid particles were presented in unprecedented detail by Pumir *et al.* [45]. However, the computational cost of DNS (both in the number of operations and storage requirements) grows rapidly with the range of scales that require resolution, and achieving high Reynolds number has always been a challenge in using DNS to test theories such as Richardson-Obukhov scaling. Only recently [46] have simulations at Reynolds numbers comparable to those attained in laboratory settings become possible. Careful attention must also be paid to the large-scale forcing used to sustain the turbulence for sufficient time, and, along with the influence of (usually periodic) boundary conditions, makes large-scale variability a manageable, but significant, concern in DNS.

1.3 Review of historical findings and current challenges

Lagrangian statistics in general (and turbulent relative dispersion in particular) have innate features that are fundamental to the difficulties encountered in testing Kolmogorov's theories through studies in the environment, the laboratory and simulations. Here we discuss the persistent issues and challenges that must be addressed in any study of Lagrangian turbulence and review the development of the state-of-the-art in the current understanding of universality in turbulent relative dispersion. This review necessarily entails references to recent innovations in overcoming these challenges through the use of fixed-scale statistics as well as the interesting and promising features that have been encountered in the study of the statistical geometry of multiparticle clusters.

1.3.1 Challenges in the study of relative dispersion

The chief, but by no means only, challenging trait of relative dispersion is one shared by all Lagrangian statistics: the requirement of a range of scales sufficiently large to credibly permit the existence of an unambiguous inertial subrange. The ratio of Lagrangian integral time scale T_L to small-scale Kolmogorov time τ_η (to be defined in Section 3) grows much more slowly with Reynolds number than any analogous ratios of length scales or time

scales relevant to Eulerian statistics [10]. Should an inertial subrange of a given range of scales exist in Lagrangian statistics, it will require a higher Reynolds numbers for clear observation than a corresponding regime in Eulerian statistics of the same order [47]. Even if a wide range of scales is realized in a particular flow, the number of particles required for adequate sampling grows with Reynolds number as well, imposing further costs on DNS and measurement.

Joint consideration of two or more particles introduces additional requirements for the range of length scales encountered by the dispersing particles. One of Richardson's [12] most fundamental observations was that the relative motion of one particle with respect to another would be driven by scales of motion comparable to their separation. Batchelor [16] interpreted this to mean that an inertial subrange in relative dispersion requires not only that the particles disperse during the inertial subrange in time, but that their separations remain well within the inertial subrange of length scales as well. If these strict conditions are not satisfied, particle pairs that separate rapidly may be affected by nonuniversal large scales at times well before T_L, and particles that stay close together could remain dominated by dissipative scales for times much longer than τ_η.

Even in a flow field with stationary Eulerian statistics, isotropic turbulence always tends to spread particles further and further from one another on average [48]. Since relative dispersion is thus nonstationary, time averaging cannot be used to improve the statistical quality of large-scale parameters, with the most suitable value of $\langle\varepsilon\rangle$ being particularly difficult to determine for use in Equation 1.1 (for a discussion in the context of DNS, see Yeung & Borgas [49]). Although not a direct consequence of nonstationarity, it is well-known that relative dispersion remains correlated to its initial conditions for a significant amount of time. Both Richardson [12] and Obukhov [27] assumed that the t^3 regime of relative dispersion was uncontaminated by initial conditions. Richardson computed solutions of a diffusion equation for the PDF of pair separation distance in the limit of vanishingly small initial separation. Later, Batchelor [16] argued that, at small time, particles move ballistically along rectilinear trajectories set by the Eulerian structure of the flow field at the start of the dispersion until well past one turnover time of eddies at the scale of the initial

separation. Examples of this behavior have been observed in the simulations of Yeung & Borgas [49] and the experiments of Ouellette *et al.* [38].

Thus, finite initial separation imposes yet another requirement on Richardson-Obukhov scaling; there must be adequate separation between this ballistic regime and T_L. In practice, tests for Richardson-Obukhov scaling also respond favorably to adjustments for initial separation at all times in the dispersion. Examples include normalization [35] by initial separation, subtracting off the initial separation [37] and examining the slope of $\langle r^2 \rangle$ in different ways [50]. These techniques are still subjects of ongoing research and assessment. We see that the issue of "memory" of initial conditions and other past events in the dispersion process is a crucial one as well.

1.3.2 Progress in overcoming these challenges

Richardson's constant g has long been notoriously difficult to measure or estimate, and only recently has there been consensus between experiments and simulations about its order of magnitude. As previously noted, environmental observations of t^3 scaling in $\langle r^2 \rangle$ are scarce and complicated by variability or ambiguity in determining $\langle \varepsilon \rangle$, making direct tests of Equation 1.1 difficult. A brief review of notable efforts to determine g from environmental measurements may be found in Section 24.3 in Monin & Yaglom [9] and the introduction to the experimental study of Ott & Mann [35]. These estimates of Richardson's constant range from values as low as $g \approx 0.06$, which is inferred from Tatarskii's [51] observations of fluctuations in the atmosphere's refractive index, to values as high as $g \approx 6$, which is a consequence of a simple empirical fit recommended by Hanna *et al.* [52] for puff diffusion. The difficulty in measuring $\langle \varepsilon \rangle$ in atmospheric flows is the major source of uncertainty in these estimates of Richardson's constant [7]. As stated earlier, the large scales are at least somewhat controllable in experiments (and completely specified in simulations), and the resultant improvements in determining dissipation rate have had important consequences on estimates of g from these two approaches.

More recent simulations and laboratory experiments have not realized the wide range of

scales and long durations found in environmental flows, but the Reynolds numbers achievable in DNS and experiments have increased substantially in the last decade. Furthermore, the control over the large scales made possible by experimental devices and the capabilities of modern measurement techniques have greatly improved the determination of mean dissipation rate for tests of Equation 1.1. The earliest DNS involving Lagrangian statistics due to Riley & Patterson (1974) [43] were restricted to Taylor-scale Reynolds number [1] $R_\lambda \leqslant 35$ on grids of 32^3 points. By 1989 Yeung & Pope [53] reported Lagrangian statistics on grids of up to 128^3 points at $R_\lambda \approx 93$, with results for relative dispersion at this Reynolds number reported by Yeung [44] in 1994. Since then computer power has increased drastically [54], with Yeung & Borgas (2004) [49] studying dispersion on grids of 512^3 points at $R_\lambda \approx 240$. Ott & Mann [35] were able to infer $g \approx 0.5 \pm 0.2$ from the statistical analysis of the relative motion of Polystyrene particles in a grid-stirred tank of water at $R_\lambda \approx 140$. Comparable estimates of Richardson's constant falling in the range $0.5 \leq g \leq 1.0$ obtained from particle tracking in DNS have accumulated rapidly thereafter [49, 55, 56] at Taylor-scale Reynolds numbers up to 650 [50]. At the same time, methods of isolating particle dynamics at fixed length scales have been applied to the problem of relative dispersion and, coupled with some long-standing but inadequately-tested models of the dispersion process, have been used to estimate Richardson's constant from alternative statistical analyses of the trajectories of particle pairs.

The principal method of analyzing dispersion at fixed length scales (instead of fixed instants in time) is the computation of exit times. The exit time at a fixed separation distance r_n is the time taken for the two particles in a given pair to first reach a distance r_n from each other measured from the first time they were separated by some fraction of r_n. A diagram of an example exit event is shown in Figure 1.1. Since turbulence has a tendency to increase particle pair separation, the factor between the two thresholds (denoted by ρ) controls the range of scales acting to change the pair's separation distance except in the

[1] Turbulence is often parameterized by the Taylor-scale Reynolds number $R_\lambda = \sigma_u \lambda / \nu$ for flows of fluids with kinematic viscosity ν. Here, σ_u is the root-mean-square velocity component. The Taylor scale is defined to be $\lambda = \left[\sigma_u^2 / \langle (\partial u_1 / \partial x_1)^2 \rangle\right]^{1/2}$ (where $\langle (\partial u_1 / \partial x_1)^2 \rangle$ is the mean-squared longitudinal gradient of one velocity component).

rare case of particles moving back closer together for a long period of time. Exit time may be used as a random variable, and its moments scale with the threshold distance r_n according to Kolmogorov's similarity hypotheses [57]. The inertial subrange in moments of exit time only includes those pairs with separation distances in the inertial subrange. This improves the possibility that such pairs will be driven through successive thresholds in r_n by inertial-range eddies alone, making the strict conditions for inertial-range scaling [16] identified in the previous subsection easier to satisfy in practice.

Artale *et al.* [58] computed exit times from measurements of dispersion in the Mediterranean Sea. The technique has also been used by Boffetta & Sokolov [59] in simulations of two-dimensional turbulence and by Biferale *et al.* [56] in DNS of turbulence in three dimensions. Experimental measurements of exit times in dispersion at $R_\lambda \approx 815$ were reported by Ouellette *et al.* [38]. Boffetta & Sokolov [59] found the exit time PDF corresponding to the pair separation PDF predicted by Richardson's [12] diffusion model of relative dispersion. By applying Kolmogorov's similarity hypotheses to the scale-dependent diffusivity in Richardson's model they were able to write an expression for g in terms of mean exit time in two-dimensional turbulence. Biferale *et al.* [56] derived a similar expression for three-dimensional turbulence and estimated $g \approx 0.5 \pm 0.05$ from mean exit time in a DNS at $R_\lambda \approx 280$. Exit times may also be used to test for intermittency-free inertial-range scaling directly, without the use of diffusion models, through the relation [57, 60]

$$\langle T^{-3}(r_n)\rangle = C_{R,-3}\langle\varepsilon\rangle r_n^{-2} \ , \tag{1.2}$$

in which T is the exit time and $C_{R,-3}$ is a universal constant analogous, but not directly connected, to Richardson's constant g. Since complete statistical analysis of exit times requires every particle pair (even slowly-separating ones) to cross the largest thresholds r_n of interest, the particles must unambiguously enter the regime when $t \gg T_L$, which has not happened in prior simulations and experiments.

The fact that the work reviewed above has only established the order of magnitude of g makes it clear that the search for universality in turbulent relative dispersion is greatly

complicated by simultaneous dynamics from different scales dominated by different dynamical processes. Given the greater difficulty in approaching the conditions (such as isotropy, wide scale separation in space and time, etc.) required to test Kolmogorov's 1941 similarity hypotheses for particle pair statistics compared to Eulerian statistics, it may seem premature to examine the joint statistics of three or more particles. It seems reasonable to anticipate greater difficulty in ensuring that a multiparticle cluster's additional degrees of freedom satisfy the preconditions for inertial subrange scaling than exists for particle pairs. Clusters of three or more particles have distinct shapes, but the amount of theoretical work predicting how moments and PDFs of the shapes of clusters should scale in the inertial subrange is minuscule compared to the reviewed body of work predicting inertial-range scaling of their average spatial extents, and there is no consensus on what to expect or what is worth testing. However, there are already simulations and measurements of quantifiable shape parameters that show statistical self-similarity (more specifically, statistical invariance with respect to time) in time intervals beginning after τ_η but before T_L (when the inertial subrange is postulated to exist in Kolmogorov's 1941 theory) more clearly than mean-square pair separation shows unambiguous t^3 scaling.

By calculating the averages of the principal-axis displacements of tetrads in a DNS at $R_\lambda \approx 82$, Pumir *et al.* [45] found a tendency for turbulence to strongly flatten and elongate tetrads at dissipation-range scales and, for $t \gg T_L$, demonstrated the relaxation of tetrads towards a mean shape identical to that of a hypothetical ensemble of tetrads made up of particles with normally-distributed position vector components. This work also contained results for the time evolution of mean tetrahedron volume. The experiment of Castiglione & Pumir [61] consisted of measurements of three-particle clusters in two-dimensional turbulence and produced distributions of various shape parameters for triangles. It was found that parameterizations of triangle shapes (to be presented in later sections) are biased towards nearly collinear configurations at intermediate scales of both space and time, and their PDFs do not change during this interval.

The DNS of three-dimensional isotropic turbulence at $R_\lambda \approx 280$ by Biferale *et al.* [62]

also had an interval of invariance for PDFs for tetrad principal-axis displacements. By applying the previously-reviewed fixed-scale techniques to these quantities, Biferale *et al.* [62] predicted an average shape for tetrads in inertial subrange turbulence. The experimental measurements of Lüthi *et al.* [39] at $R_\lambda \approx 140$ suggested that mean shapes of triangles and tetrads in three-dimensional turbulence were constant during an intermediate interval of time and different from the mean shape of the Gaussian ensemble given by Pumir *et al.* [45]. In the experiments of Xu *et al.* [63] at $R_\lambda \approx 690$ and 815, distributions of the shape of tetrads developed a strong bias towards highly elongated shapes and remained unchanged for over 30 Kolmogorov-scaled time units t/τ_η. Very few other studies [64] of the statistical geometry of multiparticle dispersion have been reported, and interpreting the few published results is made more difficult by the disparities between the Reynolds numbers and durations of the simulations and experiments completed thus far.

1.4 Thesis objectives and outline

In reviewing the challenges in understanding and testing the most fundamental theory in turbulent relative dispersion, we have also identified current approaches to dealing with these challenges. We set out to achieve the following goals:

1. Simulations of turbulence at the highest Reynolds number presently feasible ($R_\lambda \approx 1000$) for multiple Lagrangian integral times, including tetrads with a wide range of initial sizes. To achieve this goal, the parallel implementation of the cubic spline interpolation scheme used for obtaining particle velocities must be improved to allow large numbers of particles to be tracked in these simulations.

2. Statistical analysis of the shapes and sizes of triangles and tetrads in these and prior simulations across a range of Reynolds numbers. Particular attention must be paid to finding the most effective way of correcting for finite initial tetrad sizes to clearly establish trends towards statistical universality in multiple regimes of turbulent relative dispersion. The sparsity of work in the statistical geometry of relative dispersion presents an opportunity to propose and study additional parameters to describe the shape of a tetrad.

3. Improved understanding of cross-scale contamination in relative dispersion and the use of fixed-scale statistics such as exit times to mitigate it. The value of $C_{R,-3}$ in Equation 1.2 has not been determined experiments or a significant number of simulations yet, and long simulations will contribute to our understanding of it.

4. Comparison of linear interpolation to splines interpolation of the velocity field onto particle positions. Although the impact of interpolation errors on particle tracking has been quantified before [65], the impact of these errors on relative dispersion statistics is not well-understood.

Progress towards these goals is presented in this thesis as follows:

In Chapter 2 we review the numerical method and parallel algorithm used to solve for the Eulerian velocity field in the simulations reported in this work. The particle tracking algorithm and spline interpolation scheme due to Yeung & Pope [65] are reviewed as well. We then present current efforts to improve the parallel implementation of the spline interpolation algorithm, with detailed study of the performance of various communication schemes on massively parallel supercomputers at high processor counts. Current challenges in this effort are also reviewed.

We describe the initialization scheme for our tetrads, the simulation database and recent additions to it in Chapter 3. Established techniques for assessing Richardson-Obukhov scaling in functions of pair separation are applied to the spatial extents of particle pairs, triangles and tetrads in simulations across a range of Reynolds numbers. A recent approach to estimating Richardson's constant from the time derivative of functions of $\langle r^2 \rangle$ [50] is reviewed and extended to multiparticle quantities.

Chapter 4 covers our work in the statistical geometry of turbulent relative dispersion. We present the mathematical framework of the "moment-of-inertia-like" matrix G and provide qualitative interpretations of various functions of G. We study the time evolution and scaling of PDFs and moments of tetrad volume, triangle area, and shape parameters of both tetrads and triangles for the full range of initial conditions and simulations. We make estimates and inferences of inertial subrange behavior in these statistics as well.

The fixed-scale analysis of relative dispersion through exit times is the subject of Chapter 5. A brief review of diffusion models in relative dispersion is presented and estimates of g from these models are compared to estimates of g in Chapter 3 that are obtained from $\langle r^2 \rangle$. Current issues in testing Equation 1.2 and additional requirements for inertial range scaling in exit times are identified. This chapter concludes with comparisons of dispersion statistics from DNS with linear interpolation to DNS with spline interpolation.

We conclude the thesis and briefly discuss future directions of this research in Chapter 6.

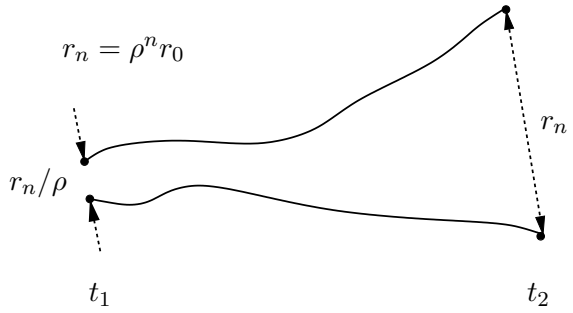

Figure 1.1: Example exit event for the separation distance $r(t)$ of a particle pair. The exit time $T = t_2 - t_1$ is the elapsed time between the first time the $r(t)$ reaches r_n/ρ ($t = t_1$) and the first time $r(t)$ reaches r_n ($t = t_2$). The thresholds are geometrically incremented from r_0 by the factor $\rho > 1$.

CHAPTER II

DIRECT NUMERICAL SIMULATIONS AND PARALLEL PARTICLE TRACKING

Here we describe the computational technique used in our direct numerical simulations (DNS) of homogeneous isotropic turbulence on massively parallel supercomputers and the method of extracting Lagrangian statistics from fluid particles tracked in the course of these simulations. We begin with a brief presentation of the numerical scheme and parallelization of the solution of the Navier-Stokes equations from the Eulerian point of view on a Cartesian grid. We continue with a description of particle tracking in these simulations and motivate the need for accurate and efficient interpolation of the Eulerian velocity field (available at fixed grid points) at the position of a moving fluid particle. We review cubic spline interpolation and previous parallel implementations in our DNS code. A parallel "pipeline" algorithm for cubic spline interpolation is presented in detail and followed by a survey of strategies for its implementation in the Message Passing Interface (MPI) protocol utilized by our code. The chapter ends with a performance analysis of these approaches to parallel spline interpolation on the two largest Cray XT5 systems in the world as well as a summary of the issues encountered in this work.

2.1 Numerical scheme for the Eulerian velocity field

2.1.1 Pseudospectral solution of the Navier-Stokes equations

Direct numerical simulation consists of the numerical solution of the exact equations of motion for the fluid flow of interest at all relevant space and time scales encountered in the problem of interest. A particularly successful method for studying homogeneous turbulent flows is the pseudospectral approach introduced by Orszag & Patterson [66] and developed further by Rogallo [67]. The simulation procedure presented here involves a parallel version of Rogallo's algorithm applied towards isotropic turbulence.

The momentum equation for an incompressible fluid with constant density ρ and constant kinematic viscosity ν at time t in the absence of body forces is

$$\frac{\partial U_i}{\partial t} = -U_j \frac{\partial U_i}{\partial x_j} - \frac{1}{\rho}\frac{\partial P}{\partial x_i} + \nu \frac{\partial^2 U_i}{\partial x_j \partial x_j} \ , \tag{2.1}$$

where U_i and P denote instantaneous velocity and mechanical pressure, respectively. Repeated Roman subscripts represent are subject to the Einstein summation convention in Cartesian tensor notation. Mass conservation under these conditions is written as

$$\frac{\partial U_i}{\partial x_i} = 0 \ . \tag{2.2}$$

The instantaneous velocity U_i and pressure P can each be written as the sum of an average value and a fluctuation such that $U_i = \langle U_i \rangle + u_i$ and $P = \langle P \rangle + p_i$. In the case of homogeneous isotropic turbulence, which has no mean velocity or pressure gradients, Equations 2.1 and 2.2 apply directly to the fluctuating velocity field.

In the pseudospectral approach, we integrate an ordinary differential equation at each of the N^3 wave vectors $\mathbf{k} = (k_1, k_2, k_3)$ (whose components are integers) making up a discrete Fourier series representation of the fluctuating velocity field. There are N Fourier modes at integer-valued wave numbers in each coordinate direction of a periodic domain with sides of length 2π. The velocity field $u_i(\mathbf{x})$ at a point in space $\mathbf{x}$ is approximated with N^3 Fourier modes $\hat{u}_i(\mathbf{k}, t)$ such that

$$u_i(\mathbf{x}) = \sum_{k_1=-N/2+1}^{N/2} \sum_{k_2=-N/2+1}^{N/2} \sum_{k_3=-N/2+1}^{N/2} \hat{u}_i(\mathbf{k}) \exp(\imath \mathbf{k} \cdot \mathbf{x}) \ , \tag{2.3}$$

where $\imath = \sqrt{-1}$. Only $N/2 - 1$ modes in one of the three directions in Equation 2.3 need to be explicitly considered since the conjugate symmetry of the Fourier representation of real-valued quantities means that the complex conjugate of a Fourier mode of the velocity field, $\hat{u}_i^*(\mathbf{k})$, determines $\hat{u}_i(-\mathbf{k})$. The governing equations for the Fourier modes $\hat{u}_i(\mathbf{k}, t)$ at the wave vector $\mathbf{k}$ are obtained by taking the discrete Fourier transform of Equations 2.1 and 2.2. The result is

$$\frac{\partial \hat{u}_i(\mathbf{k}, t)}{\partial t} = \hat{a}_i(\mathbf{k}, t) \ , \tag{2.4}$$

where the acceleration terms on the right-hand side are

$$\hat{a}_i(\mathbf{k}, t) = -\imath k_j \widehat{u_j u_i}(\mathbf{k}, t) + \imath k_i \frac{\hat{p}}{\rho}(\mathbf{k}, t) - \nu |\mathbf{k}|^2 \hat{u}_i(\mathbf{k}, t) \ , \tag{2.5}$$

and $|\mathbf{k}| = \sqrt{k_i k_i}$ is the length of the wave vector $\mathbf{k}$. The Fourier representation of the incompressibility condition (Equation 2.2) becomes

$$k_i \hat{u}_i(\mathbf{k}, t) = 0 \ . \tag{2.6}$$

The left-hand-side of Equation 2.4 is marched, starting at time t, in discrete time steps Δt with an explicit second-order Runge-Kutta time marching scheme consisting of a predictor step,

$$\hat{\mathbf{u}}^\star(\mathbf{k}) = \hat{\mathbf{u}}(\mathbf{k}, t) + \Delta t \hat{\mathbf{a}}(\mathbf{k}, t) \ , \tag{2.7}$$

where $\hat{\mathbf{u}}^\star(\mathbf{k})$ is the predictor velocity vector used to form the nonlinear corrector acceleration vector $\hat{\mathbf{a}}^\star(\mathbf{k})$ (via Equation 2.5) used in the corrector step,

$$\hat{\mathbf{u}}(\mathbf{k}, t + \Delta t) = \hat{\mathbf{u}}(\mathbf{k}, t) + \frac{\Delta t}{2} \left[\hat{\mathbf{a}}(\mathbf{k}, t) + \hat{\mathbf{a}}^\star(\mathbf{k}) \right] \ . \tag{2.8}$$

Projecting $\hat{\mathbf{u}}(\mathbf{k}, t)$ into the plane perpendicular to the wave vector $\mathbf{k}$ enforces the continuity condition Equation 2.6 and accounts for the pressure gradient $k_i \hat{p}(\mathbf{k}, t)/\rho$. An integrating factor at each time step [67] treats the diffusion term $\nu |\mathbf{k}|^2 \hat{u}_i(\mathbf{k}, t)$ exactly from t to $t + \Delta t$. The allowable step duration Δt at each time step is limited by the Courant-Friedrichs-Lewy (CFL) number, a stability parameter defined as

$$\mathrm{CFL} = \Delta t \max_{\mathbf{x}} \left\{ \sum_{\alpha=1}^{3} \frac{|u_\alpha(\mathbf{x}, t)|}{\Delta x_\alpha} \right\} \ . \tag{2.9}$$

The CFL number needs to be less than unity for numerical stability [1], and is usually 0.6 in our simulations.

The nonlinear terms, $\widehat{u_j u_i}(\mathbf{k}, t)$, are related to the individual velocity components $\hat{u}_i(\mathbf{k}, t)$ through a convolution sum that requires N^6 operations to evaluate in three dimensions. This cost is prohibitively high, so a "pseudospectral" approach involving inverse fast Fourier transforms (FFT) is used to obtain the velocity field on a Cartesian grid of N^3 points in the "physical space" where Equation 2.1 and 2.2 are written. Forward FFTs convert products of the velocities at these grid points $u_i(\mathbf{x}, t) u_j(\mathbf{x}, t)$ into the nonlinear terms $\widehat{u_j u_i}(\mathbf{k}, t)$ at each unique wave vector in the Fourier representation. The FFTs of nonlinear product terms introduce aliasing errors [68] that must be corrected for or eliminated, and the methods of

truncation (due to Patterson & Orszag [69]) and grid shifts (due to Rogallo [67]) are used in our code.

2.1.2 Representation of the flow domain for parallel computing

The majority of the most powerful supercomputers currently available [54] are distributed-memory systems with hundreds of thousands of interconnected cores capable of petaflop ($O(10^{15})$ floating point operations per second) performance. The cost of the pseudospectral algorithm described in §2.1.1 scales with the number of grid points in each direction N to order $O(N^3 \log_2 N)$. Since the grid resolution (N^3) required for DNS grows with Reynolds number at least as steeply as $N^3 \sim R_\lambda^{9/2}$ [70], the high Reynolds numbers needed for the study of homogeneous turbulence are attainable only at great computational cost. We must distribute the flow domain of N^3 grid points onto M processing elements that carry out the solution procedure in parallel and exchange data when needed. In this thesis, a processing element, such as a CPU core, is uniquely identified with a "task" in the Message Passing Interface (MPI) protocol [71, 72].

We transform the velocity field from the Fourier representation to physical space (and back) using nested one-dimensional FFTs of length N (Equation 2.3). A subdomain of the grid stored by a single task must have all N points in at least one direction to provide a full period to the FFTs computed by that task. Dividing the grid into "slabs" along one coordinate direction limits us to $M \leqslant N$, with the workload of a given task scaling with $O(N^2 \log_2 N)$ at best. In this approach, a simulation on a domain with 4096^3 grid points would be unable to fully utilize the number of cores available on larger supercomputers since only 4096 processors could be applied to the problem.

Further subdivision of slabs into "pencils" allows M to be as large as N^2, which is far more suitable for large problem sizes on massively parallel supercomputers. In this subsection we briefly present the current parallel data decomposition, its implementation in MPI and the representation of the periodic domain in physical space. A full presentation of the current parallel algorithm is given by Donzis *et al.* [73], but the details of the parallel decomposition of the physical-space grid, shown in Figure 2.1, are relevant in this thesis.

The N^3 points of the flow domain in physical space are distributed among a Cartesian "processor grid" of $M_1 \times M_2 = M$ MPI tasks. A given MPI task has a coordinate location in this grid that we write as (P_1, P_2), where P_1 is the coordinate in the first direction of the processor grid and P_2 is the coordinate in the second direction. These coordinates are constrained by the number of MPI tasks in each direction such that $0 \leqslant P_1 \leqslant M_1 - 1$ and $0 \leqslant P_2 \leqslant M_2 - 1$. Tasks with the same P_1-coordinate are grouped together in columns of M_2 tasks, and tasks with the same P_2-coordinate are grouped together in rows of M_1 tasks. There are thus M_1 columns and M_2 rows of processors that contain non-overlapping subsets, called "pencils," with $N_{y,j}$ points in the x_2 direction, $N_{z,i}$ points in the x_3 direction and a full period in the x_1 direction. The pencil dimension $N_{z,i}$ is at least N/M_1, reaching this value for all tasks when N is divisible by M_1 (this does not necessarily have to be the case, and unequally-sized pencils are handled correctly by the code). Likewise, $N_{y,j}$ is at least N/M_2, reaching this value for all tasks when M_2 is a factor of N.

2.2 Particle tracking

A fluid particle with position $\mathbf{X}(\mathbf{x}_0, t)$ at time t is uniquely identified by its initial position $\mathbf{x}_0 = \mathbf{X}(\mathbf{x}_0, 0)$[9, 6]. The velocity of a given particle $\mathbf{V}(\mathbf{x}_0, t)$ is determined by the Eulerian velocity $\mathbf{u}(\mathbf{x}, t)$ at the particle location in the surrounding fluid. The particle trajectory thus evolves according to the following equations:

$$\begin{aligned} \frac{d\mathbf{X}(\mathbf{x}_0, t)}{dt} &= \mathbf{V}(\mathbf{x}_0, t) \\ \mathbf{V}(\mathbf{x}_0, t) &= \mathbf{u}(\mathbf{X}(\mathbf{x}_0, t), t) \ . \end{aligned} \tag{2.10}$$

The Eulerian velocity field $\mathbf{u}$ is available at N^3 discrete grid points, and the particle velocity $\mathbf{V} = \mathbf{u}(\mathbf{X}, t)$ can be obtained by interpolation at the particle positions. Here we present the existing method for tracking fluid particles in DNS. We first review the time discretization scheme for Equation 2.10 (which is identical to the scheme used for the Eulerian field in Equation 2.4). We then describe the cubic spline interpolation procedure for computing $\mathbf{V}(\mathbf{x}_0, t) = \mathbf{u}(\mathbf{X}(\mathbf{x}_0, t), t)$. In the remainder of this chapter, a labeling dependence of a particle on its initial position $\mathbf{x}_0$ is implied, but omitted for brevity.

2.2.1 Numerical method and interpolation

We discretize Equation 2.10 with the same scheme used for the Eulerian field in Equation 2.4. It has a predictor step

$$\mathbf{X}^\star = \mathbf{X}(t) + \Delta t \mathbf{V}(t) \ . \tag{2.11}$$

where the predictor position $\mathbf{X}^\star$ is an estimate of $\mathbf{X}(t + \Delta t)$. This value is refined in the corrector step,

$$\mathbf{X}(t + \Delta t) = \mathbf{X}(t) + \frac{\Delta t}{2} \left(\mathbf{V}(t) + \mathbf{V}^\star \right) \ . \tag{2.12}$$

where the particle corrector velocity $\mathbf{V}^\star = \mathbf{u}(\mathbf{X}^\star, t + \Delta t)$ is obtained from the Eulerian velocity at the end of the corrector step in Equation 2.12 interpolated at the particle predictor position $\mathbf{X}^\star$. Cubic spline interpolation is used to obtain both $\mathbf{V}(t)$ and $\mathbf{V}^\star$. Cubic splines have fourth-order accuracy in space and are twice differentiable, making them suitability for velocity gradients and other Lagrangian statistics beyond the scope of this thesis.

The cubic spline interpolation procedure used in this thesis was introduced by Yeung & Pope [65] and is an algebraic rearrangement of standard techniques [74]. A Lagrangian quantity F (such as one of the three components of the velocity $\mathbf{V}$) is interpolated from the Eulerian field f (such as a velocity component u_i) at a particle location $\mathbf{X}$ according to the following formula:

$$F = \sum_{\gamma=1}^{4} \sum_{\beta=1}^{4} \sum_{\alpha=1}^{4} b_\alpha(\xi_1) c_\beta(\xi_2) d_\gamma(\xi_3) e^{(f)}_{I+\alpha, J+\beta, K+\gamma} \ . \tag{2.13}$$

In Eq. 2.13, Greek subscripts indicate dependence on grid points, not tensor indices. Four grid points in each coordinate direction (including a reference point (I, J, K)) are required to compute the value of the interpolating spline at the particle position. At each of these 4^3 points a spline coefficient $e^{(f)}_{I+\alpha, J+\beta, K+\gamma}$ is multiplied by the three one-dimensional cubic basis functions (b_α, c_β and d_γ) of the particle position, which is expressed as a fraction ξ_i of a grid spacing. Detailed expressions for the spline coefficients $e^{(f)}_{I+\alpha, J+\beta, K+\gamma}$ and the one-dimensional cubic basis functions (b_α, c_β and d_γ) may be found in Yeung & Pope [65]. We focus now on the parallel implementation of the interpolation procedure outlined above.

2.2.2 Parallel implementation: global storage and summation

The spline coefficients $e^{(f)}_{I,J,K}$ are computed from the Eulerian field variable f at the N^3 grid points and are stored in the arrangement shown in Figure 2.2. Fluid particle positions are randomly distributed in space as the particles move throughout the turbulent velocity field. A particularly convenient way to determine the spline coefficients needed by a particular particle is to convert the particle position $\mathbf{X}$ into grid spacings, divide each coordinate by the number of grid points N, and store the remainder. The i^{th} component of the particle position with respect to the spline coefficients in the flow domain is called Y_i and is determined by the following formula:

$$Y_i = \frac{X_i}{(2\pi)/N} \mod N \ . \tag{2.14}$$

The components of the basis function argument ξ_i can be expressed in terms of Y_i as $\xi_1 = Y_1 - I$, $\xi_2 = Y_2 - J$ and $\xi_3 = Y_3 - K$.

As mentioned in §2.2.1, each task holds one pencil of spline coefficients $e^{(f)}_{I,J,K}$ (Figure 2.2). But since splines require four points in each direction (Equation 2.13), it is often the case that a particle located near the edge of a pencil needs spline coefficients from more than one task. Therefore, it is necessary to determine which tasks have spline coefficients needed to evaluate Equation 2.13 for a given particle once $\mathbf{Y}$ has been determined. The simplest way to do this is to store the properties $\mathbf{X}$ and $\mathbf{V}$ of every one of the N_P particles tracked in a simulation on each task. All tasks then compute $\mathbf{Y}$ for all N_P particles, truncating down to the nearest integral whole number I such that $I < Y_1$. Similar steps are taken for J and K to obtain the index of the reference point for $\mathbf{Y}$ of a given particle. The m^{th} task then computes its partial contribution, F_m, to Equation 2.13 for each particle i from 1 to N_P provided $e^{(f)}_{I+\alpha,J+\beta,K+\gamma}$ lies in its pencil of spline coefficients. Each task skips those points that do not lie in its pencil in Figure 2.2. The only communication required is to sum F_m from all the tasks such that, taking V_1 of the i^{th} particle as an example,

$$V_1^{(i)} = \sum_{m=1}^{M} F_m^{(i)} \ , \tag{2.15}$$

where $F_m^{(i)}$ has been computed with Equation 2.13 on task m for those elements of $e^{(V_1)}_{I+\alpha,J+\beta,K+\gamma}$

that lie in the m^{th} task's pencil of spline coefficients. Formulas similar to Equation 2.15 may be written for other quantities such as V_2 and V_3 as well. Communication among the M tasks is needed only when evaluating Equation 2.15 with contributions from all the tasks and ensuring the result $V_1^{(i)}$ is distributed among all M tasks. A schematic of this procedure is shown in Figure 2.3.

The only communication needed in this method is illustrated in Figure 2.3 since it does not distribute any of the storage of particle properties among the tasks. Such duplication of storage is prohibitively expensive for the large numbers of particles needed to adequately sample Lagrangian statistics at high Reynolds number. Every task must store $\mathbf{X}$, $\mathbf{Y}$ and $\mathbf{V}$ for every particle in the ensemble, test each particle's use of spline coefficients in the task's pencil and evaluate Equation 2.13 if needed, and evaluate Equations 2.11 and 2.12 for each particle to integrate its trajectory in time. Thus, the only effect increasing the number of tasks has on the interpolation procedure is to increase the number of times Equation 2.13 may be skipped by a given task. For all other computations, the workload per task remains unchanged at high processor counts.

2.2.3 Parallel implementation: gather-scatter methods

Better distribution of particle data reduces the memory costs identified in the previous section. One method involves storing $\mathbf{X}$ and $\mathbf{V}$ only for batches of N_P/M particles, but using temporary storage for $\mathbf{Y}$ and F_m for all N_P particles. Each task computes $\mathbf{Y}$ for its batch of N_P/M particles. It then sends its batch of $\mathbf{Y}$ to all other tasks and gathers batches of $\mathbf{Y}$ for the rest of the particles from all the other tasks into a larger temporary buffer. Batches in this buffer are offset by a number of elements corresponding to their identification number, or rank, in the computation. This part of the procedure is shown schematically in Figure 2.4(a). The actual interpolation procedure is unchanged from the global method in §2.2.2, but, after evaluating Equation 2.15, one task scatters interpolated quantities (such as V_1) in batches back onto the tasks storing the rest of the properties for a particular batch. This step is shown schematically in Figure 2.4(b). The ratio of the the memory used by the gather-scatter method to the memory used by the original global

method of §2.2.2 is $1/2(1 + 1/M)$ for the storage of $\mathbf{X}$ and $\mathbf{Y}$. The actual interpolation steps in Equation 2.13 are not parallelized beyond the method in §2.2.2.

2.2.4 Parallel implementation: point-to-point pipelines

The methods presented thus far have been used in simulations reported in many prior studies of relative dispersion [44, 49, 50]. They require, at the very least, that each task store $\mathbf{Y}$ and individual interpolated quantities for all particles and summed spline contributions from all tasks using Equation 2.15. It is obvious that distributing all the Lagrangian quantities, including $\mathbf{Y}$, among the M tasks would further save memory. A major goal in this thesis is the introduction of a method of parallelizing the spline interpolation algorithm that distributes all Lagrangian quantities among the M tasks without needing any task to store all data for all particles at any time. We describe our arrangement of the MPI tasks and Lagrangian data into a point-to-point pipeline (where the term "point-to-point" [71] describes communication between individual MPI tasks and is distinguished from "collective" communication among all tasks in a given group) in this section.

Tasks can be grouped together in multiple ways in MPI, and the processor grid in Figure 2.2 can simultaneously be referred to as a sequential, periodic "ring" over all M tasks. A pipeline [72] is a logical way for each of the tasks in a ring to successively receive a batch of particle data from its "left" neighbor, modify it, and send it to its "right" neighbor. Particle positions $\mathbf{Y}$ and interpolated values F_m are received from the left, F_m is modified by local spline coefficients $e^{(F_m)}_{I,J,K}$ as needed by Eq. 2.13, and both are sent to the right. This procedure is repeated M times until a given batch of data returns to the task that sent it, having been to every other task in the ring. These methods are further distinguished by the fact that tasks communicate with each other one at a time. This is known as "point-to-point" communication in MPI parlance, which contrasts with "collective" communication involving all tasks in a given group at once. A pipeline for spline interpolation is shown schematically in Figure 2.5, and we now present a study of the different implementations of it in MPI that have been tested in the course of this work.

2.3 Parallel pipeline implementations of particle tracking

There are many different ways of carrying out point-to-point communication in MPI that give us control over how messages for F_m and $\mathbf{Y}$ are stored and when they are sent and received by a given task. It is interesting to determine what effects different algorithmic details and MPI subroutines have on performance and memory requirements at large particle and processor counts. The methods presented below have been tested on Cray XT5 systems at the National Center for Computational Sciences (NCCS, the site of Jaguar) and the National Institute for Computational Sciences (NICS, the site of Kraken) at Oak Ridge National Laboratory. These tests have guided the adoption of a particular pipeline implementation for use in three of the simulations in this work, and have identified the need for future work in improving pipeline performance for particle tracking.

2.3.1 Fully blocking

The simplest pipeline implementation is one in which all communication is done at the end of a pipeline stage. The routine `MPI_SENDRECV` efficiently and safely combines send and receive operations needed at the end of a pipeline stage into a single subroutine call. A schematic of this method is shown in Figure 2.6. Extra storage of N_P/M numbers for F_m and each component of $\mathbf{Y}$ is needed for a buffer (labeled "next" in Figure 2.6) for receiving the next stage's particles from the left. The pipeline is pushed to the next stage when the "next" batches overwrite the local storage of $\mathbf{Y}$ and F_m. The pipeline is finished after M stages, and each task ends the interpolation procedure with the positions and interpolated F for the batch it started with.

During each stage execution does not proceed past `MPI_SENDRECV` until the task has posted that all N_P/M particles have been sent right and all N_P/M particles have been received from the left. Thus, `MPI_SENDRECV` is a "blocking" subroutine in MPI terminology. No other instructions in the spline interpolation procedure may be carried out during the time a given task spends sending particles right and receiving them from the left. More flexible control over the communication workload to reduce the time a task spends waiting on its neighbors could lead to improved performance, and we pursued this goal with several

more sophisticated approaches.

2.3.2 Non-blocking

MPI also provides "non-blocking" routines that allow execution to proceed past them and essentially conduct communications in the "background" of the calling program. If computer hardware permits, computation and communication may overlap somewhat and occur simultaneously as each task evaluates Equation 2.13 locally while data for the next stage of the pipeline are sent and received in the background. As a safety measure, we also have control over when the code waits for non-blocking communication to finish before pushing the pipeline. In particular, data being sent or received must not be modified during non-blocking communication. The particles' basis function positions $\mathbf{Y}$ are not modified by the interpolation procedure, so non-blocking transmission of $\mathbf{Y}$ is straightforward. The partial contribution to the interpolated variable F_m is modified, so non-blocking transmission of F_m is somewhat more complicated. Different combinations of blocking and non-blocking communication are possible.

Figure 2.7 shows a version of the pipeline whose stages begin with non-blocking MPI calls to begin sending $\mathbf{Y}$ to the right and receive $\mathbf{Y}$ and F_m into separate storage (labelled "next" in the figure). Execution proceeds immediately after calls to non-blocking routines, so the spline interpolation operations (Equation 2.13) on F_m of the current batch (whose storage is not written to by the previous MPI calls) overlap with the transfers initiated at the beginning of the pipeline stage. After the m^{th} task has added its spline coefficients' partial contributions to F_m, it sends F_m to the right with a blocking MPI call. Thus F_m is sent with a blocking call at the end of the stage, and $F_{m,\text{next}}$ is received with a non-blocking call. If one task is significantly faster than its neighbors in the pipeline (for example, the batch it is working on needs few of its spline coefficients), its transfer of F_m to the right could be received as rapidly as it is sent, saving communication time for its right-hand neighbor in the pipeline. For added security, each task waits for the remaining non-blocking transfers to finish (ensuring receipt of full batches for the next stage in the pipeline) before pushing the pipeline at the beginning of the next stage.

Instead of incrementally adding to F_m and sending it at the end of the stage as shown in Figure 2.7, it is possible to separately store the partial contributions to F_m in a particular stage and use separate buffers to send F_m from a previous stage using non-blocking MPI calls. This arrangement is shown in Figure 2.8 and provides the most opportunities to overlap communication and computation. Extra storage, denoted $F_{m,\text{here}}$ in Figure 2.8, is needed to avoid interfering with buffers being filled by receiving operations. The pipeline must also be advanced one more time for F_m. However, all communication would be synchronized (with corresponding time spent waiting on the slowest task to catch up) at the end of the pipeline after the spline computations possible at that particular stage are complete.

2.3.3 Persistent non-blocking

The non-blocking method described above and schematically illustrated in Figure 2.8 repeats paired sending and receiving operations for messages containing data for N_P/M particles. Since the lengths and data types of these messages are fixed at every stage of the pipeline, this scheme can be implemented with "persistent" communication in MPI. Persistent communication begins with an initialization call that binds information about message size and storage locations as well as source and destination tasks to an object, called a request, that is accessible to the calling program. Requests may be thought of as ports or channels in an analogy with networking. Communication then occurs when the persistent request is started (with calls to `MPI_STARTALL`) and stops with calls to `MPI_WAITALL`. Persistent non-blocking communication makes it possible to fix a set of parameters governing communication between two tasks once and repeatedly send messages satisfying those parameters without the repeated cost of initializing communication.

2.3.4 Row-column rings

Thus far the pipeline approach to parallel spline interpolation has been applied to a one-dimensional ring containing all M tasks. All of the techniques discussed in §2.3.1 through §2.3.3 may be applied to a pipeline over the rows in Figure 2.2 nested within a pipeline over the columns. Such an approach is shown in Figure 2.9. Dividing the pipeline up into rows

and columns could reduce the effects of latency by reducing the number of tasks that must be allowed to complete the pipeline at a given stage as well as enabling further optimizations by the MPI implementation.

2.4 Performance

The algorithms introduced in §2.3.1 through §2.3.4 have been tested on the Cray XT5 systems at the National Center for Computational Sciences (NCCS [75], which hosts Jaguar) and National Institute for Computational Sciences (NICS [76], which hosts Kraken) at Oak Ridge National Laboratory, and their performance has been compared to algorithms that rely on collective communication presented in §2.2.3. These tests have been run with isolated trials of the interpolation procedure in a test code that is separate from the full DNS code. Each trial consists of interpolating the three components of an artificially constructed velocity field for a randomly distributed ensemble of N_P test particles. We first compare the partially non-blocking method (Figure 2.7) to the gather-scatter method (Figure 2.4). Wall clock time averaged over the eight trials of each of the test cases listed in Table 2.1 is plotted against the number of cores used in a given test in Figure 2.10. The computation of spline coefficients does not depend on the number of particles and has been omitted. The time taken to carry out the eight trials does not decrease substantially with processor count, showing that communication cost is not scaling favorably with processor count. The collective algorithm is at least twice as slow as the partially non-blocking pipeline algorithm below 10,000 cores, but both take the same amount of time at 32,768 cores on Jaguar. The lower overall time taken by the pipelines scheme, along with its lower memory requirements compared to the gather-scatter scheme, has led to its adoption in production DNS, but the poor scaling of both schemes has been a serious concern.

Testing done for all of the schemes in §2.3.1 through §2.3.4 reveals that the fully blocking scheme (Figure 2.6) is faster than the non-blocking schemes that were supposed to carry out the interpolation procedure concurrently with communication. In practice this was not realized, and the improved synchronization among all tasks in the blocking procedure made it slightly faster than the partially non-blocking procedure of Figure 2.7. Tests of

this scheme on Kraken at 1024 and fewer tasks are compared to the fully blocking procedure for $N_P = 8,388,608$ in Figure 2.11. Multiple trials confirmed the superiority of the fully blocking scheme, which contradicted our expectation that non-blocking communication would provide more opportunities for tasks to always be engaged in useful communication or computation. The fully non-blocking (Figure 2.8) and persistent schemes (§2.3.3) did not perform better than the partially non-blocking scheme (Figure 2.7).

Investigating the timing for different parts of the partially non-blocking algorithm shown in Fig. 2.7 reveals where the code is slowing down. Fig. 2.12 shows the contributions of the major parts of the partially non-blocking pipeline to the total times shown in Figure 2.11. The interpolation procedure has some strong scaling, but the code is consistently spending most of its time waiting for the pipeline to synchronize before proceeding to the next stage. The supposedly non-blocking MPI calls are the first to become slower with increasing processor count. These observations, coupled with the fact that some tasks are much slower than others at a given stage of the pipeline, suggests communication and computation are not overlapping in the system itself, even though the algorithm and the MPI standard allow this to occur. This is demonstrated in Figure 2.13, which shows the slowest and fastest tasks for all stages as well as the average time per stage of the partially non-blocking pipeline. The wide range of times for waiting and non-blocking MPI calls at 1024 tasks is striking.

2.5 Conclusions and future work

We have presented and described the numerical schemes and computational approach to DNS and particle tracking used in this work. The development and implementation of a pipeline algorithm to parallelize the existing cubic spline interpolation algorithm has been central to this thesis. This and other parallel algorithms have enabled a large increase in the number of particles that may be tracked in DNS, but substantial work remains to be done in avoiding great expense and poor performance at large processor counts. The poor scaling and increasing CPU cost of the pipeline methods are not yet taking up a prohibitively large fraction of the CPU time. Nevertheless, it is still important to address performance challenges. It is clear from Fig. 2.10 that the pipeline algorithm, although not

scaling properly, is less expensive in absolute terms than the collective algorithms at all but the largest processor counts.

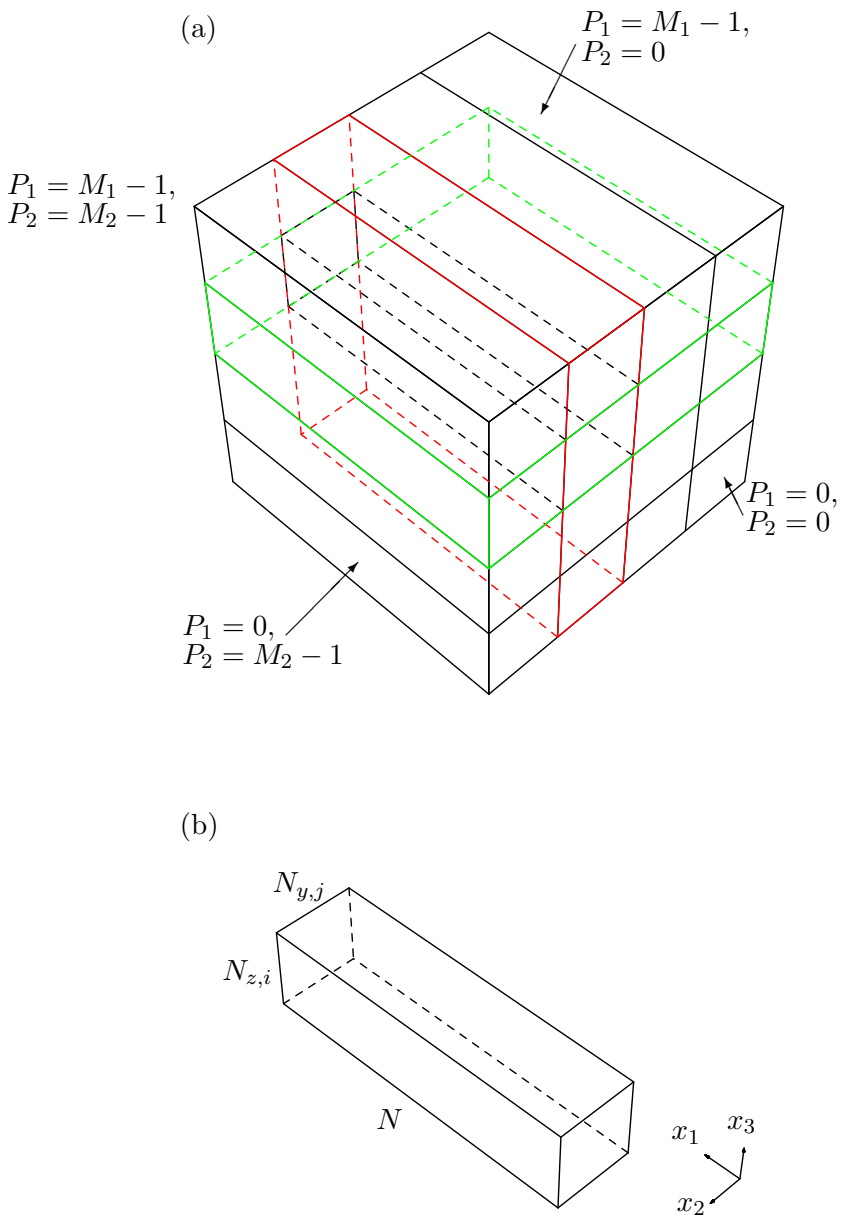

Figure 2.1: a: Parallel partitioning of a component $u_i(\mathbf{x})$ of the Eulerian velocity field in physical space. Tasks in the same row are outlined in red. Tasks in the same column are outlined in green. The location of a given task is expressed in the coordinates (P_1, P_2). Hidden dashes denote location of the example pencil shown in detail in (b). b: Example "pencil" of the velocity field. The number of grid points in each direction are labeled at the appropriate edges.

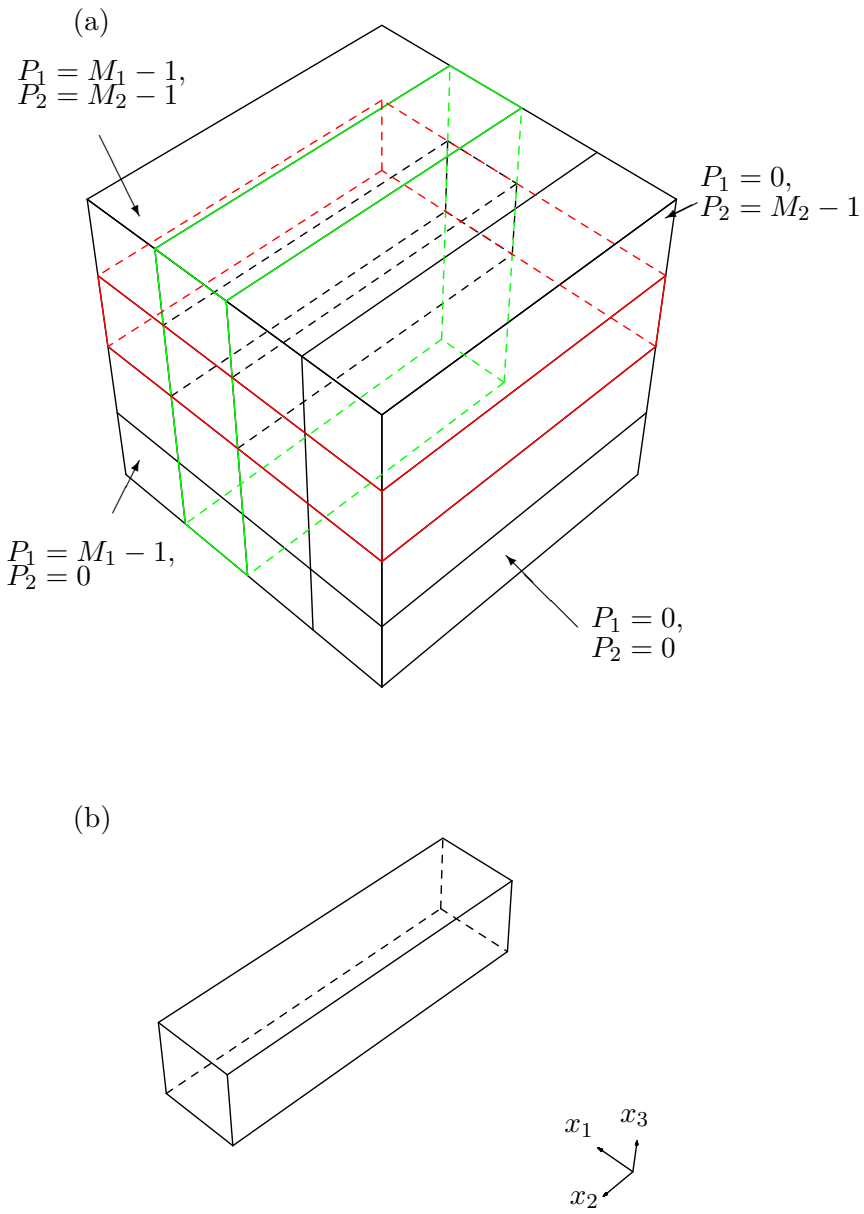

Figure 2.2: a: Parallel partitioning of spline coefficients $e^{(f)}_{I,J,K}$ for flow variable f. Tasks in the same row are outlined in red. Tasks in the same column are outlined in green. The location of a given task is expressed in the coordinates (P_1, P_2). Hidden dashes denote location of the example pencil shown in detail in (b). b: Example "pencil" of the spline coefficients.

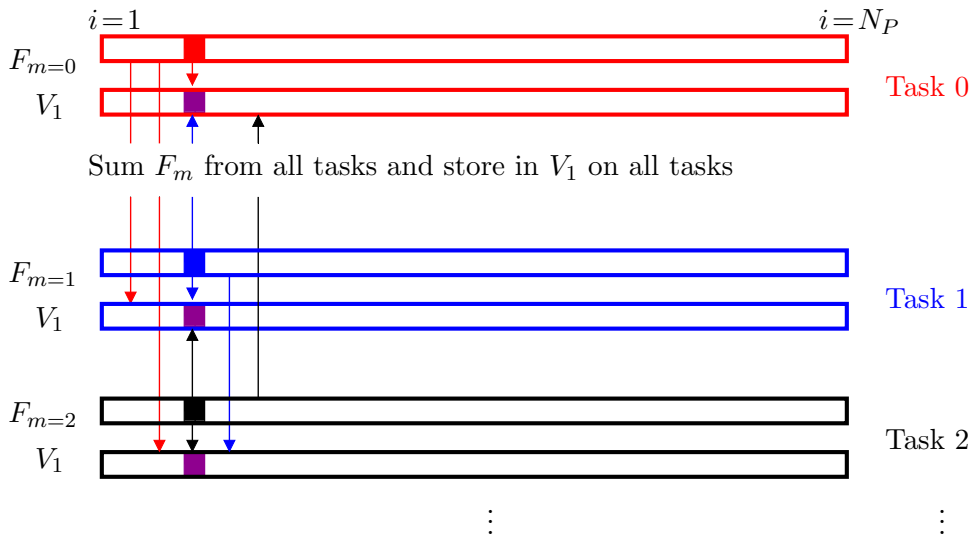

Figure 2.3: Schematic illustration of the communication procedure for the velocity component V_1 in the global storage and summation method of §2.2.2. Each task computes its spline coefficients' contribution to Equation 2.13 for each of the N_P particles and stores the result in F_m. By calling `MPI_ALLREDUCE`, each task sums F from itself and all other tasks and stores the resulting interpolated value in V_1. The schematic is from the point of view of Task 0 (red). Data for an example particle is shown in each array as a filled box. To interpolate the velocity of this particular particle, only spline coefficients from the subdomains of Task 0 and Task 1 are needed. The result is colored purple to illustrate the exclusive contributions from Tasks 0 and 1.

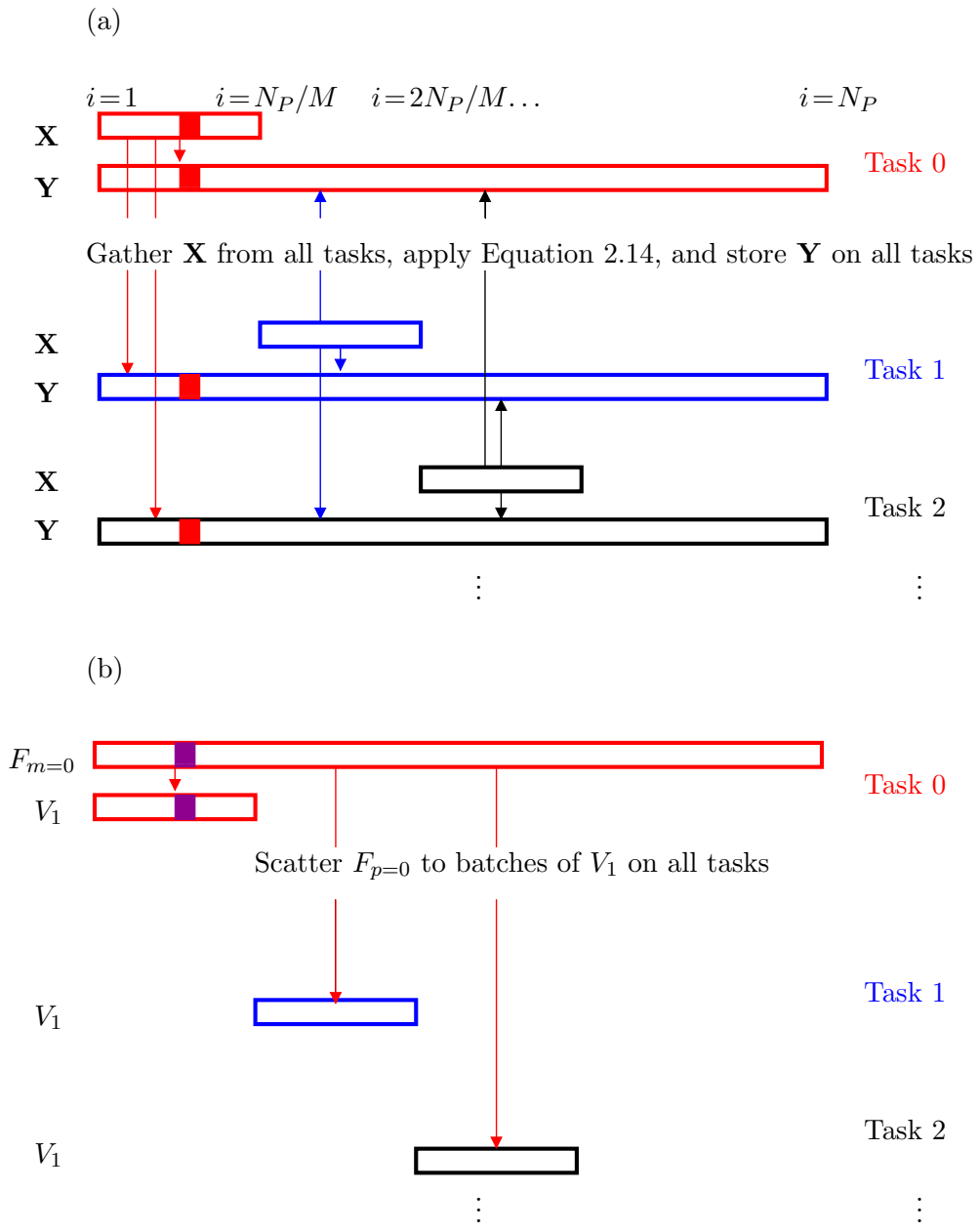

Figure 2.4: Schematic illustration of the communication steps for the gather-scatter parallel implementation of §2.2.3. a: Collecting particle positions by batch using `MPI_ALLGATHER`. All tasks store **Y** for every particle. The interpolation procedure and summation are identical to the processes described in §2.2.2 (Figure 2.3). b: Distributing interpolated V_1 back onto original batches using `MPI_SCATTER`.

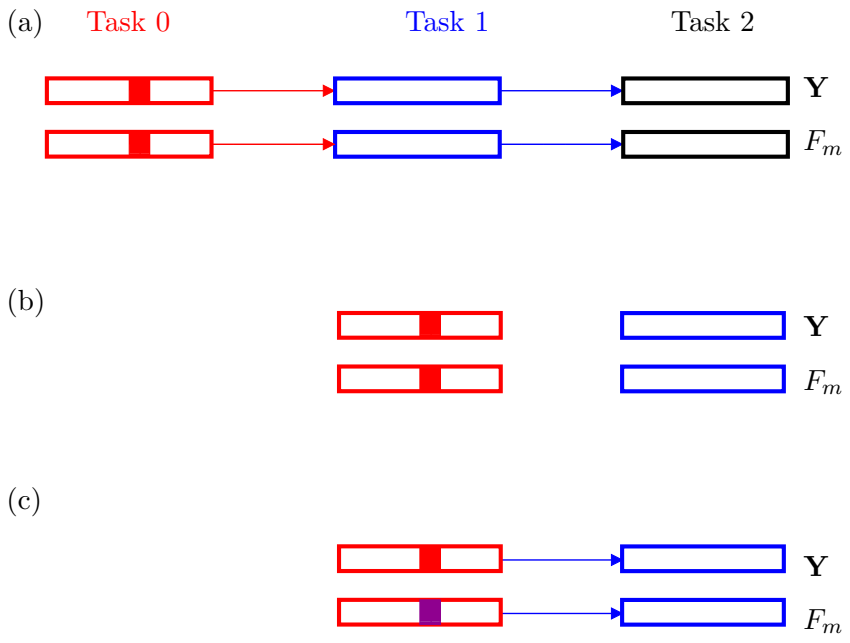

Figure 2.5: Schematic illustration of the communication steps for one stage of the pipeline parallel implementation of §2.2.4 from the point of view of Task 1. Outlined boxes are batches of N_P/M particles colored by the task storing them before and after the interpolation procedure. Quantities for an example particle associated with Task 0 (red), but using spline coefficients found on Task 1 (blue), are indicated by filled boxes. a: End of the first stage of the pipeline, after interpolation (evaluating Equation 2.13). Arrows indicate pending transfers of batches to a given task's neighbor on the right. b: Beginning of the second stage of the pipeline, after transfers in (a) are complete. Task 0 has received a batch from Task M-1 (not shown). c: End of the second stage of the pipeline, after interpolation. Task 1 has computed its contribution to the F_m of the example particle and added it to the filled box (purple). The batch is ready to be sent to Task 2.

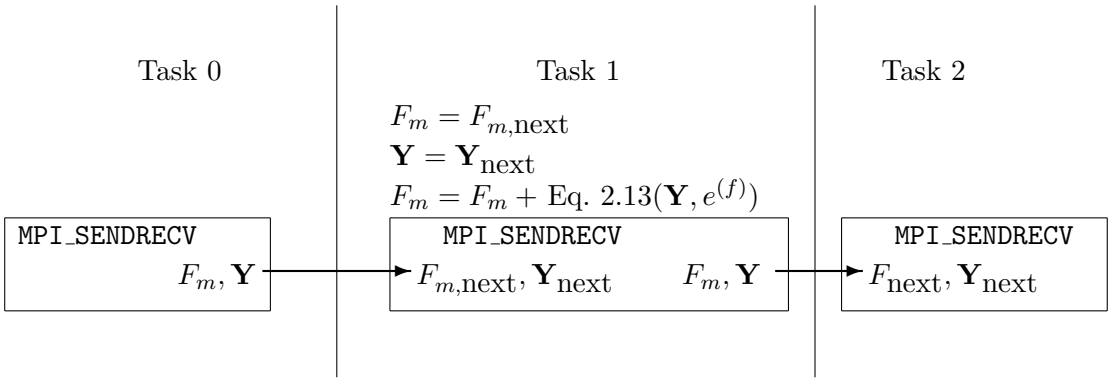

Figure 2.6: Example stage of a fully blocking pipeline (§2.3.1) for spline interpolation from the point of view of Task 1. Left and right neighbors of Task 1 do not necessarily have to have sequential task numbers, but are shown that way for convenience. Boxes are drawn around communication calls to MPI routines. Execution is blocked at the call to `MPI_SENDRECV`, which both sends a batch of particle basis function positions $\mathbf{Y}$ and interpolation contributions F_m to the right and receives a batch from the left into separate storage in the variables labelled "next."

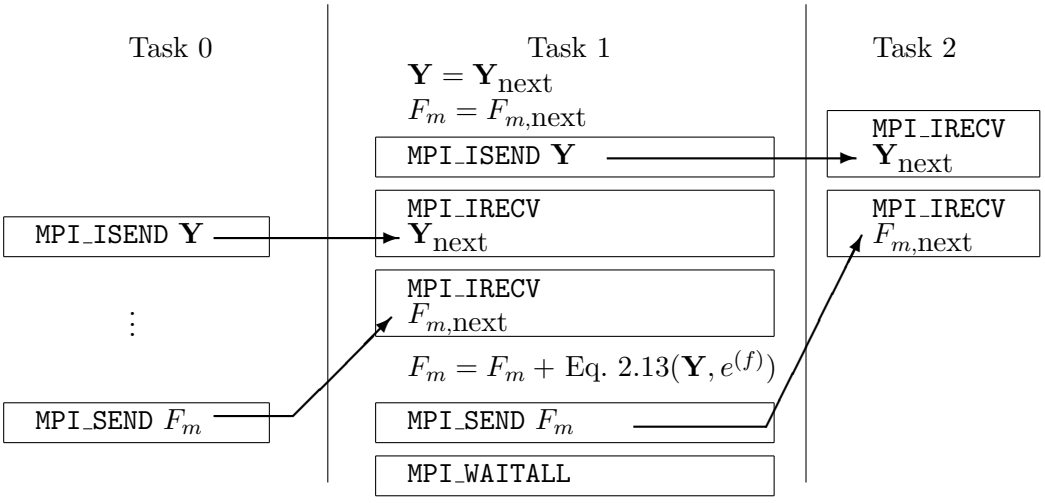

Figure 2.7: Example stage of a pipeline with non-blocking communication for the basis function positions $\mathbf{Y}$ and partially non-blocking communication for F_m, the partial contribution of the m^{th} task to the particles' interpolated values of f. After the pipeline is pushed, non-blocking MPI routines to send $\mathbf{Y}$ to the right and receive $\mathbf{Y}$ and F_m from the left (into separate storage labelled "next") are called. The spline interpolation procedure (Eq. 2.13) is carried out simultaneously with the transfers and does not involve the "next" variables being written to by `MPI_IRECV`. Updated F_m is sent right with `MPI_SEND`, a blocking routine. The stage ends by waiting for the non-blocking calls to finish (`MPI_WAITALL`).

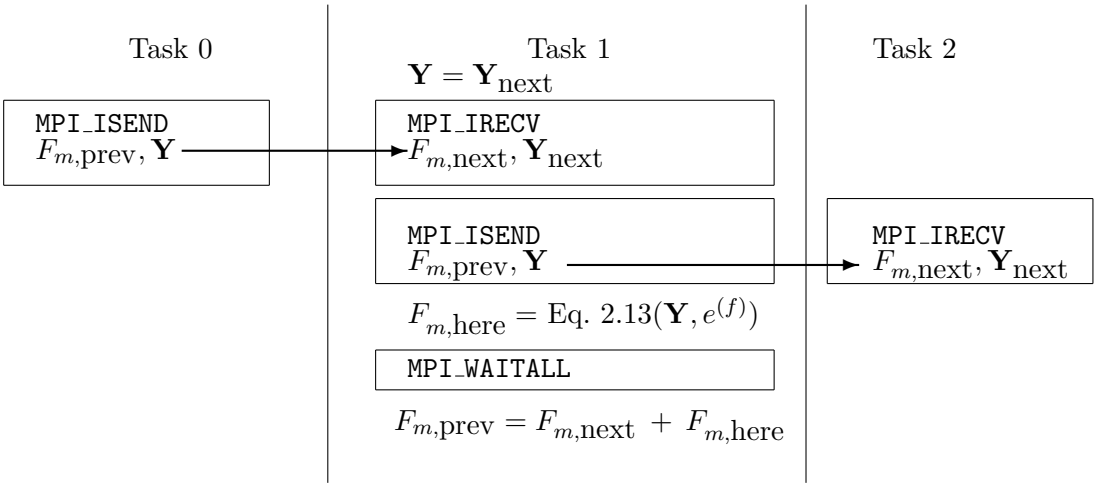

Figure 2.8: Example pipeline stage of with fully non-blocking transfers for both the basis function positions $\mathbf{Y}$ and interpolated quantity F_m. An extra buffer for $F_{m,\text{here}}$ is needed to avoid overwriting storage being used to receive the next stage's $F_{m,\text{next}}$ or send the last stage's $F_{m,\text{prev}}$ while communication occurs in the "background". For this reason, the pipeline must be "lagged" one stage, and it must be "pushed" one more time (via a `MPI_SENDRECV` call similar to the final one shown in Figure 2.6) to get F_m to correspond with the original batch of $\mathbf{Y}$ on each processor.

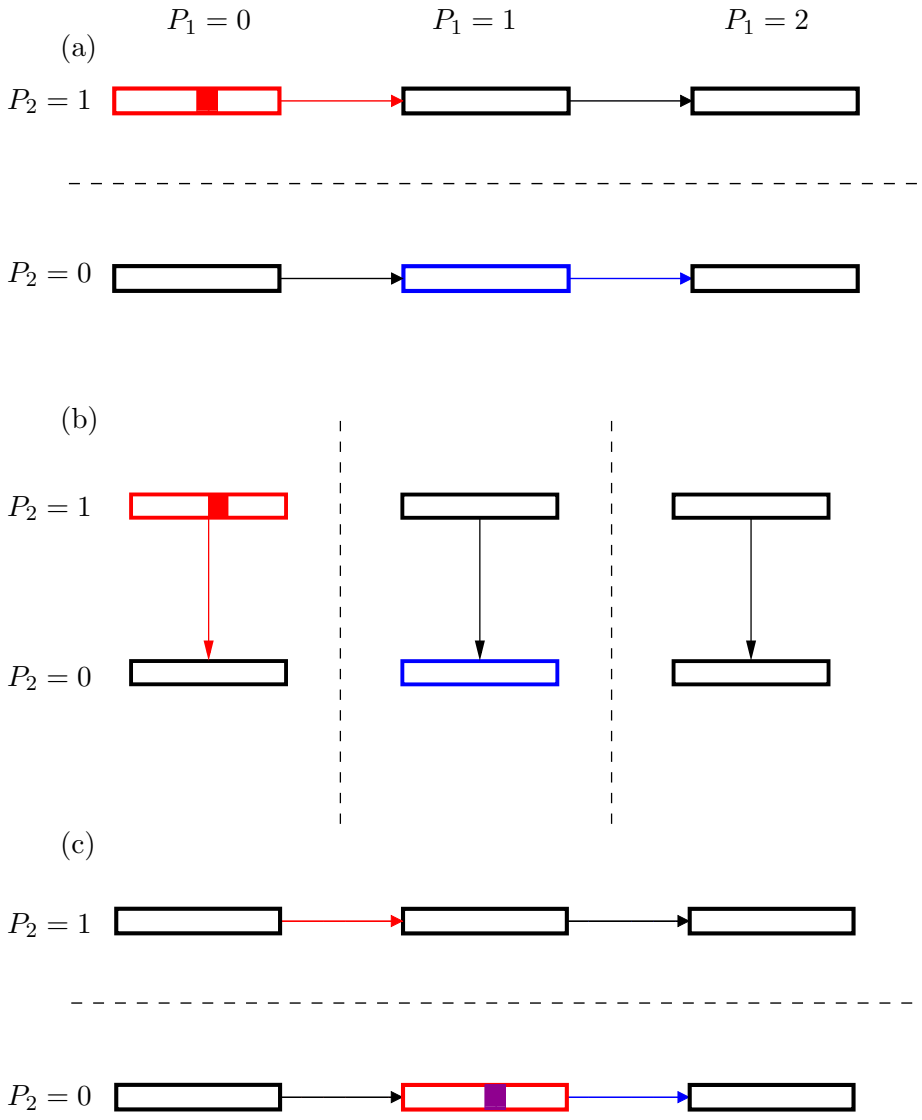

Figure 2.9: Nested parallel pipelines using the same Cartesian grid topology as the Eulerian flow domain in Figure 2.1. Boxes represent distinct batches of particles (basis function positions and the particular velocity component being interpolated) colored by the task they originate from. Arrows represent pipeline transfers colored by their sending task. a: Pipeline by rows at the end of the first stage of both pipelines. The task at (0,1) contains a particle requiring spline coefficients help by tasks (0,1) and (1,0). b: First stage of the pipeline by columns at the end of the pipeline by rows. Each task holds the batch it had at the start of the row pipeline and the interpolated quantity has been updated by all tasks in a single row. Entire rows of batches are transferred down the P_2 coordinate. c: End of the second stage of the row pipeline initiated after the first stage of the column pipeline. The example particle has been updated by the spline coefficients in task (1,0) and is colored purple to reflect this.

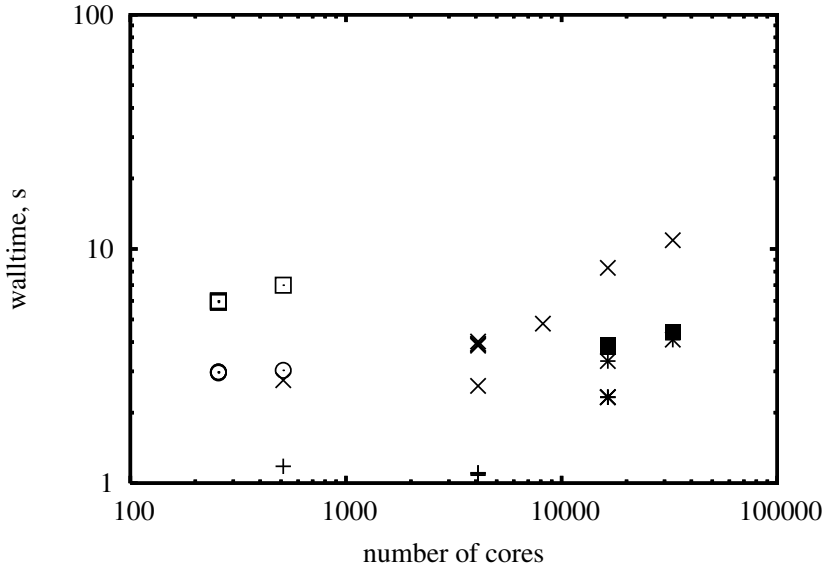

Figure 2.10: Average wall time for eight trials of the interpolation procedure. Legend is in Table 2.1.

Table 2.1: Legend for Fig. 2.10 for interpolation trials for the velocity field at the positions of N_P particles. The "collective" algorithm is described in §2.2.3 and shown in Figure 2.4. The "pipeline" algorithm (§2.3.2) is the one shown in Figure 2.7.

Symbol	N_P	Algorithm	Supercomputer
$+$	8,388,608	pipeline	Kraken
$\times$	8,388,608	collective	Kraken
$\odot$	16,777,216	pipeline	Kraken
Hollow $\square$	16,777,216	collective	Kraken
Solid $\square$	8,388,608	collective	Jaguar
$*$	8,388,608	pipeline	Jaguar

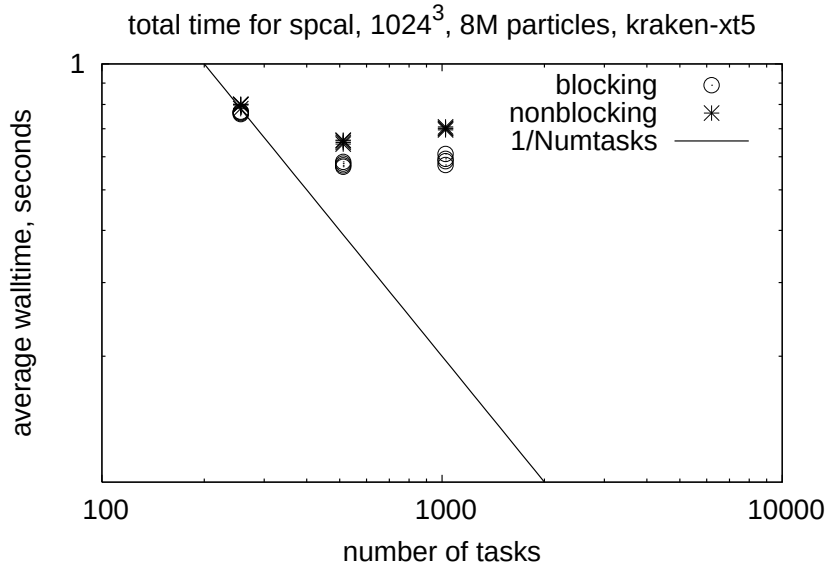

Figure 2.11: Total wall time averaged over eight trials (repeated three times) of the fully blocking method (open circles, Figure 2.6) compared to the partially non-blocking method (asterisks, Figure 2.7) with $N_P = 8,388,608$ particles on a $N^3 = 1024^3$ grid on Kraken. A solid line at $1/M$ indicates perfect strong scaling.

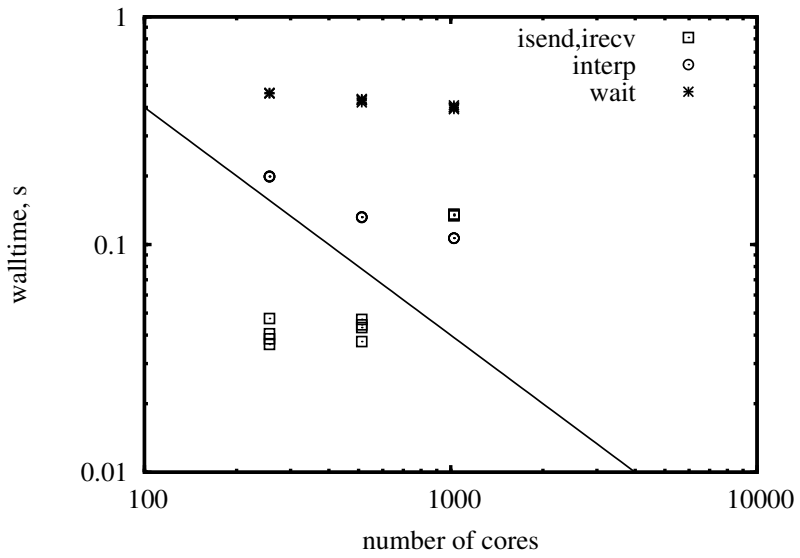

Figure 2.12: Timing contributions from each part of the partially non-blocking pipeline in Figure 2.7 to the trials shown with asterisks in Figure 2.11 on Kraken. "isend,irecv" are times for the non-blocking communication calls at the beginning of the pipeline, "interp" refers to the actual interpolation procedure (Equation 2.13) for each batch in the pipeline, and the time spent waiting at the end of a given stage for all tasks to catch up is designated "wait." The solid line represents perfect strong scaling with increasing processor count.

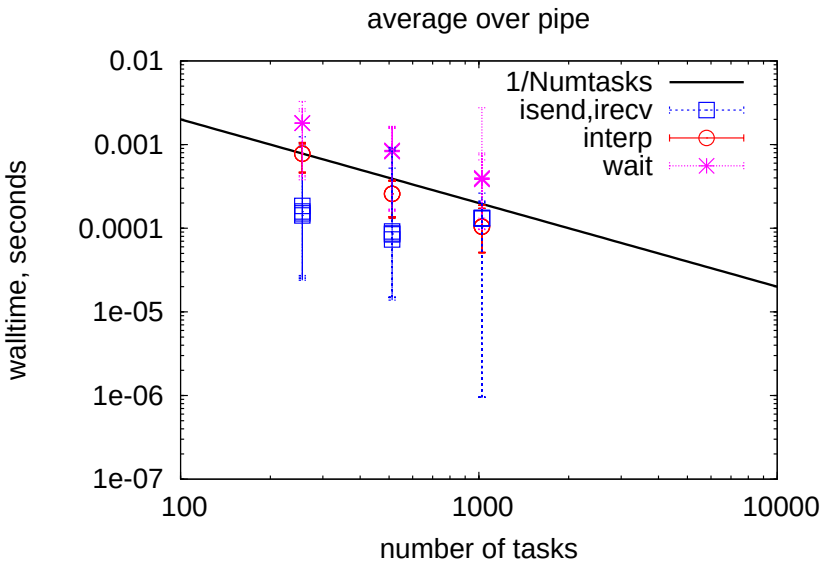

Figure 2.13: Times per stage of of the partially non-blocking pipeline (Figure 2.7). Symbols are drawn at averages for the stage, and bars are drawn between the slowest and fastest tasks in the pipeline for all stages.

CHAPTER III

SIMULATION PARAMETERS AND THE SPATIAL EXTENT OF RELATIVE DISPERSION

The fundamental challenges of studying relative dispersion discussed in §1.1, including the need for a very wide range of scales and the persistent effects of initial conditions and large-scale variability, are apparent in even the most basic statistical analysis of the motion of pairs of fluid particles. The process of testing predictions of pair separation statistics such as Richardson's t^3 law (Equation 1.1) illustrates these challenges, is interesting in its own right due to its connection to the rate at which contaminant plumes spread, and is the foundation for postulates of statistical universality in the dispersion of clusters of more than two particles. The mean-squared gyration radius of a tetrahedron is specifically included in this chapter because it is the simplest measure of the spatial extent of a tetrahedron and, like mean-squared pair separation distance, only describes the size of a contaminant cloud in turbulence.

We first show how particles are initially arranged into tetrahedra of different initial sizes in our simulations and describe how we select pairs from these tetrads. We then present our most recent simulations on 4096^3 grid points and collect simulation parameters from previous simulations into §3.1 for future reference. The deficiencies of directly testing Equation 1.1 on simulation data motivate the adoption of two methods of adjusting for initial pair separation distance r_0: differentiating mean-squared pair separation using the method of "cubed-local-slopes" [50] and studying the relative displacement vector $\mathbf{r} - \mathbf{r}_0$, which is a technique used in the early DNS of relative dispersion by Yeung [44]. The connections between the Eulerian velocity field and the statistics of dispersion in the small-time ballistic regime are covered along with the statistical features of relative dispersion in the diffusive regime at asymptotically late time. The dynamics of the ballistic regime take substantial time to diminish, while the independent motion of widely-separated particles

takes a long time to develop for those particle pairs that separate slowly, causing the ballistic and diffusive ranges to overlap for the largest initial separations in these simulations. In spite of these challenges to attaining an adequate range of scales, the DNS results at $R_\lambda \approx 1000$ are comparable to prior estimates of Richardson's constant g in the literature [35, 56].

Results for the cubed-local-slopes of the mean-squared gyration radius and the gyration radius R_D (formed using particle displacements) of clusters of four particles are also presented in this Chapter. Self-similar scaling relationships for the mean-square gyration radius in the ballistic regime, inertial subrange and diffusive regime are identified and connected to the Richardson-Obukhov law for particle pair statistics.

3.1 Simulation database

Results from multiple simulations included in our DNS database are reported in this thesis. We describe the initialization scheme for the particles and tabulate computational and physical parameters for each of the simulations studied here.

3.1.1 Initialization scheme

The initial position $\mathbf{X}_0^{(1)}$ of each particle in an ensemble of N_{tet} particles is randomly distributed throughout the solution domain. These particles serve as base vertices of tetrads of different initial sizes, which are formed by placing particles at the initial positions given by the following formula:

$$\mathbf{X}_0^{(1+i)} = \mathbf{X}_0^{(1)} + r_0 \hat{\mathbf{e}}_i, \quad i = 1, 2, 3, \tag{3.1}$$

where $\hat{\mathbf{e}}_i$ is standard basis vector in the i^{th} coordinate direction. This arrangement is shown for multiple values of r_0, each sharing the same base vertex particle and amounting to N_{sep} initial separations, in Figure 3.1. Under this scheme, the total number of particles required for N_{sep} groups of N_{tet} tetrads is $N_P = N_{\text{tet}}(1 + 3N_{\text{sep}})$. It is also clear from Figure 3.1 that each tetrad has six distinct pairs of particles; three of them consist of two particles initially separated by a distance of r_0, and the other three pairs are made up of two particles initially separated by $\sqrt{2}r_0$. The labeling in Figure 3.1 is maintained for each particle in a

tetrad throughout the simulation such that a given particle pair in the tetrad initialized at r_0 has a time dependent separation vector $\mathbf{r}(t) = \mathbf{X}^{(m)}(t) - \mathbf{X}^{(1)}(t)$, $m = 2, 3, 4$.

The volume of a tetrahedron V with vertices at $\mathbf{X}^{(\alpha)}$, $1 \leq \alpha \leq 4$, is

$$V = \frac{1}{6} \left| \left(\mathbf{X}^{(2)} - \mathbf{X}^{(1)} \right) \cdot \left[\left(\mathbf{X}^{(3)} - \mathbf{X}^{(1)} \right) \times \left(\mathbf{X}^{(4)} - \mathbf{X}^{(1)} \right) \right] \right|. \tag{3.2}$$

The tetrahedron with vertices at the initial particle positions in Figure 3.1 has volume $V_0 = r_0^3/6$. The faces of this tetrahedron fall into two categories: one initially equilateral triangle with sides of length $\sqrt{2}r_0$ and area A equal to $\sqrt{3}r_0^2/2$; and three initially right-angled isosceles triangles with two sides of length r_0, one side of length $\sqrt{2}r_0$ and initial area $A_0 = r_0^2/2$.

We consider the gyration radius R of a cluster of n particles, which is defined as

$$R^2 = \frac{1}{2n} \sum_{\alpha=1}^{n} \sum_{\beta=1}^{n} \left| \mathbf{X}^{(\beta)} - \mathbf{X}^{(\alpha)} \right|^2. \tag{3.3}$$

Interpreting the tetrahedron in Figure 3.1 as a cluster of four particles and its triangular faces as distinct three-particle clusters, we see that the tetrad of particles initially has $R_0 = 3r_0/2$. Its three-particle subset corresponding to the equilateral triangular face has an initial gyration radius of $R_0 = \sqrt{2}r_0$; each of the initially right-angled triangles makes up a three-particle cluster with $R_0 = 2r_0/\sqrt{3}$.

3.1.2 Simulation parameters

In Chapter 2 we have presented an established method for tracking fluid particles in an instantaneous velocity field of isotropic turbulence inside a periodic domain of length 2π on each side. Since viscosity acts to dissipate turbulent kinetic energy at the small scales, the turbulence must be maintained by adding energy to the large scales through some mechanism of artificial forcing. Throughout the course of this work we have employed two schemes for artificially forcing the large scales in a manner consistent with the desired homogeneity and isotropy of the turbulence: the stochastic forcing method of Eswaran & Pope [1] and the method of Donzis & Yeung [2], which entails freezing the energy spectrum in the lowest few wavenumber shells at values obtained by the forcing of Eswaran & Pope [1]. Both of these schemes are nominally stationary and consistent with isotropy, but the

scheme of Donzis & Yeung [2] has the advantage of reducing the time-variability of space-averaged statistics such as the turbulent kinetic energy and mean dissipation rate. This statistical variability and a method of adjusting for it will be revisited after an outline of the major parameters that characterize the individual simulations.

The fluid kinematic viscosity ν, domain size and forcing parameters roughly determine the range of scales. The number of grid points in each direction N is chosen to keep the spacing between two points at about 2η, where the Kolmogorov length scale η characterizes the smallest dissipative scales and is defined to be

$$\eta = \left(\frac{\nu^3}{\langle\varepsilon\rangle}\right)^{1/4}. \tag{3.4}$$

Due to the low-wavenumber forcing, these flows are nominally stationary, and the time-averaged Taylor-scale Reynolds number R_λ is used to quantify their range of scales.

In each simulation we have chosen fixed values of the initial separation r_0 that cover a wide range of scales in the flow. Relative dispersion is a non-stationary process, and the significance of the initial separation at different times depends on the dynamical features that the initial conditions imposes on the dispersion at small time. The statistical quality of Lagrangian statistics depends on the number of tetrads N_{tet} tracked for each choice of r_0. As is the case with Eulerian statistics, more particles (representing more degrees of freedom) are needed to adequately sample the wider range of scales of the turbulent fields at higher Reynolds numbers than at lower ones [10].

The Lagrangian integral time scale T_L is defined from the one-particle velocity autocorrelation function. In stationary isotropic turbulence, it is

$$T_L = \int_0^\infty \rho(s)ds, \tag{3.5}$$

where $\rho(s)$ is the autocorrelation function for the fluctuating Lagrangian velocity at time lag s. The ratio of Lagrangian integral time scale T_L to the Kolmogorov time scale ($\tau_\eta = (\nu/\langle\varepsilon\rangle)^{1/2}$) quantifies the range of time scales relevant to the Lagrangian dynamics of the flow. Furthermore, T_L is a useful parameter for scaling the duration of the of the simulation T_{sim}. The ratio T_{sim}/T_L needs to be large in order for the particles in a given tetrad to eventually move independently of one another.

We have listed these parameters for the simulations studied in this work in Table 3.1. Initial separations are collected into Table 3.2. These choices result in a decade of R_λ and, for some simulations, about three decades of initial separation. As the range of scales widens at the progressively higher Reynolds numbers attained in the larger simulations, evidence of inertial subrange scaling in several dispersion statistics emerges at intermediate scales of length and time.

Relative dispersion is affected by the large scales of turbulence in many ways (§1.2.2). In DNS, substantial ambiguity can arise from temporal variability of the space-averaged energy dissipation rate in response to forcing applied to the low wavenumber modes. However, this effect may be mitigated by replacing the long-time average of $\langle\varepsilon\rangle$ by the cumulative average due to Sawford *et al.* [50],

$$\langle\varepsilon\rangle(t) = \left(\frac{1}{t}\int_0^t \varepsilon(t')^{1/3}dt'\right)^3, \tag{3.6}$$

where the ε is the instantaneous space-averaged dissipation rate and the one-third power inside the integral sign is motivated by considerations in stochastic modeling [77]. The time dependence of $\langle\varepsilon\rangle$ in Equation 3.6 is hereafter implied, and τ_η is defined using it as well. As noted in Table 3.1, we have further reduced the large-scale variability through the use of the revised forcing scheme of Donzis & Yeung [2] in our largest simulations.

3.2 Results for particle pairs

The scaling regimes encountered in particle pair dispersion are fundamental to the statistical behavior of multiparticle clusters. The deficiencies of direct tests of Richardson-Obukhov motivate us to incorporate the initial conditions into the scaling laws both of particle pair dispersion statistics here and of more sophisticated multiparticle quantities in later chapters.

3.2.1 Richardson-Obukhov scaling and corrections for finite r_0

Applying Kolmogorov similarity principles to particle-pair dispersion produces a prediction of t^3 growth of the mean-squared separation distance, a result known as Richardson-Obukhov scaling given by

$$\langle r^2\rangle = g\langle\varepsilon\rangle t^3, \tag{3.7}$$

which is postulated to hold when $t \gg \tau_\eta$, but before the diffusive regime when $t \gg T_L$ and particles move independently of one another in stationary homogeneous turbulence. Although the Lagrangian integral time scale T_L is associated with the large-scale eddies and parameterizes how long particle positions are correlated with their initial positions, it has less relevance as a time scale for the motion of one particle relative to another. Whether or not two particles may be said to move independently of one another depends on the distance between the two particles at least as much as it depends than the duration a particular pair has been tracked. Evidence of Richardson-Obukhov scaling has been found at times even later than T_L [50], so we do not restrict our attention to $t \ll T_L$ when testing Equation 3.7[32]. The simple test of Equation 3.7, shown in Figure 3.2 for $4 \leqslant r_0/\eta \leqslant 32$ at $R_\lambda \approx 650$ and 1000, illustrates many of the challenges encountered in the study of relative dispersion. In this figure $\langle r^2 \rangle$ has been divided by $\langle \varepsilon \rangle t^3$. If Equation 3.7 is valid and the conditions for Kolmogorov's similarity hypotheses are satisfied in the simulations, then $\langle r^2 \rangle / (\langle \varepsilon \rangle t^3)$ will reach a plateau at Richardson's constant g in an interval of time within the range identified for Equation 3.7.

Figure 3.2 shows that this procedure does not result in a clear plateau at a fixed value of g shared by all of the initial separations even in the DNS at the highest Reynolds number we have yet reached. Although $\langle r^2 \rangle / (\langle \varepsilon \rangle t^3)$ becomes flatter with respect to time at $R_\lambda \approx 1000$ than $R_\lambda \approx 650$, there are still substantial and persistent differences between the height of these nascent plateaus for each of the initial separations in the plot. Although it did not appear in the original formulations of Equation 3.7, it is now generally accepted [32, 50, 56] that the effects of initial particle pair separation distance r_0 must be considered in tests of Equation 3.7 using experimental or simulation data. Normalizing $\langle r^2 \rangle$ is one method; another is to examine displacements $\mathbf{r} - \mathbf{r}_0$. The time scale for the structure of the Eulerian field at the initial separation distance r_0 is also important.

The two-point structure of the Eulerian field at scales comparable to the initial separation r_0 imposes additional length and time scales onto the early relative dispersion process. The Batchelor [16] time scale t_0 is the time scale for an inertial subrange eddy of size r_0. It

is defined to be

$$t_0 = \left(\frac{r_0^2}{\langle \varepsilon \rangle} \right)^{1/3}. \tag{3.8}$$

For inertial-range initial separations satisfying $\eta \ll r_0 \ll L$, where $L = \sigma_u^3/\langle \varepsilon \rangle$ is a length scale for the large eddies, t_0 is the time scale during which the Eulerian field at $t = 0$ dominates the dispersion. Normalizing the time by t_0 for each r_0 is one way of adjusting for initial conditions. We have adopted two methods of adjusting for r_0 in the left-hand-side Equation 3.7 as well. The first is to study the relative displacement vector $\mathbf{r}(t) - \mathbf{r}(0)$ in place of the separation vector $\mathbf{r}$. The second method was introduced by Sawford *et al.* [50] based on the work of Ott & Mann [35] and involves normalizing $\langle r^2 \rangle$ by r_0^2, raising both sides of Equation 3.7 to the 1/3 power and differentiating with respect to t/t_0. It can be shown that the resulting function,

$$\left(\frac{d}{d\,(t/t_0)} \left[\left(\frac{\langle r^2 \rangle}{r_0^2} \right)^{1/3} \right] \right)^3. \tag{3.9}$$

which we refer to as a "cubed-local-slope" (CLS) of $\langle r^2 \rangle$, will approach a plateau with height equal to Richardson's constant g under the conditions for inertial subrange scaling in Equation 3.7. We now apply these two methods successively to the pair separation statistics and demonstrate clearer evidence of Richardson-Obukhov scaling than is obtainable from direct observations like those in Figure 3.2.

3.2.2 Relative displacement statistics

We introduce the mean-square relative displacement magnitude $\langle |\mathbf{r} - \mathbf{r}_0|^2 \rangle$ using the longer simulation at $R_\lambda \approx 650$ (Table 3.1) as an example in Figure 3.3, which is a plot of the square root of this quantity normalized by the Kolmogorov length scale η vs Kolmogorov-scaled time t/τ_η. At small time, $\langle |\mathbf{r} - \mathbf{r}_0|^2 \rangle$ grows quadratically with time at all initial separations. This is due to the early rectilinear motion of the particles. In the limit $t/t_0 \to 0$, which is called the ballistic regime, the displacement $\mathbf{r} - \mathbf{r}_0$ is proportional to the difference in the Eulerian velocities at $\mathbf{X}_0^{(2)}$ and $\mathbf{X}_0^{(1)}$ (for example) at $t = 0$. The structure of the Eulerian velocity field at $t = 0$ thus determines $\langle |\mathbf{r} - \mathbf{r}_0|^2 \rangle$ at infinitesimally small time, and, for particle pairs with separation r_0 along the coordinate axes, this means (Yeung & Borgas

[49])

$$\langle |\mathbf{r}-\mathbf{r}_0|^2 \rangle = \left[D_{LL}(r_0) + 2D_{NN}(r_0)\right] t^2, \quad \begin{cases} t \ll \tau_\eta, & r_0 \leqslant \eta \\ t \ll t_0, & \eta \ll r_0 \ll L \end{cases} . \tag{3.10}$$

where $D_{LL}(r_0)$ and $D_{NN}(r_0)$ are Eulerian longitudinal and transverse structure functions of the velocity [70]. For $r_0/\eta \leqslant 1$, we use the standard relations for the structure function in the dissipation range of isotropic turbulence and substitute $D_{NN}(r_0) = 2D_{LL}(r_0) = 2r_0^2\langle(\partial u_1/\partial x_1)^2\rangle$ into Equation 3.10. The isotropy relation [70]

$$\langle \varepsilon \rangle = 15\nu\langle(\partial u_1/\partial x_1)^2\rangle = 15\nu\frac{\lambda^2}{\sigma_u^2}, \tag{3.11}$$

where λ is the Taylor scale, is used to derive the following relationship [49]:

$$\frac{\langle |\mathbf{r}-\mathbf{r}_0|^2 \rangle^{1/2}}{\eta} = \frac{1}{\sqrt{3}}\frac{r_0}{\eta}\frac{t}{\tau_\eta}, \tag{3.12}$$

which appears as a dotted line in Figure 3.3 for dispersion at $r_0/\eta = 1/4$.

Subtracting off the initial separation vector $\mathbf{r}_0$ is not a complete adjustment for initial conditions since τ_η is not the time scale of the ballistic regime for $r_0 \gg \eta$. As is the case in the compensated plot of $\langle r^2 \rangle$ in Figure 3.2, there are still substantial differences between $\langle |\mathbf{r}-\mathbf{r}_0|^2 \rangle^{1/2}$ at different values of r_0, making it difficult to identify regions of scaling proportional to $t^{3/2}$ (square root of Equation 3.7) in Figure 3.3. When $t \gg T_L$ ($T_L/\tau_\eta \approx 52.7$ in Figure 3.3 for this case at $R_\lambda \approx 650$ according to Table 3.1), these differences diminish as the particles in a given pair are spread so far apart by the turbulence that their velocities become independent of one another. The asymptotic regime when this behavior occurs is called the diffusive regime since, being uncorrelated from their initial locations as well, the statistics of pair displacement may be obtained from considering the statistics of $\mathbf{X}^{(1)}$ and $\mathbf{X}^{(2)}$ separately. Each particle in a pair then follows Taylor's [11] single-particle diffusion equation, which states

$$\langle |\mathbf{X}-\mathbf{X}_0|^2 \rangle \approx 6\sigma_u^2 T_L t, \quad t \gg T_L, \tag{3.13}$$

due to the components of $\mathbf{X}$ having identical independent Gaussian distributions. Applying Equation 3.13 to both particles, adding the contributions of each of the two particles, and

rearranging (making use of Equation 3.11) gives the result [44]

$$\frac{\langle|\mathbf{r}-\mathbf{r}_0|^2\rangle^{1/2}}{\eta} \approx \frac{(12R_\lambda)^{1/2}}{15^{1/4}}\left(\frac{T_L}{\tau_\eta}\right)^{1/2}\left(\frac{t}{\tau_\eta}\right)^{1/2} \qquad (t \gg T_L)\ , \tag{3.14}$$

which is the dashed line gradually approached by all initial separations in Figure 3.3.

Having identified different physical mechanisms yielding distinct scaling regimes at both very small times (ballistic regime) and very late times (diffusive regime) we return to our search for inertial subrange scaling between these to regimes. We divide $\langle|\mathbf{r}-\mathbf{r}_0|^2\rangle$ by $\langle\varepsilon\rangle t^3$ and plot it against t/t_0 for $R_\lambda \approx 650$ (dashed curves) and 1000 (solid curves) in Figure 3.4 in an effort to estimate Richardson's constant g after adjusting for finite initial separation r_0. In Figure 3.4 we see that dispersion at initial separations $r_0/\eta \geqslant 32$ has the same compensated mean-square relative displacement $\langle|\mathbf{r}-\mathbf{r}_0|^2\rangle/(\langle\varepsilon\rangle t^3)$ at a given value of $t/t_0 \leqslant 1$. This collapse is consistent with inertial subrange scaling in the ballistic regime $t \ll t_0$ for $\eta \ll r_0 \ll L$ initial separations in the inertial subrange [16]. The dotted line at $(t/t_0)^{-1}$ in the compensated plot in Figure 3.4 corresponds to Equation 3.10 evaluated in the inertial subrange under Kolmogorov's 1941 hypotheses, giving

$$\langle|\mathbf{r}-\mathbf{r}_0|^2\rangle = \frac{11}{3}C\left(\langle\varepsilon\rangle r_0\right)^{2/3}t^2, \quad t \ll t_0, \quad \eta \ll r_0 \ll L\ , \tag{3.15}$$

where $C \approx 2.13$ is the Kolmogorov constant for the Eulerian longitudinal second-order velocity structure function [78, 79]. The ballistic regime for initial separations in the inertial subrange is sometimes called the Batchelor regime [32] and has been encountered in experiments [38] and simulations [50].

At times after t_0, dispersion at the largest initial separations at these two Reynolds numbers (650 and 1000), $r_0/\eta = 128$ and 512, approaches the diffusive regime, and $\langle|\mathbf{r}-\mathbf{r}_0|^2\rangle/(\langle\varepsilon\rangle t^3)$ reaches $(t/t_0)^{-2}$ (not shown) at $R_\lambda \approx 650$, $r_0/\eta = 512$. Since these initial separations are themselves at the upper limit of the inertial subrange at both of these values of R_λ, there is not much time after the end of the ballistic regime before the particles in a given pair become so widely dispersed that they move independently of one another. Stated another way, there is not sufficient scale separation between t_0 and T_L for an inertial subrange to develop. The transition to the diffusive regime is the only reason for departures from a locus of curves that approach t^3 scaling (a plateau in the compensation used in Figure 3.4) after

about 10 Batchelor times. It is delayed to later Batchelor-scaled time t/t_0 as smaller inertial subrange initial separations are considered. Considered together, an inflection point in the compensated mean-squared relative displacement at about $t/t_0 = 40$ is shared by dispersion at $8 \leqslant r_0/\eta \leqslant 32$ at $R_\lambda \approx 1000$, and the height of this inflection point is associated with Richardson's constant $g \approx 0.56$ (dashed horizontal line in Figure 3.4). This value reinforces the result of Sawford *et al.* [50] with data at $R_\lambda \approx 1000$. Before continuing, we note that the logarithmic scales of Figure 3.4, strictly speaking, do not allow us to determine g this accurately; this plot of the mean-squared relative displacement is at best consistent with $g \approx 0.56$. The method in the next subsection is the more precise source of this estimate.

The smallest initial separations in Figure 3.4 have compensated mean-square relative displacement curves that terminate at the largest values of t/t_0. The Batchelor time is less meaningful for dissipation-range initial separations (except for $r_0/\eta = 1$, for which $t_0 = \tau_\eta$), but including $r_0/\eta \sim O(1)$ in Figure 3.4 illustrates the approach of the local maximum in $\langle |\mathbf{r} - \mathbf{r}_0|^2 \rangle / (\langle \varepsilon \rangle t^3)$ for $t \gg t_0$ towards $g \approx 0.56$ at higher Reynolds number. This trend was observed by Sawford *et al.* [50] for $38 \leqslant R_\lambda \leqslant 650$ and is identified with nascent inertial subrange scaling, even for dissipation-range initial separations.

3.2.3 Cubed-local-slope plots

Plotting compensated relative displacement statistics as functions of Batchelor-scaled time (Figure 3.4) has improved our ability to estimate Richardson's constant g in spite of dissipation-range contamination at small initial separations and the observation that the Batchelor regime ($t \ll t_0$) overlaps the diffusive regime ($t \gg T_L$) at large initial separations even at the highest Reynolds numbers available in our simulations. Nevertheless, there is still considerable uncertainty in estimating g from a plot such as Figure 3.4 due to the subtraction required in each component of the separation vector to get the relative displacement as well as the wide range of values that arise in dividing by t^3. Ott & Mann [35] proposed examining $\langle r^2 \rangle^{1/3}$ and fitting straight lines to this quantity in the hopes of finding time intervals in which $\langle r^2 \rangle^{1/3} = (g \langle \varepsilon \rangle)^{1/3} t$. Sawford *et al.* [50] differentiated $\left(\langle r^2 \rangle / r_0^2 \right)^{1/3}$ with respect to the Batchelor-scaled time t/t_0. The cube of such a derivative is given in

Equation 3.9 and is called the "cubed-local-slope" of $\langle r^2 \rangle$ (CLS($\langle r^2 \rangle$)). We now show how these derivatives are powerful tools in the study of multiparticle relative dispersion by using them to further refine our estimates of Richardson's constant.

In Figure 3.5 we show CLS($\langle r^2 \rangle$) at $R_\lambda \approx 650$ and 1000 at all initial separations given in Table 3.2. In general, for each r_0, the CLS starts from 0 in the limit $t/t_0 \to 0$ and increases to a maximum before decreasing slightly. There is some evidence of an inflection point shared by both r_0/η =16 and 32 at $R_\lambda \approx 1000$. The height of this inflection point is even closer to 0.56 than could be inferred from the relative displacement plot in Figure 3.4. The noisy plateau behavior of CLS($\langle r^2 \rangle$) at $r_0/\eta = 8$ could be associated with inertial subrange scaling, but since we saw $\langle r^2 \rangle$ at $r_0/\eta = 4$ grow at a rate faster than t^3 briefly in Figure 3.2, we cannot rule out that the interval of t^3 scaling at $r_0/\eta = 8$ in Figure 3.5 is fortuitous. Furthermore, the inflection point at $g \approx 0.56$ in Figure 3.5 is shared by both $r_0/\eta = 16$ and 32; the height of the plateau for $r_0/\eta = 8$ is not shared by any other initial separations. As was the case for the mean-squared relative displacement in Figure 3.4, the data at $r_0/\eta \geqslant 128$ collapse onto common values of CLS($\langle r^2 \rangle$) until transition to diffusive scaling when CLS($\langle r^2 \rangle$) declines at a rate proportional to $(t/t_0)^{-2}$. For $t \leqslant t_0$ this collapse is due to a shared Batchelor regime for inertial-subrange initial separations. For $t > t_0$, Figure 3.4 implies that the transition between the Batchelor regime and the inertial Richardson-Obukhov regime is also shared unless the diffusive regime interferes prematurely due to insufficiently high T_L/t_0.

For the smallest values of r_0/η (in the dissipation range), there is a narrow peak with height increasing with Reynolds number. As in Sawford *et al.* [50] we infer that, at sufficiently large Reynolds number, these peaks approach the plateau from below. The limited interval during which this result is displayed ($8 \leqslant t/t_0 \leqslant 15$ for $r_0/\eta = 16$ and 32), even at $R_\lambda \approx 1000$, is a reminder of the challenges of finite Reynolds number in the study of relative dispersion. At higher Reynolds numbers, because of a wider range of time scales, this occurs later with respect to t_0.

The effects of forcing and large-scale temporal variability on relative dispersion statistics is demonstrated in Figure 3.6, which shows a comparison of CLS($\langle r^2 \rangle$) at $R_\lambda \approx 650$ for the two different forcing schemes in Table 3.2. It can be seen in the figure that the scaling range

in the simulation (b) with revised forcing of Donzis & Yeung [2] is better defined and has less ambiguity from the choice of intermediate scale values of r_0 than the simulation (a) with the stochastic forcing of Eswaran & Pope [1].

3.3 Gyration radius of clusters of more than two particles

The preceding analysis of relative dispersion of particle pairs extends to dispersion of multiparticle clusters through the gyration radius R through its definition (Equation 3.3) as an average over all possible pairs in the initial tetrad of Figure 3.1. Although it is acted on by the turbulence in the same way that simple pair separation distance is, the gyration radius is a particularly direct and robust measure of the spatial extent, or size, of the cluster. In Chapter 5 we use it extensively to normalize other multiparticle quantities. Therefore, it is useful to relate R to pair statistics through displacements and cubed-local-slopes.

We first present the root-mean-squared (r.m.s.) gyration radius at our lowest and highest R_λ (140 and 1000, respectively, from Table 3.1) in Figure 3.7. The dashed line at $t^{3/2}$ is meant to show that t^3 Richardson-Obukhov scaling in the gyration radius is not any easier to assess without adjusting for initial conditions than it was for mean-squared pair separation in Figure 3.2. In the diffusive regime, however, these adjustments do not matter since the initial conditions are forgotten when $t \gg T_L$, and we supplement the demonstration of diffusive scaling at $R_\lambda \approx 650$ with an analogous derivation for $\langle R^2 \rangle^{1/2}$ that is tested at $R_\lambda \approx 140$ in Figure 3.7. Using 3.3 (with $n = 4$), we see that when $t \gg T_L$, the mean-squared gyration radius is statistically identical to 3/2 times the mean-square pair separation distance. We readily obtain

$$\langle R^2 \rangle \approx 18 \sigma_u^2 T_L t, \quad t \gg T_L. \tag{3.16}$$

The result for the mean-square gyration radius corresponding to the result for mean-square pairwise relative displacement in Equation 3.14 (itself equivalent to mean-square pair separation at late time) can be written as

$$\frac{\langle R^2 \rangle^{1/2}}{\eta} = \frac{(18 R_\lambda)^{1/2}}{15^{1/4}} \left(\frac{T_L}{t_\eta} \right)^{1/2} \left(\frac{t}{t_\eta} \right)^{1/2} \qquad (t \gg T_L) \ . \tag{3.17}$$

Figure 3.7 shows that the results of the DNS at $R_\lambda \approx 140$, a simulation whose duration is almost 20 T_L, are in excellent agreement with the limiting case given by Equation 3.17. Although the DNS at $R_\lambda \approx 1000$ (being only 5 T_L long) is too short to observe such agreement with the diffusive prediction, it does show a systematic trend towards it.

3.3.1 Relative displacement statistics

The particle displacements (obtained by subtracting off the initial positions) can be substituted for $\mathbf{X}$ in the definition of the gyration radius in Equation 3.3 to form the following displacement gyration radius R_D:

$$R_D^2 = \frac{1}{8}\sum_{m=1}^{4}\sum_{n=1}^{4}|\mathbf{r}^{(mn)} - \mathbf{r}_0^{(mn)}|^2, \tag{3.18}$$

where $\mathbf{r}^{(mn)} = \mathbf{X}^{(m)} - \mathbf{X}^{(n)}$. Although R_D is not commonly studied, we present a few results from it to illustrate the statistical effects of deriving results for particle pair statistics from multiparticle clusters.

Equation 3.18 has four terms where $m = n$ and are thus zero; six terms where $m = 1, n \neq 1, m \neq n$ (or vice versa) corresponding to pairs with the form $|\mathbf{r} - \mathbf{r}_0|^2$; and six terms where $m \neq 1, n \neq 1, m \neq n$ corresponding to pairs with the form $\left|\mathbf{r} - \sqrt{2}\mathbf{r}_0\right|^2$. The mean-square of R_D is thus a multiple of the arithmetic mean of $\langle|\mathbf{r} - \mathbf{r}_0|^2\rangle$ and $\langle\left|\mathbf{r} - \sqrt{2}\mathbf{r}_0\right|^2\rangle$. Applying Equation 3.15 to each of these sets of pairs yields:

$$\begin{aligned} \langle|\mathbf{r} - \mathbf{r}_0|^2\rangle/t^2 &= \frac{11}{3}C\left(\langle\varepsilon\rangle r_0\right)^{2/3} \\ \left\langle\left|\mathbf{r} - \sqrt{2}\mathbf{r}_0\right|^2\right\rangle/t^2 &= \frac{11}{3}2^{1/3}C\left(\langle\varepsilon\rangle r_0\right)^{2/3}, \quad t \ll t_0, \quad \eta \ll r_0 \ll L\ . \end{aligned} \tag{3.19}$$

These relations are tested and compared to Batchelor-compensated forms in $\langle r^2 - r_0^2\rangle$ and $\langle r^2 - 2r_0^2\rangle$ in Figure 3.8 at the largest initial separation ($r_0/\eta = 512$) at $R_\lambda \approx 1000$. We are interested in $\langle r^2 - r_0^2\rangle$ since, in the ballistic regime, the pair separation vector $\mathbf{r}$ can be approximated by a Taylor series,

$$\mathbf{r} \approx \mathbf{r}_0 + \mathbf{w}_0 t \quad , \tag{3.20}$$

and

$$\left\langle|\mathbf{r} - \mathbf{r}_0|^2\right\rangle = \langle r^2 - r_0^2\rangle + 2\langle\mathbf{w}_0 \cdot \mathbf{r}_0\rangle t \approx w_0^2 t^2\ . \tag{3.21}$$

By Equation 3.21, $\langle r^2 - r_0^2 \rangle$ differs from $\langle |\mathbf{r} - \mathbf{r}_0|^2 \rangle$ by the term $\langle \mathbf{r}_0 \cdot \mathbf{w}_0 \rangle$, which vanishes in truly homogeneous turbulence with zero mean velocity at any time. Thus, if $\langle r^2 - r_0^2 \rangle$ and $\langle r^2 - 2r_0^2 \rangle$ don't show Batchelor scaling at early time, it indicates some sort of spurious correlation between initial conditions and relative velocity. Both the r_0 and $\sqrt{2}r_0$ pairs deviate from t^2 scaling in Figure 3.8, but in opposite directions, indicating that $\langle \mathbf{r}_0 \cdot \mathbf{w}_0 \rangle$ for the pairs initially placed along the coordinate axes in Figure 3.1 with initial separation r_0 and the corresponding correlation for the "diagonal" pairs with separation $\sqrt{2}r_0$ are oppositely signed.

We would expect that Batchelor scaling for gyration radius would be a simple matter of adding up Equation 3.19 for the 6 "base" pairs in Equation 3.18 and the 6 "diagonal" pairs and dividing by 8 to get

$$\langle R_D^2 \rangle / t^2 = \frac{11}{4} \left(1 + 2^{1/3}\right) C \left(\langle \varepsilon \rangle r_0\right)^{2/3} . \tag{3.22}$$

Furthermore, we may expect that, since pairs with opposing signs of $\langle \mathbf{r}_0 \cdot \mathbf{w}_0 \rangle$ are included in Equation 3.22, that $\langle R^2 - R_0^2 \rangle$ would be closer to $\langle R_D^2 \rangle$ than $\langle r^2 - r_0^2 \rangle$ is to $\langle |\mathbf{r} - \mathbf{r}_0|^2 \rangle$ since it essentially represents better sampling of our isotropic turbulent field. This is confirmed in Figure 3.9, which compares tests of Batchelor scaling in $\langle R^2 - R_0^2 \rangle$ to Batchelor-compensated $\langle R_D^2 \rangle$ for the same conditions as in Figure 3.8.

Richardson-Obukhov compensation of $\langle R_D^2 \rangle$ (by dividing by $\langle \varepsilon \rangle t^3$ and plotting against Batchelor-scaled time t/t_0) is shown in Figure 3.10 under the same conditions for which $\langle |\mathbf{r} - \mathbf{r}_0|^2 \rangle / (\langle \varepsilon \rangle t^3)$ is shown in Figure 3.4. The horizontal line associated with inertial subrange scaling has been moved from the inference of $g \approx 0.56$ to $3g/2 \approx 0.85$ because each particle pair making up the gyration radius Equation 3.3 is expected to have the same Richardson-Obukhov scaling (Equation 3.7) regardless of whether the particles in the pair were initially separated by r_0 or $\sqrt{2}r_0$. We thus expect the same sort of relationship between the mean-square gyration radius and mean-square pair separation in the inertial subrange that we find in the diffusive regime (Equation 3.17), yielding

$$\frac{\langle R^2 \rangle}{r_0^2} = \frac{3}{2} g \left(\frac{t}{t_0}\right)^3 , \quad t_0 \ll t \ll T . \tag{3.23}$$

3.3.2 Cubed-local-slope plots

By taking the cube root of both sides of Eq. 3.23, differentiating with respect to t/t_0, and taking the cube of the resulting derivative, we can write

$$\left(\frac{d}{d\,(t/t_0)} \left[\left(\frac{\langle R^2 \rangle}{r_0^2} \right)^{1/3} \right] \right)^3 = \frac{3}{2} g \ . \tag{3.24}$$

In analogy with Equation 3.9 for particle-pair separation, we refer to the left-hand-side of Equation 3.24 as the cubed-local-slope (CLS) of $\langle R^2 \rangle$. At sufficiently high Reynolds number the height of this plateau should be independent of r_0 within the inertial range and related simply to Richardson's constant as $3g/2$.

In Figure 3.11 we show data for the left-hand-side of Equation 3.24, at the two highest Reynolds numbers available ($R_\lambda \approx 650$ and 1000). Data for tetrads of small r_0 appear farthest to the right, because their values of t_0 are small. The data for small r_0 at early times under the chosen normalization have no Reynolds number dependence, indicating small-scale universality. In general, for each r_0, the CLS starts from 0 in the limit $t/t_0 \to 0$ and increases to a maximum before it decreases slightly, with some evidence of an inflection point in the case of r_0/η =16 and 32 at the highest Reynolds number shown as was the case for the particle pairs in Figure 3.5. The narrow peaks at small initial separations are interpreted in the same way as those in Figure 3.5 as representing nascent inertial subrange scaling. The numerical value of the plateau is about 0.85, which reinforces estimates of $g \approx 0.56$ for mean-squared pair separation. Considering the level of uncertainty in our simulations, this value of g is in very good agreement with inferences drawn from plots based on two-particle statistics, as in Figure 3.5 for data at the same Reynolds numbers. We also observe that data at early times for large values of r_0 differ very little. Ultimately, at large times, as $\langle R^2 \rangle$ approaches linear growth, the CLS behaves as $(t/t_0)^{-2}$. At higher Reynolds numbers, because of a wider range of time scales, this occurs later with respect to t_0.

3.4 Summary

We have seen the effect that initial conditions, particularly the initial particle separation r_0 along coordinate directions, has on the nonstationary relative dispersion process. Evidence for inertial-range Richardson-Obukhov scaling in the moments of squared pair separation and has been found between the ballistic and diffusive scaling regimes, which are often sufficiently long that they overlap if there is insufficient separation between the scales of independent motion T and the Batchelor time scale t_0 of the Eulerian field at initial separation r_0. Estimates of Richardson constant of $g \approx 0.56$ are reinforced at higher Reynolds number than previously reported in the literature before Hackl *et al.* [64] and using multiparticle statistics.

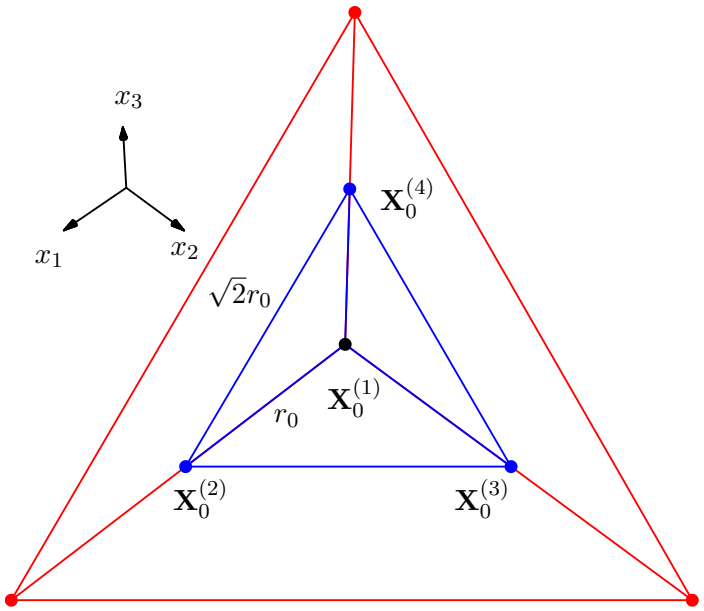

Figure 3.1: Initial placement of particles in a tetrad. A particle is placed at a distance r_0 away from the base particle (located at $\mathbf{X}_0^{(1)}$) along each coordinate axis. The length $\sqrt{2}r_0$ of the diagonal sides of the initially equilateral triangle are also annotated. Another tetrad with larger r_0 is superimposed over the labeled tetrad to show how the base particle shared by both tetrads.

Table 3.1: Major numerical simulation parameters, including number of grid points in each direction, version of forcing used, Taylor-scale Reynolds number averaged over the simulation, and ratios formed among time span of simulation, Lagrangian integral time scale, and Kolmogorov time scale.

N	Forcing	R_λ	T_{sim}/T_L	T_L/τ_η
256	Eswaran & Pope	140	19.2	13.1
256	Donzis & Yeung	140	19.2	13.1
512	Eswaran & Pope	235	22.4	19.8
1024	Eswaran & Pope	390	43.6	31.1
2048	Eswaran & Pope	650	5.4	43.8
2048	Donzis & Yeung	650	11.4	52.7
4096	Donzis & Yeung	1000	5.4	79.6

Table 3.2: Major Lagrangian simulation parameters such as number of tetrads of each choice of initial size and particular choices of initial size r_0 in Kolmogorov units for the cases in Table 3.1.

N	N_{tet}	Forcing	R_λ	r_0/η
256	65536	Eswaran & Pope	140	1/4, 1, 4, 16, 64, 128
256	65536	Donzis & Yeung	140	1/4, 1, 4, 16, 64, 128
512	65536	Eswaran & Pope	235	1/4, 1, 4, 8, 16, 32, 64, 128, 256
1024	65536	Eswaran & Pope	390	1/4, 1, 4, 8, 16, 32, 64, 128, 256
2048	262144	Eswaran & Pope	650	1/4, 1, 4, 8, 16, 32, 64, 128, 256
2048	262144	Donzis & Yeung	650	1/4, 1, 4, 8, 16, 32, 128, 512
4096	262144	Donzis & Yeung	1000	1/4, 1, 4, 8, 16, 32, 128, 512

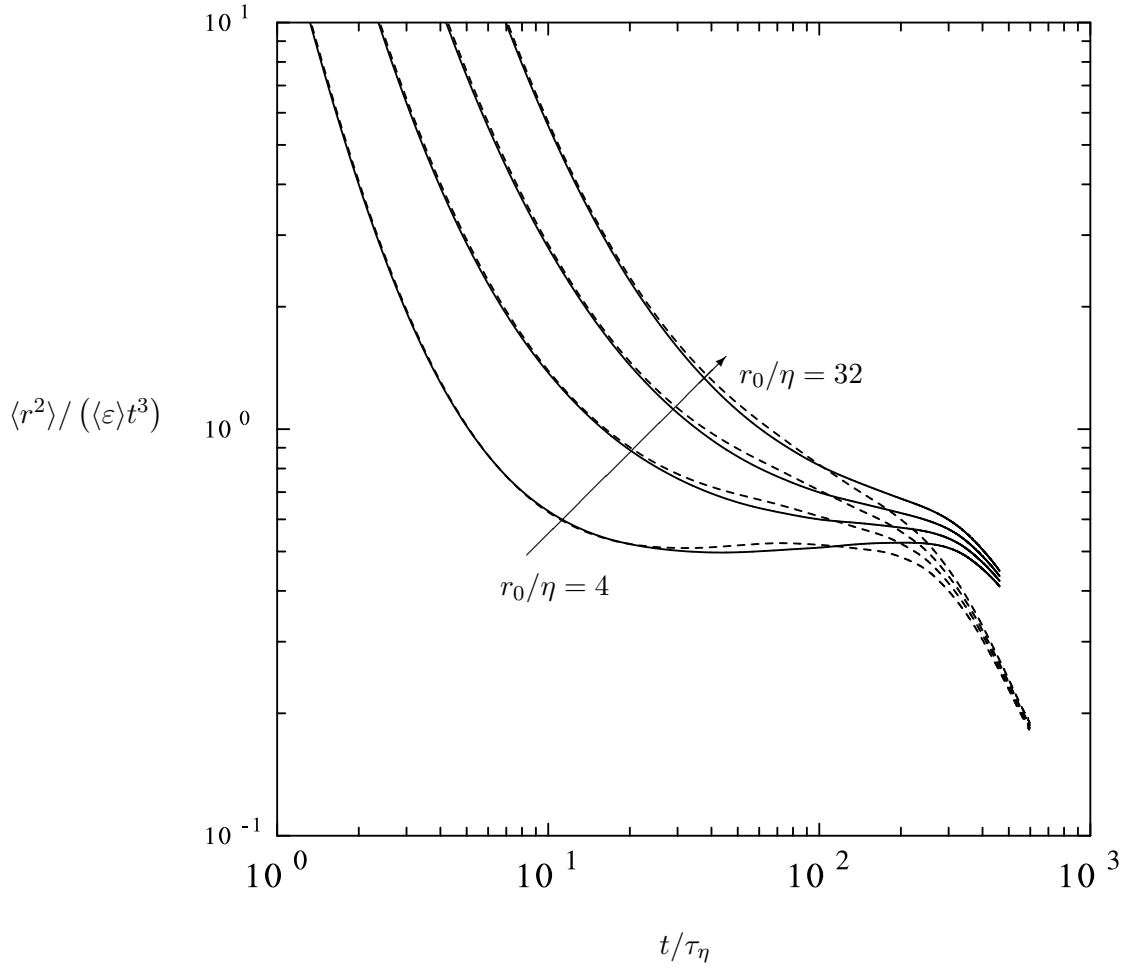

Figure 3.2: Mean-squared pair separation distance normalized by the right-hand side of Equation 3.7 at $R_\lambda \approx 650$ (dashed curves) and 1000 (solid curves). Initial separations are, from the bottom of the plot to the top, $r_0/\eta = 4$, 8, 16 and 32. The arrow indicates increasing initial separation.

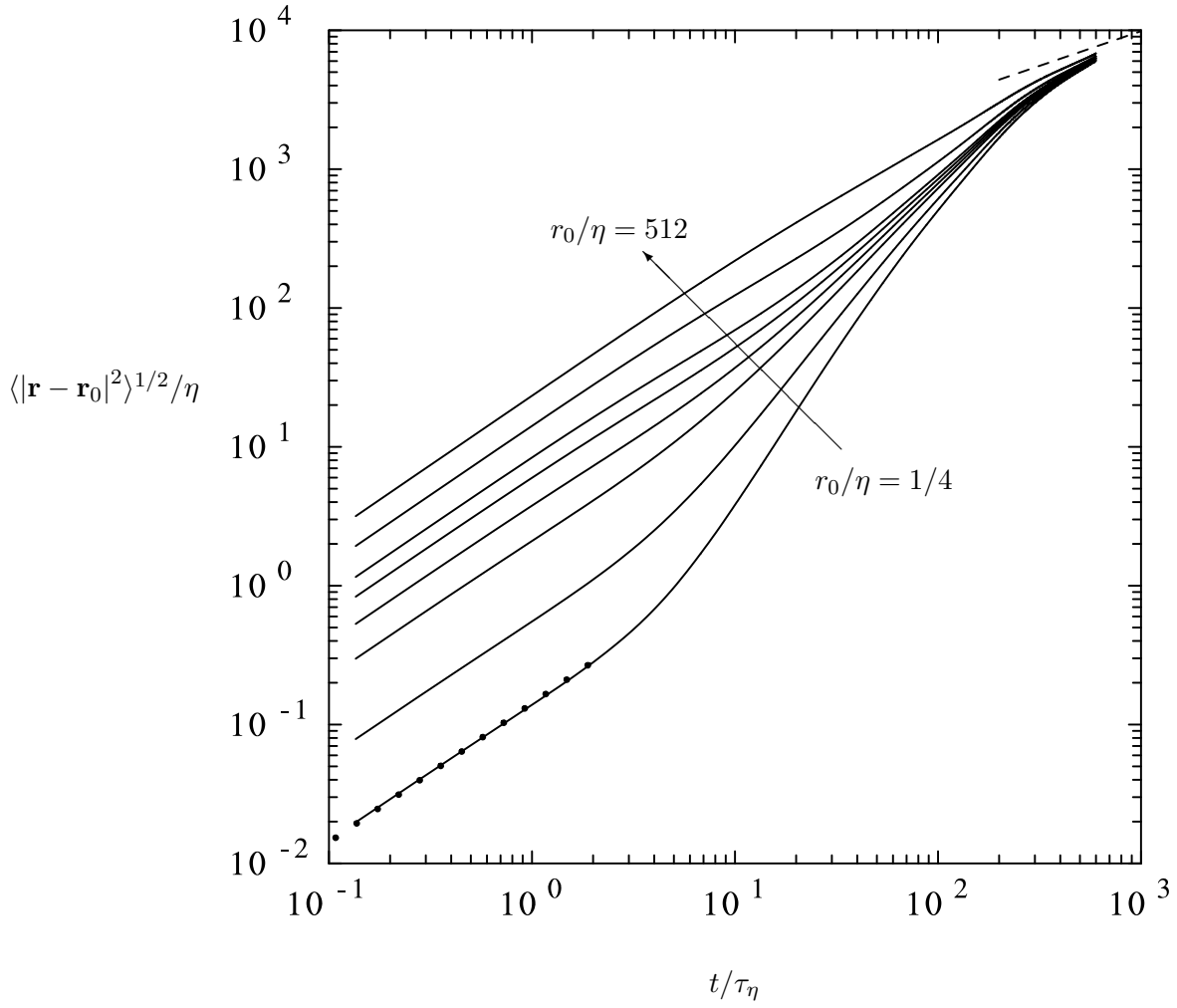

Figure 3.3: Root-mean-square pair displacement $\langle|\mathbf{r}-\mathbf{r}_0|^2\rangle^{1/2}$ vs time under Kolmogorov scaling at $R_\lambda \approx 650$. Initial separations (from bottom to top) are: $r_0/\eta = 1/4$, 1, 4, 8, 16, 32, 128, 512. A dotted line indicates ballistic scaling in the dissipation subrange corresponding to Equation 3.12 for $r_0/\eta = 1/4$. A dashed line is drawn for the diffusive-regime result in Equation 3.14. The arrow indicates increasing initial separation.

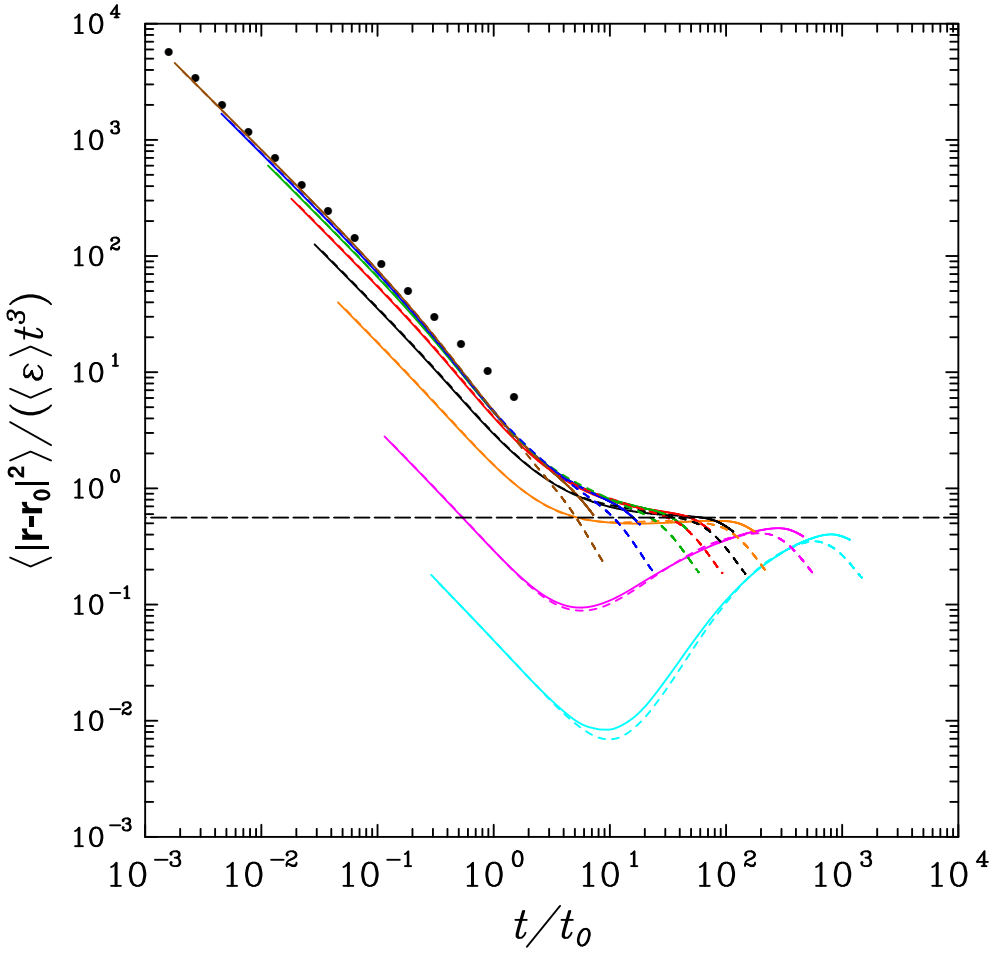

Figure 3.4: Mean-square pair displacement $\langle |\mathbf{r}-\mathbf{r}_0|^2 \rangle$ compensated by the right-hand-side of Equation 3.7 to test for Richardson-Obukhov scaling. Dotted line of slope $(t/t_0)^{-1}$ is the compensated form of the Batchelor scaling given in Equation 3.15. A horizontal dashed line is placed at the estimate of $g \approx 0.56$. Dashed curves: $R_\lambda \approx 650$. Solid curves: $R_\lambda \approx 1000$. Cyan: $r_0/\eta = 1/4$; magenta: 1; orange: 4; black: 8; red: 16; green: 32; blue: 128; brown: 512.

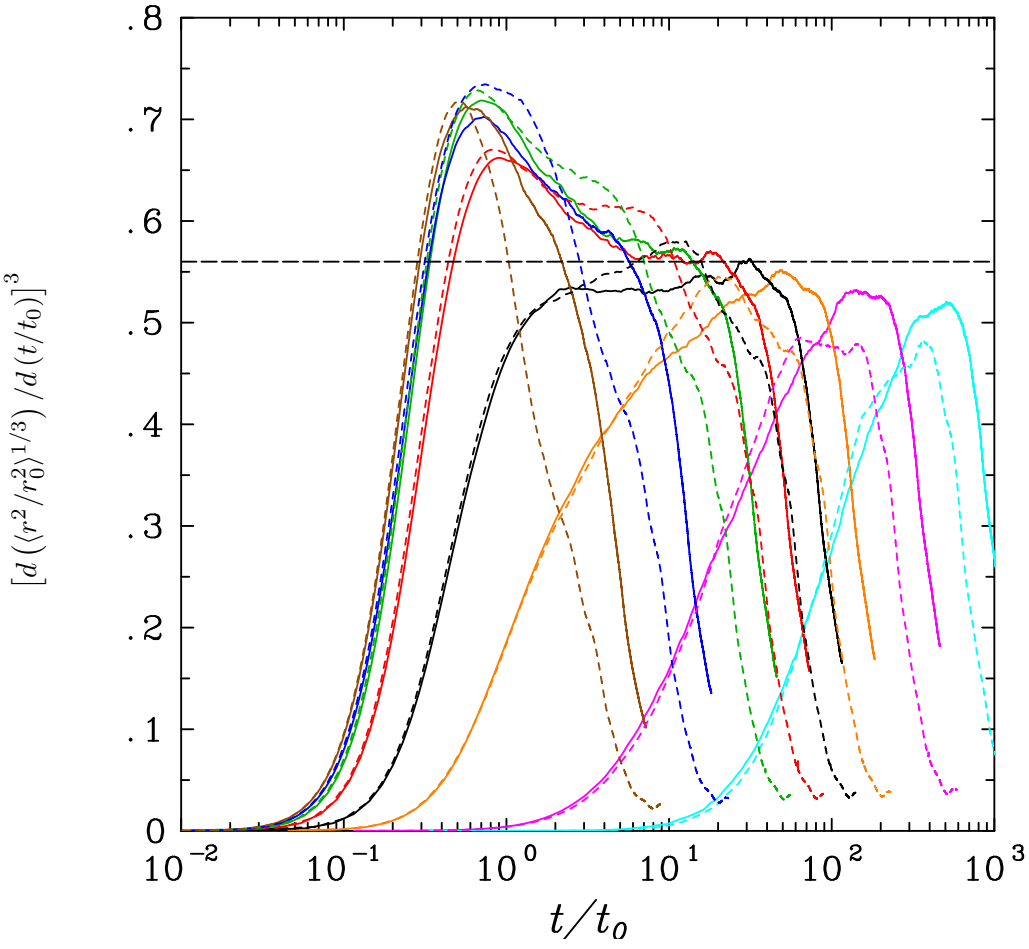

Figure 3.5: The cubed-local-slope of mean-squared pair separation CLS($\langle r^2 \rangle$) at $R_\lambda \approx 650$ (dashed) and 1000 (solid). A horizontal dashed line is placed at the estimate of $g \approx 0.56$. Cyan: $r_0/\eta = 1/4$; magenta: 1; orange: 4; black: 8; red: 16; green: 32; blue: 128; brown: 512.

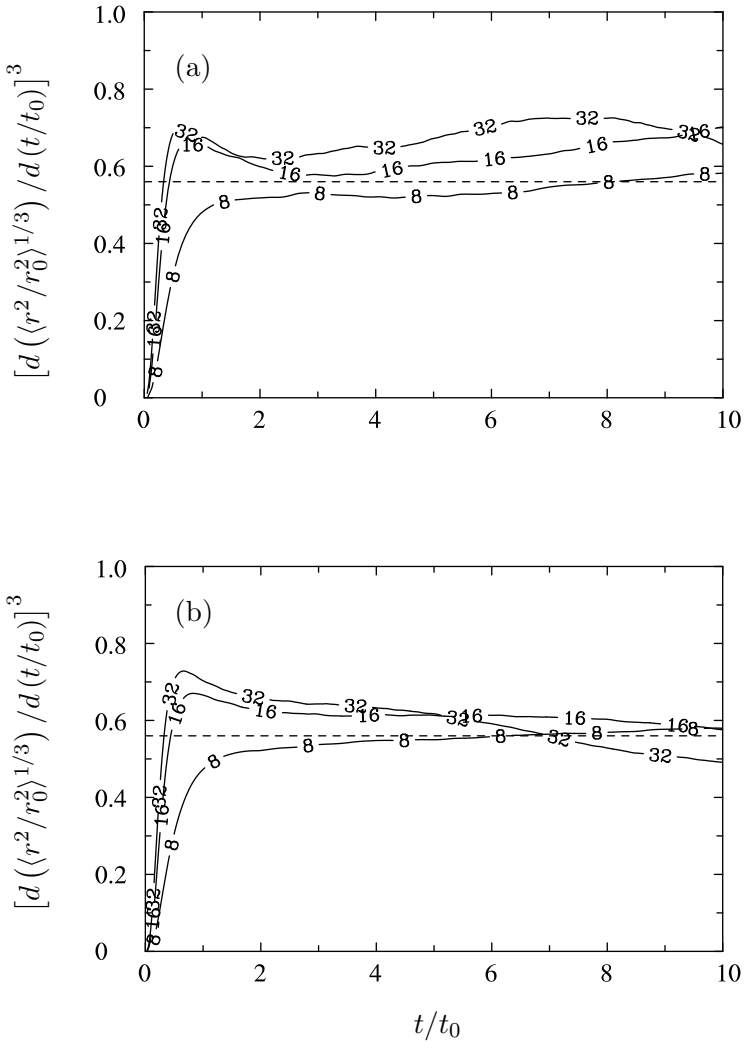

Figure 3.6: "Cubed-local-slope" of normalized mean-squared pair separation $\langle r^2\rangle/r_0^2$ according to the definition in Eq. 13, for two 2048^3 simulations at $R_\lambda \approx 650$ with different forcing schemes: (a) Eswaran & Pope [1]. (b) Donzis & Yeung [2]. Curves are labeled by r_0/η. A dashed line in each plot gives an estimate of Richardson's constant $g \approx 0.56$ from the data. Arrows point in direction of increasing r_0/η.

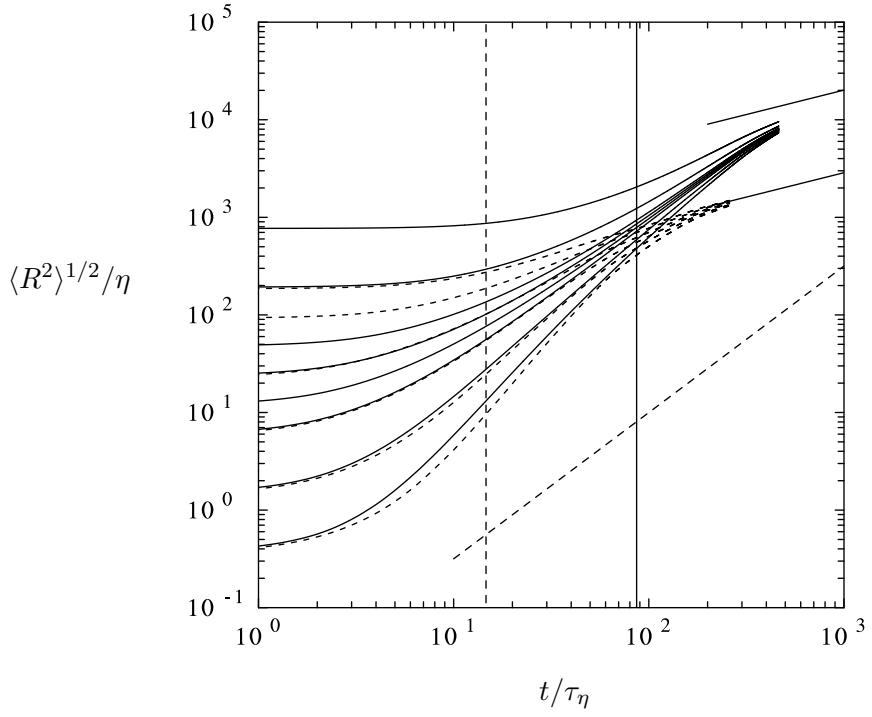

Figure 3.7: Evolution of linear tetrad size based on gyration radius, $\langle R^2\rangle^{1/2}$, normalized by Kolmogorov variables, at $R_\lambda \approx 140$ (dashed curves) and 1000 (solid curves). Curves at each Reynolds number are, going upward, for $r_0/\eta = 1/4, 1, 4, 16, 64, 128$ ($R_\lambda \approx 140$) and for $r_0/\eta = 1/4, 1, 4, 8, 16, 32, 128, 512$ ($R_\lambda \approx 1000$). Dashed line of slope 1.5 provides reference for inference of inertial range scaling. Solid lines showing diffusive regime are computed using Eq. 3.17 with parameters from the simulations.

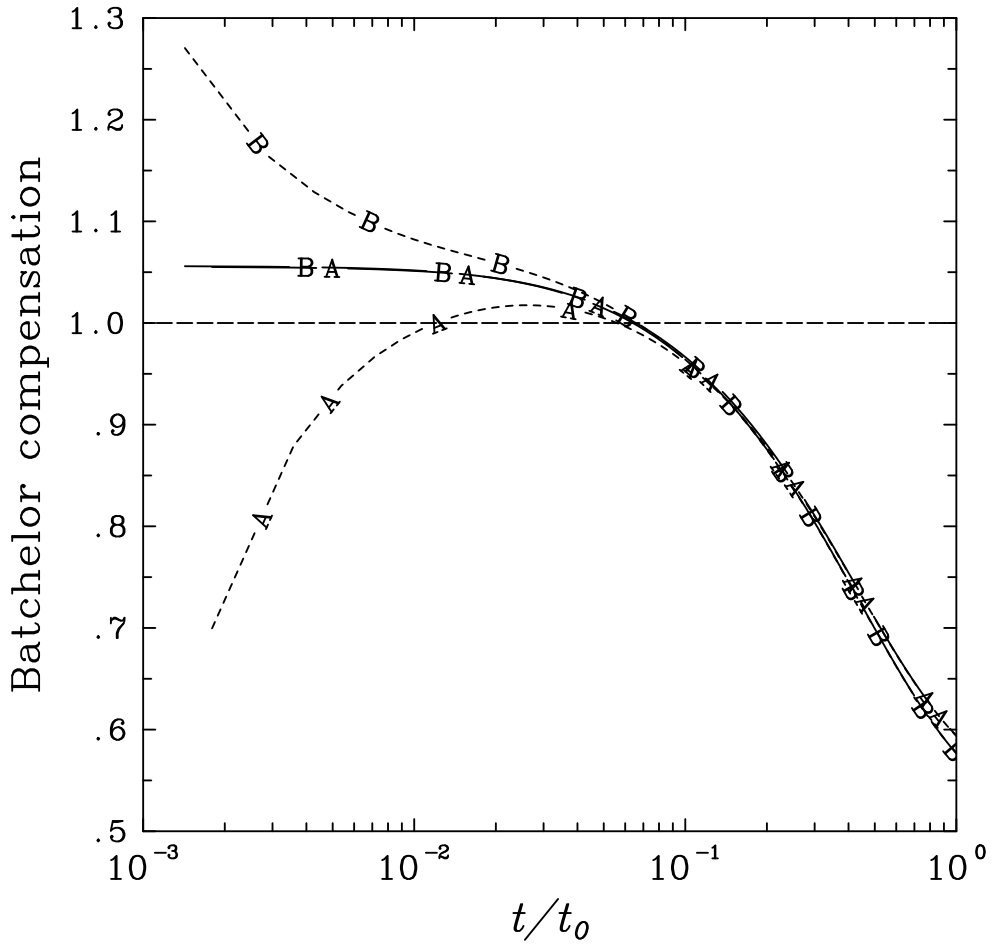

Figure 3.8: Batchelor scaling for all sets of pairs in a given initial tetrad at $r_0/\eta = 512$ at $R_\lambda \approx 1000$. Dashed A: $\langle r^2 - r_0^2 \rangle$ compensated by $\frac{11}{3} C \left(\langle\varepsilon\rangle r_0\right)^{2/3} t^2$. Solid A: $\langle |\mathbf{r} - \mathbf{r}_0|^2 \rangle$ compensated by $\frac{11}{3} C \left(\langle\varepsilon\rangle r_0\right)^{2/3} t^2$. Dashed B: $\langle r^2 - 2r_0^2 \rangle$ compensated by $\frac{11}{3} 2^{1/3} C \left(\langle\varepsilon\rangle r_0\right)^{2/3} t^2$ for "diagonal" pairs. Solid B: $\langle |\mathbf{r} - \sqrt{2}\mathbf{r}_0|^2 \rangle$ compensated by $\frac{11}{3} 2^{1/3} C \left(\langle\varepsilon\rangle r_0\right)^{2/3} t^2$. Long-dashed line at 1 shows agreement with Batchelor prediction.

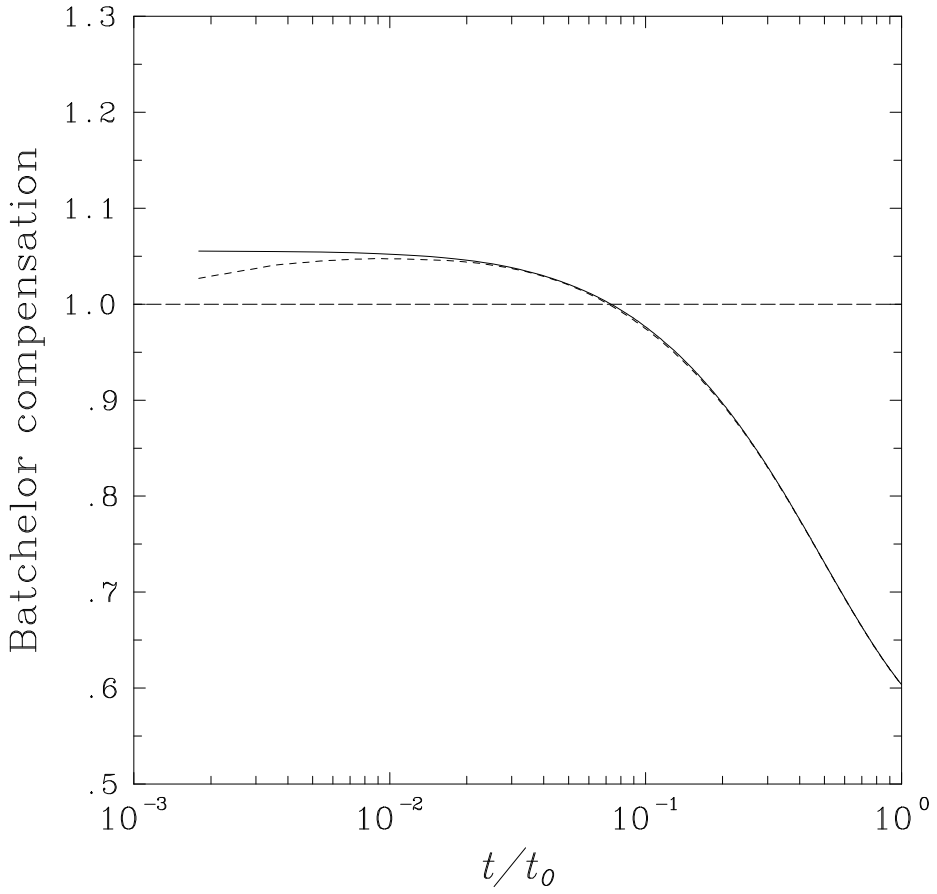

Figure 3.9: Batchelor scaling for mean-square tetrad gyration radius at $r_0/\eta = 512$ at $R_\lambda \approx 1100$. Dashed: $\langle R^2 - R_0^2 \rangle$ compensated by $\frac{11}{4} C \left(1 + 2^{1/3}\right) (\langle \varepsilon \rangle r_0)^{2/3} t^2$. Solid: $\langle R_D^2 \rangle$ compensated by $\frac{11}{4} C \left(1 + 2^{1/3}\right) (\langle \varepsilon \rangle r_0)^{2/3} t^2$. Long-dashed line at 1 shows agreement with Batchelor prediction.

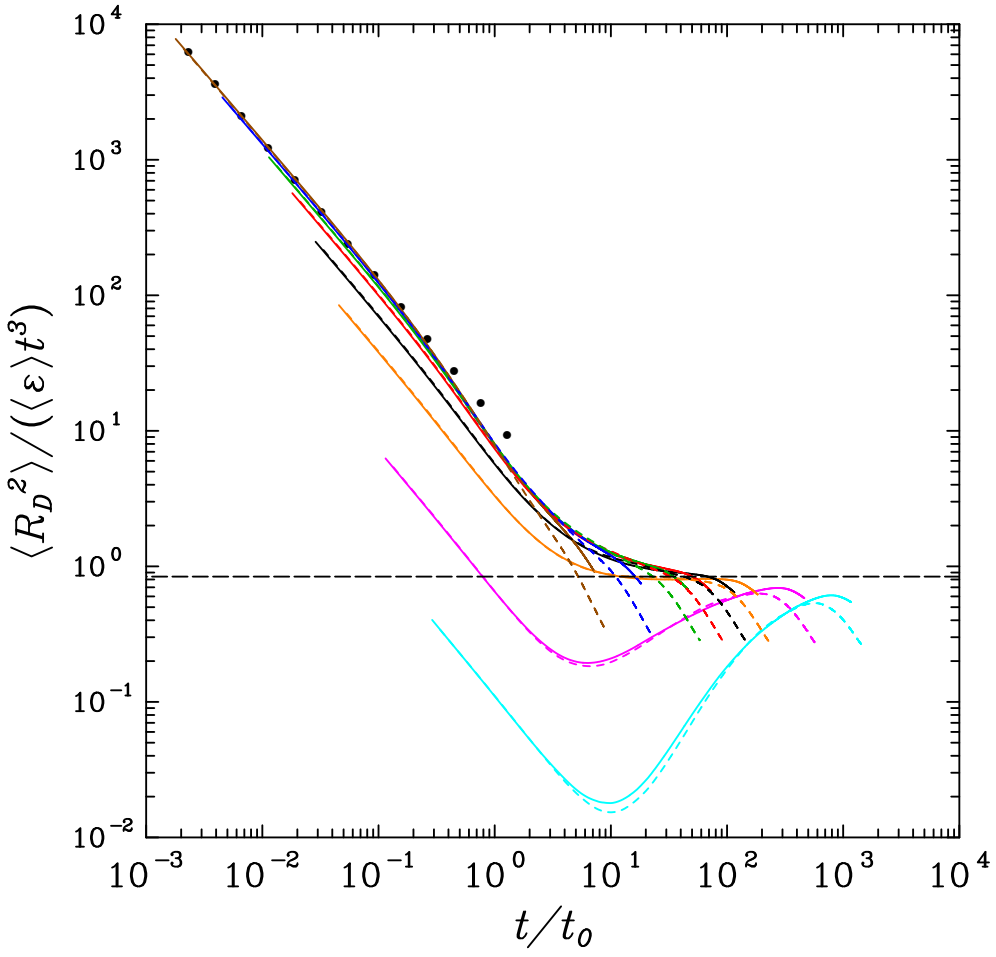

Figure 3.10: Mean-square gyration radius $\langle R_D^2 \rangle$ computed from particle displacements compensated by Richardson-Obukhov scaling under the same conditions as Figure 3.4. Dotted line of slope $(t/t_0)^{-1}$ is the compensated form of the Batchelor scaling given in Equation 3.22. Long-dashed line at estimate $3/2g \approx 0.85$.

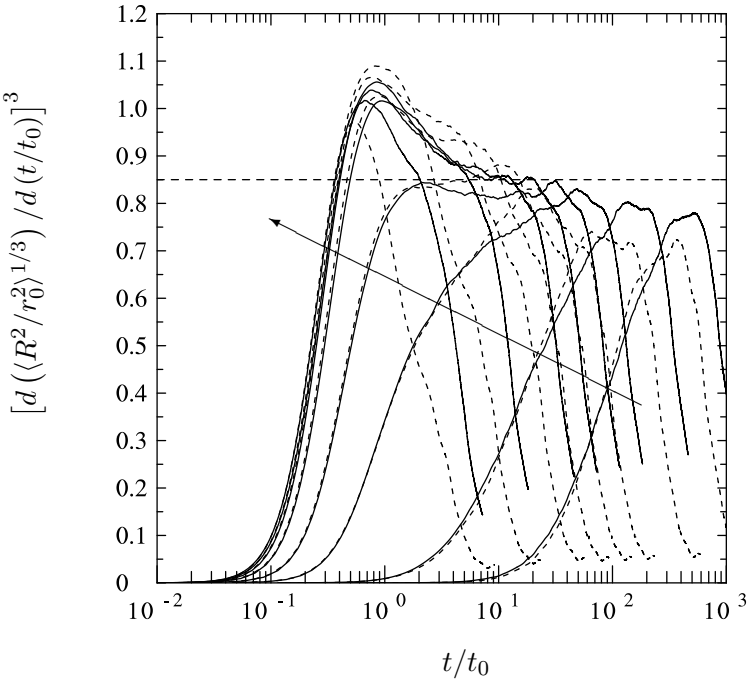

Figure 3.11: Cubed-local-slope for normalized mean-square gyration radius $\langle R^2\rangle/r_0^2$ at $R_\lambda \approx 650$ (dashed curves) and 1000 (solid curves). In both cases data for $r_0/\eta = 1/4$, 1, 4, 8, 16, 32, 128 and 512 are shown. Dashed horizontal line corresponds to $3g/2 \approx 0.85$. Curves move to the left with increasing r_0/η. The arrow indicates increasing initial separation.

CHAPTER IV

STATISTICAL GEOMETRY OF MULTIPARTICLE RELATIVE DISPERSION

Both three- and four-particle clusters (namely, triangles and tetrads) contain important information on size and shape which can be quantified by more than one measure in each case. The study of tetrads is of special interest since it is the minimum configuration that has a volume and contains a rich amount of shape information appropriate in three-dimensional space.

The particle pair separation statistics in Chapter 3 have slow transitions out of the ballistic regime and, at later times, into the diffusive regime that obscure the possibility of inertial range scaling. Signs of inertial range scaling for the mean-squared pair separation distance and mean-squared tetrad gyration radius emerge only very gradually with R_λ in Chapter 3. It seems reasonable to expect requirements for scale similarity in the statistics of more geometrically sophisticated multi-particle quantities to be at least as stringent as they are for the particle pair statistics, if not more so. However, data from both experiment [61, 39, 63] and numerical simulation [45, 62, 80] suggest trends towards statistical invariance of geometric features of three- and four-particle clusters over a limited range of intermediate time intervals. In other words, previous investigations have raised the possibility that the statistics of tetrad shape may, in general, exhibit more robust scaling behavior than the statistics of tetrad size. This chapter is concerned with how to characterize the asymptotic states of shape parameters at high Reynolds numbers.

This chapter begins with the mathematical characterization of the shapes of three- and four-particle clusters through the moment-of-inertia tensor. We then compare the simulation results for mean tetrahedron volume and mean eigenvalues of the dispersion tensor for four-particle clusters to a few experiments and other simulations in the literature. The

statistics of measures of shape, as considered in this chapter, are seen to display different trends in the Reynolds number dependence and approach towards asymptotic states compared with statistics of measures of size in Chapter 3. Results for triangles (i.e. three-particle clusters) are discussed as well.

4.1 Mathematical background and definitions

In general, a cluster consists of n particles with instantaneous positions $\{\mathbf{X}^{(1)}, \mathbf{X}^{(2)} ... \mathbf{X}^{(n)}\}$ at time t. For homogeneous isotropic turbulence these position vectors are identically distributed while their different coordinate components are all mutually independent. Each of $n-1$ reduced separation vectors, called $\boldsymbol{\rho}^{(m)}$, expresses the position of the $(m+1)^{\text{th}}$ particle relative to the center of mass of the first m particles. These reduced separation vectors are defined to be

$$\boldsymbol{\rho}^{(m)} = \sqrt{m/(m+1)} \left(\mathbf{X}^{(m+1)} - \frac{1}{m} \sum_{i=1}^{m} \mathbf{X}^{(i)} \right), \quad 1 \leqslant m \leqslant n-1 \ , \tag{4.1}$$

where the coefficients have been chosen such that each $\boldsymbol{\rho}^{(m)}$ would have the same variance as the position vector of a single fluid particle if all position vectors involved were independent. In §3.2.2, we see that this limiting case occurs at very large times in homogeneous turbulence. When most particles are far enough apart from each other that their velocities become independent of each other, while all of the reduced separation vectors become statistically orthogonal to each other as well.

For turbulence in d-dimensional space each of the reduced separation vectors defined above will have d components. We define a $d \times (n-1)$ matrix $\mathcal{G}$ with each column being one of the $n-1$ separation vectors. The singular value decomposition of $\mathcal{G}$,

$$\mathcal{G} = U \Sigma W^T \ , \tag{4.2}$$

where U is a $d \times d$ orthogonal matrix, Σ is a $d \times (n-1)$ diagonal matrix of non-negative numbers and W is a $(n-1) \times (n-1)$ orthogonal matrix, provides the following description of the geometrical configuration of the cluster. The matrices U, Σ and W, represent, respectively, orientation in physical space, scaling along the coordinate axes, and orientation in the pseudo-space defined by the labeling of the reduced separation vectors. Two further

tensors that can be formed from $\mathcal{G}$ are $G = \mathcal{G}\mathcal{G}^T$, which is the moment of inertia tensor, and $C = \mathcal{G}^T\mathcal{G}$, which we refer to as the dispersion tensor. It can be shown [81] that G and C have the same non-zero eigenvalues, and the diagonal elements of Σ are just the square roots of these non-zero eigenvalues.

A fully rigorous specification of the geometry of an n-particle cluster can be made using the so-called Euler parameterizations [82]. This consists of $n-1$ eigenvalues of the tensor G (or C) defined above and $(n-1)(n-2)/2$ Euler angles which define rotation in $(n-1)$-dimensional pseudo-space (while rotations in physical space merely determine the cluster orientation). For tetrads there are three Euler angles, which makes their use very cumbersome and thus we focus mainly on the role of the eigenvalues. However, for triangles there is only one Euler angle, which is much simpler to study and obtain physical insight from.

The matrices $\mathcal{G}$ and $\mathcal{C}$ have $\min(d,(n-1))$ nontrivial eigenvalues, which are all non-negative and can be arranged in descending order as $g_1 \geqslant g_2$.... The trace of $\mathbf{G}$, which is just the sum of the eigenvalues of $\mathcal{G}$, is equal to the square of the n-particle gyration radius (R). In addition to the definition given in Equation 3.3, squared gyration radius has the following relationships with the reduced vectors and $\mathbf{G}$:

$$R^2 = \sum_{\alpha=1}^{n} g_\alpha = \mathrm{Tr}(\mathbf{G}) = \sum_{m=1}^{n-1} |\boldsymbol{\rho}^{(m)}|^2. \tag{4.3}$$

The sum of the eigenvalues represents the size of the cluster, while their ratios, i.e.,

$$I_\alpha = g_\alpha / R^2, \quad (\alpha = 1, 2...n-1) \tag{4.4}$$

(which, by definition, sum to unity) contain useful information about the cluster shape.

Substituting $n = 4$ in Equation 4.1 yields the following hierarchy of three reduced vectors for tetrads [23]:

$$\begin{aligned}
\boldsymbol{\rho}^{(1)} &= \left(\mathbf{X}^{(2)} - \mathbf{X}^{(1)}\right)/\sqrt{2}\ , \\
\boldsymbol{\rho}^{(2)} &= \left(2\mathbf{X}^{(3)} - \mathbf{X}^{(2)} - \mathbf{X}^{(1)}\right)/\sqrt{6}\ , \\
\boldsymbol{\rho}^{(3)} &= \left(3\mathbf{X}^{(4)} - \mathbf{X}^{(3)} - \mathbf{X}^{(2)} - \mathbf{X}^{(1)}\right)/\sqrt{12}\ .
\end{aligned} \tag{4.5}$$

Regardless of the ordering of the vertices, the tetrahedron volume is the absolute value of a vector triple product, i.e., $V = \frac{1}{6}\left|\left(\mathbf{X}^{(2)} - \mathbf{X}^{(1)}\right) \cdot \left[\left(\mathbf{X}^{(3)} - \mathbf{X}^{(1)}\right) \times \left(\mathbf{X}^{(4)} - \mathbf{X}^{(1)}\right)\right]\right|$, and is related to the eigenvalues of $\mathbf{G}$ and $\mathbf{C}$ by

$$V = \frac{1}{3}\left(g_1 g_2 g_3\right)^{1/2} \ . \tag{4.6}$$

While interpretations of the volume are subject to the caveat that $V = 0$ for sheet-like structures (for which $g_3 = 0$) a comparison between its properties and those of the gyration radius is still relevant. In particular, a standard inequality between arithmetic and geometric means ($(g_1 + g_2 + g_3)/3 \geqslant (g_1 g_2 g_3)^{1/3}$) is relevant, and substitution from Equations 4.3 and 4.6 leads to the constraint

$$0 \leqslant V^{2/3}/R^2 \leqslant 3^{-5/3} \ . \tag{4.7}$$

This suggests the dimensionless parameter $V^{2/3}/R^2$, which is denoted by Λ for short, is a convenient measure of shape, as it varies between 0 for sheet-like tetrads of all four particles lying in a plane, to a maximum of $3^{-5/3} \approx 0.16025$ in the case of regular tetrahedra with all sides equal and $g_1 = g_2 = g_3$. The normalized eigenvalues defined in Equation 4.4 can also be used as shape factors, subject to the constraint $I_1 + I_2 + I_3 = 1$. Furthermore, the expression

$$\Lambda = V^{2/3}/R^2 = 3^{-2/3}(I_1 I_2 I_3)^{1/3} \tag{4.8}$$

shows how Λ absorbs information from the shape factors I_1, I_2 and I_3 (of which only two are independent).

For completeness, we note that the sum and product of g_1, g_2 and g_3 are also the first and third invariants of the tensors G and C, whereas the second invariant is $g_1 g_2 + g_2 g_3 + g_3 g_1$, whose square root gives a generalized area, A_t. There is thus a non-linear, but one-to-one relationship between the shape factors I_1 and I_2 and the physical ratios, Λ and A_t/R^2. These ratios, and therefore the shape factors themselves, are measures of the aspect ratio of the tetrad. There are three limiting cases of tetrad shape: namely, $I_1 + I_2 = 1$ (with $I_3 = 0$) for a sheet-like tetrad, $I_1 = I_2 > I_3$ for a pancake-shaped tetrad, and $I_1 = 1$ (with $I_2 = I_3 = 0$) for a needle-like tetrad.

The case of $n = 3$ represents triangles, with no fourth particle, no $\boldsymbol{\rho}^{(3)}$, zero volume, and a moment-of-inertia tensor with two nonzero eigenvalues, $g_1 > g_2$ with $g_3 = 0$. It is clear then that $R = (g_1 + g_2)^{1/2}$, and $I_3 = 0$ while $I_1 + I_2 = 1$. As noted by Castiglione & Pumir [61] (and as shown in Equation 3.3) R^2 is also the average of the squared lengths of each side in the triangle, making the ratio A/R^2 also an additional measure of the aspect ratio. Following Shraiman & Siggia [82] we use

$$w = \frac{4A}{\sqrt{3}R^2} \ , \tag{4.9}$$

where the numerical factors are chosen such that w is the ratio of the area of the triangle to the area of an equilateral triangle of the same scale [83, 84]. In general, w lies between 0 (for collinear triangles of null area) and 1 for equilateral triangles; it is small for triangles of two long sides and one short side. Both I_1 and I_2 are directly related to w, through the exact relationship $I_2 = (1 - \sqrt{1 - w^2})/2$ (and $I_1 = 1 - I_2$).

As we noted above, for triangles one Euler angle is sufficient to specify configuration in pseudo-space and hence fully specify the two degrees of freedom in the shape of a triangle. This Euler angle is defined by [82]

$$\chi = \frac{1}{2} \arctan \left(\frac{2\boldsymbol{\rho}^{(1)} \cdot \boldsymbol{\rho}^{(2)}}{|\boldsymbol{\rho}^{(2)}|^2 - |\boldsymbol{\rho}^{(1)}|^2} \right) \tag{4.10}$$

and expresses the orientation of principal axes in the vector space spanned by $\boldsymbol{\rho}^{(1)}$ and $\boldsymbol{\rho}^{(2)}$. Although different permutations in the numbering of the three vertices lead to different values of χ, a principal branch can be defined such that for each triangle a unique ordering of the vertices exists which will result in a value of χ in the physical branch $[0, \pi/6]$. For equilateral triangles χ is undefined since both the numerator and denominator in the argument of arctan in Equation 4.10 vanish. Both extremes of χ occur for isosceles triangles, with $\chi = 0$ for triangles with two equal sides of much greater length than the third side, and $\chi = \pi/6$ for triangles with equal sides shorter than the third side. We interpret I_1, I_2 and A/R^2 as measures of the aspect ratio, and χ as a measure of the symmetry as reflected in the deviation from an isosceles shape.

4.2 Statistical geometry of tetrahedra

It is well understood that that averaged measures of cluster size (such as gyration radius and, below, volume) will, in an unbounded domain of homogeneous turbulence, always grow without limit as time evolves. In contrast, measures of shape are often by definition confined to a certain range: e.g., I_1, I_2 and I_3 for a tetrad are bounded in the interval [0,1]. The development of highly anisotropic shapes, such as the case of a planar tetrad, is likely to be the result of intense local strain rates acting in certain directions in the flow. However, while some effects of the resulting shape distortion may linger for a finite period of time, such intense strain rates are known to be relatively short-lived [85]. Studies of fluid particle acceleration [86] and the geometry of particle-pair separation vectors [49] also indicate that changes in particle orientation occur more rapidly than changes in inter-particle distance. Together with the boundedness properties, suggest that effects of initial conditions on cluster shapes are much less long-lasting than they are on cluster size. Indeed, the results of this section, as presented below, indicate that measures of shape exhibit asymptotic scaling properties in their statistics at intermediate times more readily than measures of size do.

We now turn our attention to the statistical behavior of multiparticle quantities that describe tetrahedron shape, which is not possible with two-particle statistics and mean-square gyration radius in Chapter 3. After examining statistical features of the tetrahedron volume and the moment-of-inertia eigenvalues g_1 through g_3, we develop the description of tetrahedron aspect ratio through the use of the moments and distributions of Λ, which is related to V by Equation 4.8. More detailed information about the distortion of tetrahedra is then sought in the statistical study of the normalized moment-of-inertia eigenvalues I_1 through I_3 (Equation 4.4). The evolution of these quantities with time and dependencies on initial tetrad size and the Reynolds number are examined in each of the subsections below.

4.2.1 Mean tetrahedron volume and moment-of-inertia eigenvalues

Figure 4.1 shows the growth of volume, in terms of the square root of its two-thirds moment, i.e. $\langle V^{2/3} \rangle^{1/2}$, at the lowest and highest Reynolds numbers ($R_\lambda \approx 140$ and 1000, dashed and solid curves respectively) listed in Table 3.1, scaled by Kolmogorov variables. Vertical

lines in the figure indicate the time scale ratio T_L/t_η, which is, as expected from classical scaling, roughly proportional to R_λ. The choice of $\langle V^{2/3}\rangle^{1/2}$ as a measure of linear size is motivated by the fact that dimensional reasoning based on Equation 3.7 suggests $\langle V^{2/3}\rangle$ should follow an inertial range relationship given by

$$\langle V^{2/3}\rangle = C_V\langle\varepsilon\rangle t^3, \quad \tau_\eta \ll t \ll T, \tag{4.11}$$

where C_V is a universal constant analagous to Richardson's constant g, that is free of intermittency corrections. The corresponding scaling behavior for $\langle V^{2/3}\rangle^{1/2}$ is $t^{3/2}$, which appears as a line of slope 3/2 in Figure 4.1.

In the logarithmic axes chosen here it is natural that significant changes in the mean volume of large tetrads take longer to become readily apparent. However, the mean volume of tetrads of initial size in the dissipative range ($r_0/\eta \leqslant 1$) remains nearly constant for a significant time period, perhaps close to two Kolmogorov time scales. This lack of initial growth is expected, since in the limit of $r_0/\eta \to 0$ the relative velocities between the particles (which determine the rate of change of volume) become proportional to the velocity gradients, and incompressibility implies the rate of volumetric expansion of an infinitesimal volume element must vanish [45]. In this early-time ballistic regime one can expect that lower-order particle-pair statistics are universal with respect to Reynolds number if scaled by Kolmogorov variables. However at higher Reynolds number the growth of volume begins slightly earlier in Kolmogorov-scaled time. This may be a result of some particle pairs in zones of intense velocity gradients (which are intermittent in nature) moving apart much more rapidly than the others. This behavior contrasts with r.m.s. gyration radius $\langle R^2\rangle^{1/2}$ (Figure 3.7), a quantity that does spontaneously grow when $t > 0$, and more rapidly so if r_0 is small.

The same difficulties in assessing Richardson-Obukhov scaling in the Kolmogorov-scaled mean-squared pair separation (Figure 3.2) and displacement (Figure 3.3), as well as mean-squared gyration radius (Figure 3.7) are encountered in $\langle V^{2/3}\rangle^{1/2}/\eta$. It is difficult to attribute the $t^{3/2}$ scaling in such a plot to inertial subrange scaling or transition away from dissipation-range initial separations with mean-square pair displacements that grow faster

than t^3 at the end of the dissipation range. When $t \gg \tau_\eta$, $\langle V^{2/3} \rangle$ also lacks clear separation in time before the gradual onset of long-time diffusive behavior (not quite reached in the simulation at $R_\lambda \approx 1000$), a trait also encountered in pair statistics ($\langle |\mathbf{r} - \mathbf{r}_0|^2 \rangle^{1/2}$) in Figure 3.3) and r.m.s. gyration radius $\langle R^2 \rangle^{1/2}$ (Figure 3.7) when scaled by Kolmogorov variables.

At sufficiently late times application of Taylor's one-particle diffusion results suggests that $\langle V^{2/3} \rangle$ should be proportional to $\sigma_u^2 \, T_L t$. Unlike squared gyration radius (Equation 3.3), volume is cubic in the positions of particles relative to one another; the scaling of moments of powers of V in the diffusive regime is not linearly related to the diffusivity of one particle's displacement (Equation 3.13). Monte-Carlo calculations in which the coordinates of all four particles are independent Gaussian variables indicate the proportionality constant between $\langle V^{2/3} \rangle$ and $\sigma_u^2 \, T_L t$ is about 1.16. As was the case for the r.m.s. gyration radius (Figure 3.7), the DNS at $R_\lambda \approx 140$ is in excellent agreement with the diffusive-regime limit, and the DNS at $R_\lambda \approx 1000$ shows a systematic trend towards it as well.

The CLS of $\langle V^{2/3} \rangle$ is shown in Figure 4.2 at $R_\lambda \approx 1000$ in order to test Equation 4.11. A similar analysis to the one in §3.2.3 (applying Equation 3.9 to $\langle V^{2/3} \rangle$) gives a scaling constant of $C_{V^{2/3}} \approx 0.037$, which is included in Table 4.2. While this scaling constant is much smaller than that (0.85 in Table 4.2) observed for the mean-squared gyration radius in Figure 3.11, the disparity in magnitude is not surprising, since mathematically the ratio $V^{2/3}/R^2$ is always small compared to 1.0; furthermore, the volume may occasionally vanish when one particle passes through the plane on which the other three particles in the tetrad lie.

For more information on structural aspects, we also consider the individual eigenvalues $g_1 \geqslant g_2 \geqslant g_3$ of the moment-of-inertia matrix, whose sum and product give R^2 and V respectively. Figure 4.3 shows the evolution of all three mean eigenvalues, scaled by Kolmogorov variables in the simulation at $R_\lambda \approx 1000$. The behavior is qualitatively similar to that obtained in the DNS of Biferale *et al.*[62] (figure 1 therein). At sufficiently large times, when the tetrad shape distribution has reached an asymptotic state, one can expect the mean values of these three eigenvalues each to evolve similarly to $\langle R^2 \rangle$. This is indeed the

case in this work. However, at small times a relaxation of shape from the prescribed initial conditions must occur. While initially $g_1 = g_2$ due to our choice of initial configurations (Figure 3.1), it is clear that $\langle g_1 \rangle$ becomes much larger than both $\langle g_2 \rangle$ and $\langle g_3 \rangle$ quite rapidly. The period of rapid change of shape apparently starts earlier for tetrads of small r_0/η. Opposing changes occur in $\langle g_3 \rangle$, which decreases to a minimum value before growing again steadily in a manner similar to $\langle g_1 \rangle$ and $\langle g_2 \rangle$. Finally, for each mean eigenvalue, curves for tetrads of different initial sizes converge at very late time as expected in the diffusive limit.

The differences among the eigenvalues seen above suggest the possibility that different mean eigenvalues have different intervals of scaling, which in turn suggests one or more of the eigenvalues may be less susceptible to scale-crossover effects and hence display clearer inertial range scaling than the others. It is useful to extend the cubed-local-slope approach of Equation 3.24 to the mean eigenvalues, by writing

$$\mathrm{CLS}(g_1) = \left(\frac{d}{d\,(t/t_0)} \left[\left(\frac{\langle g_1 \rangle}{r_0^2} \right)^{1/3} \right] \right)^3 , \tag{4.12}$$

with similar expressions for g_2 and g_3. Furthermore if a well-defined Richardson-Obukhov scaling range exists during a time period in which the shape distribution of the tetrads has reached an asymptotic state, we can define three new proportionality constants, such that, for instance, $\langle g_1 \rangle = C_{g,1} \langle \epsilon \rangle t^3$ and similarly for the other eigenvalues. The cubed-local-slopes will then be equal to these new constants, whose sum, i.e., $C_{g,1} + C_{g,2} + C_{g,3}$, should be $3g/2$, which also follows from Equation 3.23.

Figure 4.4 shows results for cubed-local-slopes of the mean tetrad eigenvalues, based on the same data as in Figure 4.3. Appearance of a plateau in this figure indicates t^3 scaling, while the numerical values on the ordinate are measures of sign and magnitude. Since g_1 is the dominant eigenvalue it is not surprising that its local slope behavior resembles that of R^2 (Figure 3.11). Cubed-local-slopes for tetrads of intermediate and large initial sizes rise towards a peak before dropping gradually towards a plateau, which suggests $C_{g,1} \approx 0.72$. On the other hand, for g_2 and g_3, curves for almost all choices of r_0/η appear to show peaks of various widths but at the same heights, thus providing support for a plateau as well, but one which is reached from below. The asymptotic values are close to 0.12 and 0.013 for $C_{g,2}$

and $C_{g,3}$ respectively.

Cubed local slopes have been used to determine inertial subrange scaling constants for relative displacements of particle pairs, tetrad gyration radii, eigenvalues of $\mathbf{G}$ (essentially separation distances along the principal axes of a tetrahedron) and tetrahedron volume, but only after careful adjustment for initial tetrad size and configuration. These results have been collected into Table 4.2. Evidence for their universality in their independence from Reynolds number across intermediate r_0 is even stronger for the normalized quantities introduced in §4.1 that are discussed below.

4.2.2 Features of tetrad shape

We begin with the shape parameter $\Lambda = V^{2/3}/R^2$. In our simulations all tetrads begin with $V = r_0^3/6$ and $R^2 = 9r_0^2/4$, thus giving (via Equation 4.8) $\Lambda = 6^{-2/3}(9/4) \approx 0.1346$, which is relatively close to the upper bound value of 0.16025 noted in §4.1. These parameters are listed in Table 4.1. In general a tetrad of given instantaneous linear size is subject to distortion by velocity fluctuations at scales at or smaller than those of the tetrad. For our tetrads which are initially highly symmetrical with a large value of Λ, the shape distortion causes a decrease in $\langle\Lambda\rangle$ averaged over the entire population of tetrads, before a restoring tendency away from highly anisotropic shapes starts to be felt.

In Figure 4.5 we show the evolution of the mean value of Λ in Batchelor-scaled time, at $R_\lambda \approx 1000$ and including initial tetrad sizes r_0/η from 1/4 to 512. Beyond the early-time decrease, which is mostly a ballistic response to the choice of initial conditions in Figure 3.1, a scaling regime of near-constant $\langle\Lambda\rangle$ emerges in data for $r_0/\eta \leq 128$. For tetrads of initial size $r_0/\eta = 16$, which is most closely identified with inertial range scaling here and in previously-discussed quantities, the observed scaling range for $\langle\Lambda\rangle$ is most evident as a clear level region of height about 0.045 over almost one decade of t/t_0. The scaling region is eventually terminated at later times by an approach to the diffusive range (for $t \gg T_L$, not reached in this particular simulation), where $\Lambda \approx 0.0645$. The inertial range scaling region is also evident, but less extensive, for $r_0/\eta = 32$, and is almost attained

for $r_0/\eta = 128$. For $r_0/\eta > 128$ the tetrads are more strongly influenced by the energy-containing eddies and the transition towards the diffusive range prevents the plateau being attained. For $r_0/\eta < 16$, the tetrads are influenced by dissipation scale motions for a period which increases if r_0/η is further reduced. These dissipation scale motions result in even lower values of Λ, which eventually recover towards the diffusive value at large times. Remarkably, in the transition from the dissipation range to the diffusive regime the curves for these smaller initial separations show an inflection point also at the value 0.045. This provides further support for near-constancy at 0.045 as a marker of inertial range behavior for $\langle\Lambda\rangle$. It is also the first clear indication that, at sufficiently high Reynolds numbers, inertial range scaling can be attained for configurations with initial separations in the dissipation range.

This demonstration of inertial range scaling is reinforced by comparisons with results at other Reynolds numbers. In Figure 4.6 we show the evolution of $\langle\Lambda\rangle$ at $R_\lambda \approx 390$, 650 and 1000 for initial sizes $r_0/\eta = 1$, 4, 16, 128. At $R_\lambda \approx 650$, the curve for $r_0/\eta = 16$ has a plateau at height 0.045, while those for $r_0/\eta = 1$ and 4 show inflection points at that value. It also appears that $R_\lambda \approx 390$ is just sufficiently high for tetrads of $r_0/\eta = 16$ to reach inertial range behavior, while as R_λ increases to 650 and 1000 the extent of the scaling range steadily widens. Figure 4.6 also shows that, for tetrads of small r_0, the early-time behavior of $\langle\Lambda\rangle$ depends only weakly on the Reynolds number. This collapse with respect to R_λ is a consequence of small-scale universality for initial tetrad sizes in the dissipation range. Furthermore, at large times the data at $R_\lambda \approx 390$ and 650 show very good agreement with a diffusive limit given by Monte-Carlo estimates. A key requirement for such close agreement is a very long simulation time period, which can be explained by long-time memory effects in particle displacements [44], although statistical variability in Eulerian flow parameters (such as turbulence kinetic energy and dissipation) in time can also introduce some uncertainties.

While initially all tetrads have the same shape, at any time $t > 0$ there is an evolving distribution of shapes that can be represented by the PDF of Λ. At $t = 0$ this PDF is a delta function at $\Lambda \approx 0.1346$. We are interested in its early time evolution, possible inertial

range scaling and the late-time diffusive limit. Figure 4.7 shows this PDF for tetrads of initial size $r_0/\eta = 16$ at $R_\lambda \approx 1000$ that best represent inertial-range behavior. The data shown are taken at times t/t_0 approximately half a decade apart starting at $t/t_0 = 0.1$, and ending at the last time step in the simulation. At early times (including $t/t_0 = 0.1$ and 0.3) this PDF has a smooth profile skewed to the left, as some samples of Λ much smaller than 0.1346 arise. This form of the PDF indicates a small but nontrivial fraction of tetrads have sides of disparate lengths, which in turn implies a minority of particle pairs are much farther apart than the others, and is also consistent with a large positive skewness in particle-pair separation distance at small and intermediate times [49]. On the other hand some tetrads will also develop values of Λ slightly larger than 0.1346, since some particle pairs initially far apart (and forming the longest sides of a tetrad) may move towards each other slightly at early times [44], making the lengths of each side more nearly equal at $t = 0$.

Figure 4.7 shows that PDFs at $t/t_0 = 3$, 10 and 30 differ very little. In this same time period, the mean of Λ as seen in Figure 4.5 is essentially constant over one decade of Batchelor-scaled time t/t_0, at a value considered representative of the inertial range. The shape of the PDF in this regime is characterized by a positive skewness, and peak probability at a relatively low Λ of about 0.015. It may be said, thus, that tetrads in the inertial range tend to be quite distorted. On the other hand, at large times the PDF of Λ relaxes towards a diffusive asymptotic limit, denoted by open circles in the figure. Although the simulation at $R_\lambda \approx 1000$ is not sufficiently long to attain this limit, a systematic trend towards this large-time asymptote is apparent, as illustrated by the last (dashed) curve at the end of the simulation. It bears mention that simulations run for a sufficiently long time period almost guarantee diffusive-regime scaling.

In addition to tetrads with inertial-range r_0, it is also useful to examine the PDF of Λ for tetrads of initial size in the dissipation range, and to obtain a compare the characteristic shapes of the PDF of Λ in distinct scaling regimes. Accordingly, in Figure 4.8 we show PDF data at different times for $r_0/\eta = 1/4$ in simulation at $R_\lambda \approx 1000$. Based on the evolution of $\langle\Lambda\rangle$ seen in Figure 4.6, we have plotted the PDF at times t/t_0 when $\langle\Lambda\rangle$ first crosses the diffusive range value (despite not showing true diffusive behavior yet), when it attains

its minimum, and when it reaches the inflection point corresponding to the inertial range value ($\langle\Lambda\rangle \approx 0.45$). Although, in general, a given value of the mean does not determine the form of a PDF, we find that the curve that corresponds to $\langle\Lambda\rangle = 0.0645$ nearly coincides with the diffusive range form of the PDF. Since the initial tetrad size is small the PDF becomes shifted strongly towards small Λ as these tetrads become highly distorted. At later times relaxation to a shape closely matching inertial-range forms is clearly seen; indeed, the inertial range shape inferred from this figure is essentially identical to that seen in Figure 4.7 for tetrads with inertial-range initial size. In addition, since the PDFs in the inertial and diffusive regimes rise sharply near $\Lambda = 0$ we have also included (in the inset) a log-log plot, which shows that there is a slope 1/2 behavior for extremely small Λ. Since this behavior is shared by PDFs in different dynamic temporal regimes we conclude that it is of a kinematic nature. Further diagnostics also indicate that this feature can be related mathematically to the fact that the PDF of Λ is nonzero at $\Lambda = 0$.

Since the shape of a tetrad, a three-dimensional object, cannot be fully described by one single parameter, we next turn to the shape factors I_1, I_2 and I_3 (defined in Equation 4.4), of which two are independent since their sum is fixed at unity. Figure 4.9 shows all three mean shape factors from the $R_\lambda \approx 1000$ simulation. Consistent with Figure 4.6, the evolution of these mean shape factors is characterized by a flat scaling range at intermediate times which may be reached as an inflection point in the case of small r_0, followed by a trend towards the diffusive limit at large times. The present high-Reynolds-number data suggest that the mean shape factors in the inertial range are $\langle I_1\rangle \approx 0.83$, $\langle I_2\rangle \approx 0.16$, and $\langle I_2\rangle \approx 0.01$, which are all indicated by horizontal dashed lines in the figure. These values and other inertial-range estimates of moments of shape parameters are summarized in Table 4.3. Again, like the results in Figure 4.6, the same asymptotic values are attained in data at $R_\lambda \approx 390$ and 650 as well. The large disparity among these mean shape factors, especially with $\langle I_1\rangle$ more than 80 times larger than $\langle I_3\rangle$, suggests highly elongated shapes are dominant. One possible scenario is, for instance, the case of one of the particles in a tetrad located at a large distance away from the plane formed by the other three.

Data in the literature are available for comparisons with our results in Figure 4.9,

although only qualitatively. Unlike the case in DNS, in the experiments of Xu *et al.*[63] the tetrads do not all have the same initial shape, and initially the mean shape factors are roughly $\langle I_1 \rangle \approx 0.4$, $\langle I_2 \rangle \approx 0.35$ and $\langle I_3 \rangle \approx 0.25$. Subsequently, as observed in our simulations, both $\langle I_2 \rangle$ and $\langle I_3 \rangle$ decrease, while $\langle I_1 \rangle$ becomes increasingly dominant. Xu *et al.* encountered a stationary period where $\langle I_1 \rangle$, $\langle I_2 \rangle$ and $\langle I_3 \rangle$ are approximately 0.76, 0.21, and 0.03. However, these experimental values are for tetrads with r_0/η in the range 300-600, and are thus more comparable with our results for $r_0/\eta = 512$ which (as seen in Figure 4.9) are too large to display true inertial range behavior. Using DNS, Biferale et al. [62] quote shape factors in the inertial range as $I_1 = 0.82$, $I_2 = 0.16$ and $I_3 = 0.02$, which are however derived from exit time statistics (Chapter V) and cannot be compared with mean shape factors at fixed time directly. However, Biferale et al. [62] also estimated the mean shape factors from PDFs that have been conditionally sampled to remove tetrads with any one of the eigenvalues outside specified scaling ranges. The values obtained using this latter approach, $\langle I_1 \rangle = 0.854$, $\langle I_2 \rangle = 0.135$ and $\langle I_3 \rangle = 0.011$ are similar to the ones in Figure 4.9 and Table 4.3.

The evolution of the probability distributions of the shape factors I_1, I_2 and I_3 with time are shown in Figure 4.10 for tetrads of initial size $r_0/\eta = 1/4$ from the simulation at $R_\lambda \approx 1000$. In principle, because of Equation 4.8 and the constraint $I_1 + I_2 + I_3 = 1$, if Λ and any one of I_1, I_2 and I_3 are given then the other two can be determined as the solution of a quadratic equation, but since the relationship is nonlinear it does not carry over to the moments. Similar to Figure 4.8, the PDFs shown are taken at times where (based on Figure 4.9) $\langle I_2 \rangle$ (i) crosses its diffusive range value, (ii) attains its minimum, and (iii) reaches its inertial-range inflection point, and are compared with the asymptotic diffusive limit (computed from Monte-Carlo calculations) as well. The PDFs of I_1 and I_2 appear to have complementary shapes, while that of I_3 is dominated by very small values of I_3 and has a positively skewed tail. The PDF of I_2, which peaks at $I_2 \approx 0.05$ in the inertial regime, is qualitatively similar results from the simulations of Biferale *et al.* [62], while the PDF of I_3 (sharply peaked at $I_3 = 0$ beyond the ballistic regime) resembles results of Xu *et al.* [63].

For all three shape parameters there is good agreement between the PDF at the first

time instant shown and the diffusive limit, although the agreement is not as close as seen previously for the PDF of Λ in Figure 4.8. The diffusive limit is characterized by rounded shapes for the PDFs of I_1 and I_3 with small negative and positive skewness respectively. At the time of minimum $\langle I_2 \rangle$ the PDFs are sharply peaked and hence have been truncated before $I_2 = 0$ in the figures. The inertial range forms are significantly skewed as well.

The observed invariance of moments and PDFs of the shape factors over time periods considered to constitute the inertial regime makes time averaging over these periods a viable way to improve statistical sampling. Joint statistics benefit from this improvement and are a more refined way to determine the statistical geometry of tetrads in the inertial subrange. Inertial-range behavior is represented by data for initial size $r_0/\eta = 16$ from the simulation at $R_\lambda \approx 1000$. The joint PDF of I_1 and I_2, which correspond to the largest principal dimensions of the tetrad, is shown in this observed inertial subrange in Figure 4.11. The data are presented as contour lines where adjacent contour levels change by powers of two, with solid and dashed lines for inertial and diffusive ranges, respectively. This joint PDF in the diffusive limit when $t \gg T_L$ is obtained from Monte-Carlo calculations. All contour lines, as well as all samples, fall into a triangular realizability envelope bounded by three straight lines, representing limiting shapes of pancakes ($I_1 = I_2 > I_3$), sheets ($I_1 + I_2 = 1$; $I_3 = 0$), and needles ($I_1 > I_2 = I_3$). Since it has been seen earlier (Figure 4.9) that in the inertial range the mean value of I_1 becomes large as the mean of I_2 becomes small while their sum is almost unity, we expect that sheet-like structures (with very small I_3) close to the line $I_1 = 1 - I_2$ are favored. Accordingly, the solid contour lines in this figure are packed near the $I_1 = 1 - I_2$ boundary of the realizability envelope. Conversely, in the long-time diffusive limit the contour lines (dashed) become shifted towards both pencil and pancake-like shapes. At the same time, even the lowest contour levels drawn remain some distance away from the intersection point between pancake and needle shapes, which represents the limiting case of a regular tetrahedron with all edges equal in length.

Figure 4.12 shows the joint PDF of I_2 and I_3 in the inertial subrange, which compliments $P(I_1, I_2)$ in Figure 4.11. Here the realizability triangle is such that contour lines are naturally spaced further apart within a larger area of the figure. Again it can be seen that

in the inertial range (because of stronger deformation) contour lines show much greater tendency for sheet-like structures than geometries similar to a regular tetrahedron. Pencils or needles (near the left edge of the realizability triangle) are also somewhat more likely than pancake-shaped geometries (on the right). These trends are gradually relaxed and eventually reversed at large times, while regular tetrahedra (which also correspond to the largest possible Λ, close to 0.16) remain very unlikely. Thus, the regular tetrahedra almost never appear in isotropic turbulence at intermediate or large times.

4.3 Features of triangle shape

Although the fullest description of the geometric features of Lagrangian relative dispersion in three-dimensional homogeneous turbulence requires configurations of at least four particles, the shape of three-particle clusters is interesting for several reasons. The shape of triangles is much more amenable to mathematical description through the singular value decomposition (Equation 4.2) through the quantities w, representing aspect ratio, and χ, representing symmetry or orientation in the pseudo-space defined by the reduced separation vectors (Equation 4.1). The scheme we use to initialize particle positions readily provides triangles of two distinct initial shapes, which allows us to study the effect of initial cluster shape on the triangle statistics. A comparison of shape factors for triangles with those for tetrads is also relevant to general considerations on the limiting behavior of the shape factors as the number of particles in the cluster considered is made arbitrarily large. Finally, data on triangle shape statistics in two-dimensional (2D) turbulence [61] are available for comparison, with the caveat that such comparisons are inevitably indirect given the many inherent differences between 2D and 3D turbulence.

To begin, we show in Figure 4.13 the evolution of the mean aspect ratio parameter, $\langle w \rangle$, as a function of Batchelor-scaled time (t/t_0), for all initial sizes in the simulation at $R_\lambda \approx 1000$, and for triangles evolving from isosceles right-angled and equilateral initial shapes. The overall structure of ballistic, inertial and diffusive regimes as seen in this figure is very similar to those in Figures 4.5 and 4.9 for measures of tetrad shape (Λ, I_1, I_2, and I_3). It is also clear that the effect of initial shape is significant only at earlier times; for example,

the minimum values of $\langle w \rangle$ observed for the case of smallest initial size ($r_0/\eta = 1/4$) for the two initial initial shapes are almost the same (between 0.31–0.32).

Triangles of both isosceles right-angled and equilateral initial shapes show a clear inertial range scaling region where $\langle w \rangle$ is nearly constant for an extended period of time. This feature is apparently not observed in kinematic simulations [87] nor in experiments in 2D turbulence [61]. The height of the scaling range ($\langle w \rangle \approx 0.55$) is slightly lower than a plateau at height about 0.6 reported by Lüthi *et al.* [39] in an experiment at lower Reynolds number ($R_\lambda \approx 172$). Analogous plots for the shape factors give inertial range values of $\langle I_1 \rangle = 0.885$ and $\langle I_2 \rangle = 0.115$ (see Table 4.3), again independent of the initial triangle shape. It is noteworthy that these limiting values are larger and smaller respectively than their counterparts for tetrads, as listed in Table 4.3. It is possible that, as the number of particles in a particle cluster and the number of degrees of freedom increase, samples of I_1 (as the largest normalized principal dimension of the cluster) close to the maximum (unity) become less likely, thus contributing to a reduction of $\langle I_1 \rangle$ from triangles to tetrads. Similar plots at other Reynolds numbers also indicate these inertial range values show very little variation with R_λ in the range 390 – 1000. In the late-time diffusive limit in 3D we expect $\langle w \rangle = 2/3$, which follows directly from $P(w) = 2w$, which in turn can be derived from the diffusive PDF of I_2 as given by Pumir *et al.* [45]. Our data show a trend towards this limit.

In Figure 4.14, we show, under the same conditions as in Figure 4.13, the evolution of $\langle \chi \rangle$, which provides information about triangle symmetry, i.e. the resemblance of triangles to an isosceles triangle. The observed trends in $\langle \chi \rangle$ for initially isosceles right-angled triangles are similar to those in other shape parameters like $\langle I_2 \rangle$ and $\langle w \rangle$, with clear inertial range scaling at $\langle \chi \rangle \approx 0.452\ \pi/6$. However, it is apparent (e.g., by comparison with Figure 4.14) that the decrease of $\langle \chi \rangle$ in the dissipation range is not as strong as it is for $\langle w \rangle$ and $\langle I_2 \rangle$. Unlike the case in kinematic simulations [87] the minimum value of $\langle \chi \rangle$ appears insensitive to r_0/η. In addition, we find that for very small initial separations $r_0/\eta \leqslant 1$ an inflection point (almost a plateau for $r_0/\eta = 1/4$) appears at $\langle \chi \rangle \approx \pi/12$. This feature can be better understood after considering results for initially equilateral triangles, as below.

Triangles of equilateral initial shape do not possess a well-posed initial value of χ. As the

particles in such a triangle move away from their initial locations they do not develop any tendency to become more or less isosceles because the initial velocity vectors are isotropic. As a result, all values of χ are equally likely at early times, and the resulting uniform distribution has the mean value $\langle\chi\rangle = \pi/12$. This behavior is clearly seen in the right panel of Figure 4.14, up to $t/t_0 \approx 1$. Later, for $t > t_0$, $\langle\chi\rangle$ shows trends similar to those of other shape factors, with an inertial range plateau, dissipation range minima for small values of r_0/η, and, ultimately, an approach to a diffusive range with $\langle\chi\rangle = \pi/12$ at sufficiently large time. Comparison between the two halves of Figure 4.14 indicates triangles of both initial shapes show the same inertial range value and subsequent late time behavior. The time at which curves for triangles of different initial shapes start to behave in the same way is also close to the time at which data for small r_0/η shows an inflection point, as noted above.

We can now interpret the inflection point (for $r_0/\eta = 1/4$ and 1 in the left panel of Figure 4.14) as follows. For $r_0/\eta < O(1)$, the ballistic regime lasts for $O(t_\eta)$. During this time, the displacements tend to generate a uniform distribution for χ, as we have already noted. For initially isosceles right-angled triangles this uniform distribution will only be observed if r_0 is small enough so that the ballistic displacements wipe out shape information in the initial configuration before $t \approx t_\eta$. The resulting fast approach to a state with $\langle\chi\rangle = \pi/12$ is manifested as an inflection point in the curve. Subsequently, again for r_0 suitably small, there will be an exponential growth regime for a period $t \approx \ln(\eta/r_0)t_\eta$ (which can be arbitrarily long if r_0 is suitably small), during which the dynamics of local velocity gradients generates extremely distorted triangles at the minimum in $\langle\chi\rangle$. In the limit $r_0/\eta \to 0$, we expect that these triangles will be collinear, with $w = 0$ and $\chi = 0$, although as we have noted the rate of decrease of $\langle\chi\rangle$ with decreasing r_0/η is much slower than that of $\langle w\rangle$. This corresponds to one particle in the triangle moving far away from the other two. The other possibility (with $\chi = \pi/6$) requires two particles to move co-linearly far away from the third, which seems very unlikely. For $r_0/\eta > O(1)$, since the ballistic displacements cannot eliminate the initial shape information before the triangle enters the exponential growth regime, no early approach to a state with $\langle\chi\rangle = \pi/12$ occurs.

In Figure 4.15 we show the PDF of w at several time instants for initially isosceles

right-angled triangles of initial size $r_0/\eta = 16$ in the simulation at $R_\lambda \approx 1000$. The general trend in time is similar to that noted for Λ for tetrads in §4.2.2. At small time $t \ll t_0$ this PDF spreads away from a delta-function at $w_0 = \sqrt{3}/2 \approx 0.866$, then shifts towards smaller values of w, collapsing to an invariant form in the inertial range, which (according to Figure 4.13) spans the period 2.6 to 36.2 t_0.

The PDF of w for initially equilateral triangles (not shown) has almost the same behavior, except at very early times (as it evolves from a delta function at $w = 1$). This is expected, since, as discussed earlier, beyond an initial ballistic period, of order t_0, the initial shape has no further effect. For times t/t_0 representing the inertial range this PDF has a well-rounded peak close to 0.5, and a sharper drop on the left ($w \to 0$) than on the right ($w \to 1$). This implies that close-to-equilateral shapes are much more likely than the collinear case of three particles on a straight line. Eventually, at later times the shape of the PDF evolves towards the linear large-time asymptote $P(w) = 2w$. It may be noted that in 2D turbulence [61] the PDF of w takes an entirely different form, with a peak at $w = 0$. Furthermore, in the diffusive limit in 2D turbulence, w is uniformly distributed between 0 and 1, with mean value 0.5, showing that simple geometric factors are at least partly responsible for the differences between 2D and 3D turbulence.

Figure 4.16 shows the corresponding data on the PDF of χ, with results for triangles of the two different initial shapes shown separately. For initially isosceles right-angled triangles the PDF of χ shows the same trends as those discussed already for w and Λ for tetrads. In contrast, the PDF of χ for initially equilateral triangles remains uniform in the ballistic range until $t = t_0$, as noted in the discussion following Figure 4.14. Subsequently, this PDF evolves through an invariant inertial range form before the trend reverses back towards the uniform diffusive form. The inertial range form of $P(\chi)$ is characterized by a smooth decrease with χ throughout, with sensitivity to χ being weak for χ close to $\pi/6$. Like the case of w, the shape of this PDF is also very different from that in 2D turbulence [61]. Although in the diffusive limit the particle displacements are Gaussian distributed, this is not a prerequisite for a uniform distribution of χ. Indeed, we have identified two physical

causes, namely isotropic perturbation away from an undefined initial state, as well as late-time independent motion, which can lead to a lack of preference for any value of χ in the simulated turbulent flow. Consequently, it is not surprising that the PDF of χ varies much less in time than that of w.

For a more detailed characterization of the distribution of triangle shapes, we show the joint PDF of χ and w under the observed inertial range conditions (the same ones used in Figure 4.11) in Figure 4.17. There is a ridge of elevated probability density running from $\{\chi = 0, w \approx 0.3\}$ to $\{\chi = \pi/6, w \approx 0.8\}$. The most probable shape is at the lower end of this ridge, i.e. at $\chi = 0$, representing isosceles shapes with two long sides and one short side. The other end of the ridge where $\chi = \pi/6$ corresponds to triangles with two equal sides not much shorter than the third. Finally, the placement of contour lines also suggests sensitivity to χ is strong near $w = 0$ but weak near $w = 1$.

Additional information on the interdependence between w and χ is available in the conditional PDFs, say of w given χ, which are shown together with the unconditional PDF of w in Figure 4.18, under the same conditions as in Figure 4.17. It can be seen that, compared with the unconditional PDF, small values of χ lead to increased incidence of small w. Recalling (from Sec. II) that small χ represents isosceles triangles of two long sides and one short side, this can be understood as the case of one particle moving far away from the other two which in turn are still close together, such that the area, and hence w, is small. On the other hand, again relative to the unconditional PDF, large χ is associated with increased incidence of large w, representing isosceles triangles of one side slightly longer than the other two, and thus close to equilateral. A combination of large χ and small w would resemble the case of three particles aligned on a straight line with one particle exactly halfway between the other two. The fact that $P(w|\chi)$ is small at small w if χ is large confirms that such a scenario is one of low probability.

4.4 Summary

Measures of size and measures of shape are considered separately for clusters of three and four particles; shape statistics generally show better-defined scaling properties. Tetrad

shape is represented by the parameter $\Lambda = V^{2/3}/R^2$ as well as shape factors defined as normalized eigenvalues (I_1, I_2, I_3, in descending order) of the dispersion tensor. All of these parameters indicate the distribution of shape evolves from the ballistic range (where all tetrads have the same shape) to an asymptotic diffusive range, through an intermediate stage where some tetrads become highly elongated. Provided the Reynolds number is sufficiently high, this intermediate time period can be identified with inertial range scaling, in which a plot of the mean shape parameters versus time shows, depending on the initial tetrad size, either a flat scaling range or an incipient inflection point at the same height. From the data we infer that the inertial range values of $\langle\Lambda\rangle$, $\langle I_1\rangle$, $\langle I_2\rangle$ and $\langle I_3\rangle$ are 0.045, 0.83, 0.16, and 0.01 respectively. Joint probability density functions of these shape parameters also indicate that highly stretched shapes, which tend to be sheet like ($I_1 + I_2 = 1$, $I_3 = 0$), are dominant in the inertial range period, while shapes resembling pancakes ($I_1 = I_2$) and needles ($I_2 = I_3$) are more prevalent at later times. We have compared our results on shape parameters with available data from experiments and other numerical simulations, and observed a satisfactory degree of qualitative agreement although there are differences in flow conditions and sampling.

While a complete description of tetrad shape requires three independent parameters, the shape information for triangles of three particles has fewer degrees of freedom and is more readily amenable to a detailed analysis. In addition to the shape factors I_1 and $I_2 = 1-I_1$, or equivalently the aspect ratio parameter w (Equation 4.9), we also studied the pseudospace rotation χ (Equation 4.10), which quantifies the symmetry of the triangle in terms of its deviation from an isosceles shape. We find that invariance in the statistics of triangle shape parameters occurs for widely disparate initial shapes, and both initially equilateral and initially isosceles right-angled triangles approach $\langle w\rangle \approx 0.55$ and $\langle\chi\rangle = 0.45(\pi)/6 \approx 0.24$ in the inertial range. Corresponding values for the mean shape factors are $\langle I_1\rangle = 0.89$ and $\langle I_2\rangle = 0.11$. Finally, an examination of joint and conditional probability density functions shows the prevalence of approximately isosceles triangles of two long sides and one short side, which is understood as the case of one particle moving away from the other two which are still close together.

An overall observation in this work is that inertial range scaling is more readily observed in the statistics of measures of cluster shape (e.g. Figure 4.5) than those of measures of cluster size (e.g. Figure 3.11). This suggests that measures of shape representing the statistical geometry of turbulence are more robust and perhaps more amenable to modeling or theoretical description than measures of size, which are more dependent on a degree of separation available within the range of turbulence scales acting on a given cluster. At the same time, we have also encountered some interesting features which are not fully explained. One example is that, for small initial sizes, the diffusive form of the PDF of tetrad shape parameters such as Λ appear to be attained prematurely when $\langle\Lambda\rangle$ first encounters (transiently) the value that represents the diffusive limit. Another example is the uniform distribution of χ for triangles, which occurs during the ballistic distortion of initially equilateral triangles in isotropic turbulence, in addition to its more readily understood association with independent particle motion. Since, it is recognized, of course, that changes in size and shape both have an important role in the physics of multiparticle cluster dispersion, it is likely that conditional sampling based on cluster size would be helpful for understanding these features better. In addition, to put differences between triangles and tetrads in perspective, it would be useful to study clusters of more than four particles, through the dispersion tensor or through the use of Euler angles (such as χ) extended from triangles to tetrads.

It is evident that the problem of multiparticle cluster evolution is less studied and less understood than the case of two-particle relative dispersion, and the stochastic modeling in this context is likewise underdeveloped. Hopefully the present data would be useful for model development in the future.

Table 4.1: Initial shape parameters of the tetrad shown in Figure 3.1

R_0^2	V_0	Λ_0	$I_{1,0}$	$I_{2,0}$	$I_{3,0}$
$(9/4)r_0^2$	$r_0^3/6$	$6^{-2/3}(9/4)$	$4/9$	$4/9$	$1/9$

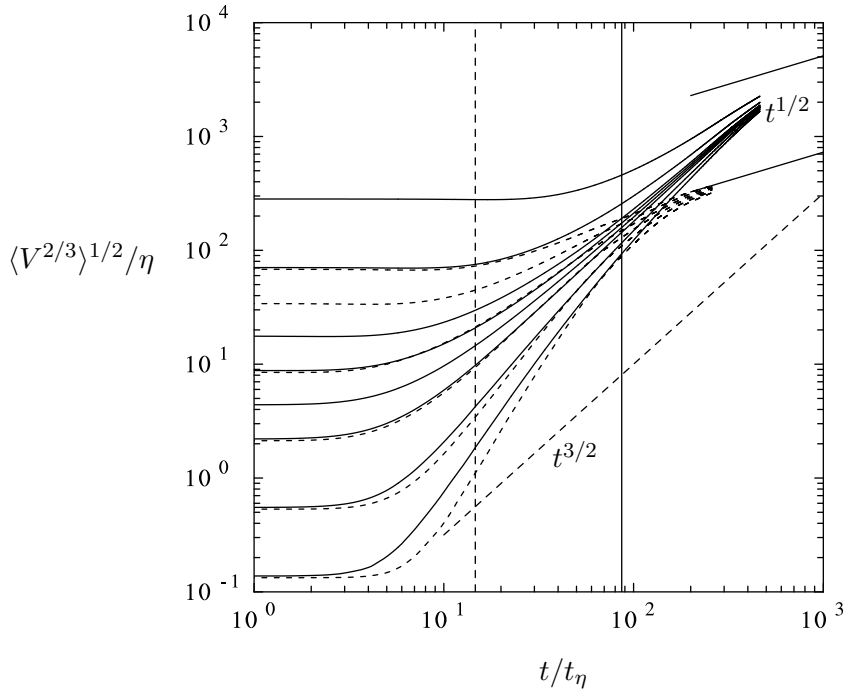

Figure 4.1: Evolution of linear tetrad size derived from the tetrad volume, in the form $\langle V^{2/3}\rangle^{1/2}$, normalized by Kolmogorov variables, at $R_\lambda \approx 140$ (dashed curves) and 1000 (solid curves). Curves at each Reynolds number are, going upward, for $r_0/\eta = 1/4, 1, 4, 16, 64, 128$ ($R_\lambda \approx 140$) and for $r_0/\eta = 1/4, 1, 4, 8, 16, 32, 128, 512$ ($R_\lambda \approx 1000$). Dashed line of slope 1.5 provides reference for inference of inertial range scaling. Solid lines at $t^{1/2}$ represent diffusive limit results ($\langle V^{2/3}\rangle^{1/2}/\eta \approx (1.16R_\lambda)^{1/2}/15^{1/4}(T_L/\tau_\eta)(t/\tau_\eta)$) for each Reynolds number. Vertical lines show ratio of T_L/t_η at $R_\lambda \approx 140$ (dashed) and 1000 (solid).

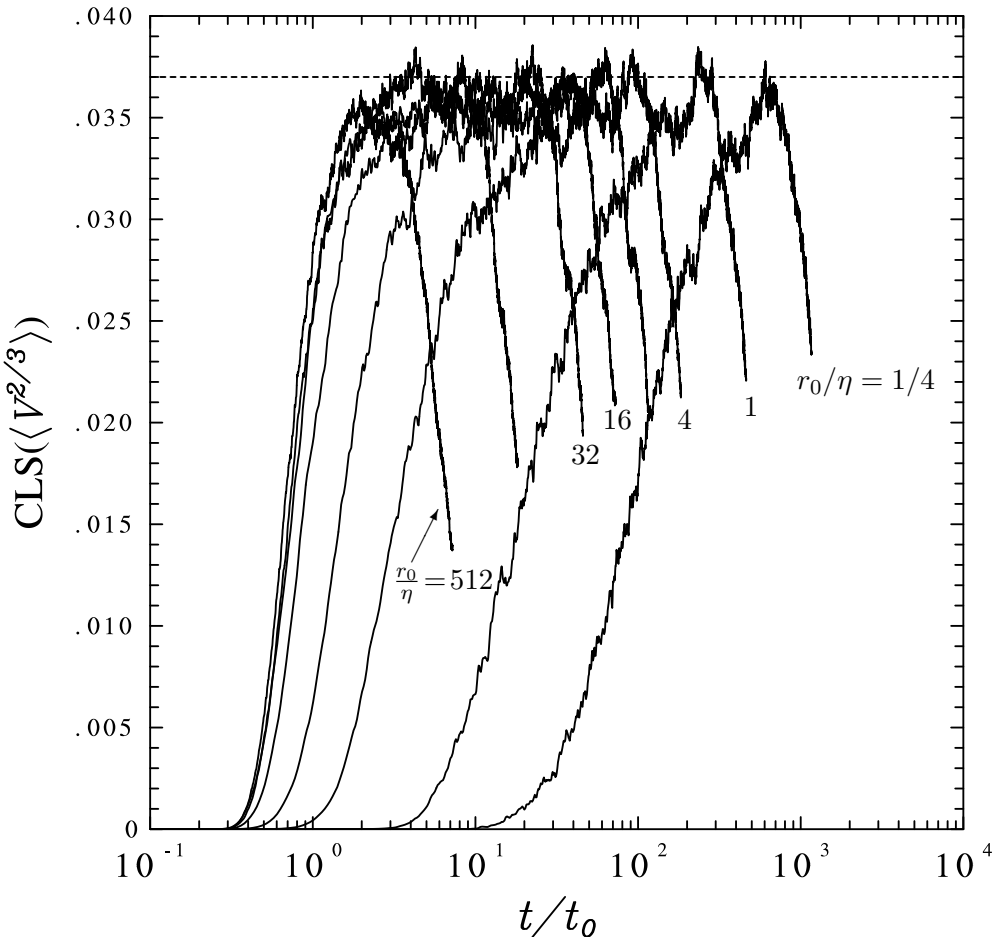

Figure 4.2: The cubed-local-slope of $\langle V^{2/3} \rangle$, $6^{-2/3} \left[d \left(\langle (V/V_0)^{2/3} \rangle^{1/3} \right) / d(t/t_0) \right]^{1/3}$, at $R_\lambda \approx 1000$ for $r_0/\eta = 1/4$, 1, 4, 8, 16, 32, 128 and 512. The factor of $6^{-2/3}$ is needed since t_0 is defined (Equation 3.8) using r_0 instead of V_0. Curves move to the left with increasing r_0/η. A horizontal dashed line is placed at the estimate of $C_{V^{2/3}} \approx 0.037$.

Table 4.2: Estimated values of inertial range scaling constants for tetrad volume and eigenvalues of the dispersion tensor. The sum of the scaling constants of the three eigenvalues is equal to 3/2 of Richardson's constant (g). These values are inferred from simulation data at R_λ 1000 as shown in Figs. 3.11 and 4.4.

$C_{V^{2/3}}$	$C_{g,1}$	$C_{g,2}$	$C_{g,3}$	$3g/2$
0.037	0.72	0.12	0.012	0.85

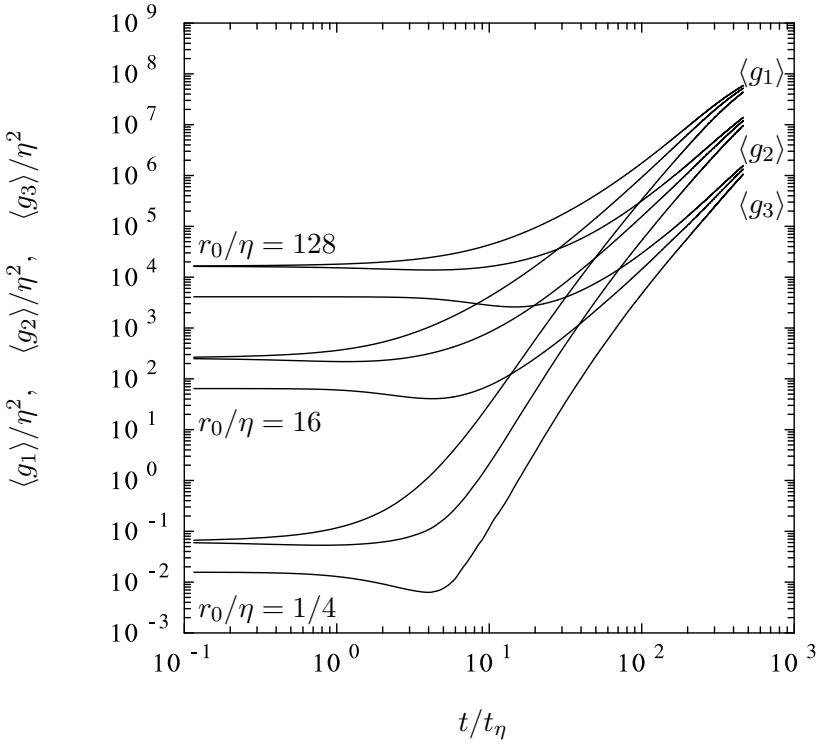

Figure 4.3: Evolution of mean tetrad eigenvalues in Kolmogorov variables, from the simulation at $R_\lambda \approx 1000$. Three sets of curves for $\langle g_1\rangle$, $\langle g_2\rangle$, $\langle g_3\rangle$ are shown, for tetrads with $r_0/\eta = 1/4$ (lower), 16 (middle), and 128 (upper). (Note that $g_1 \geqslant g_2 \geqslant g_3$ by definition.)

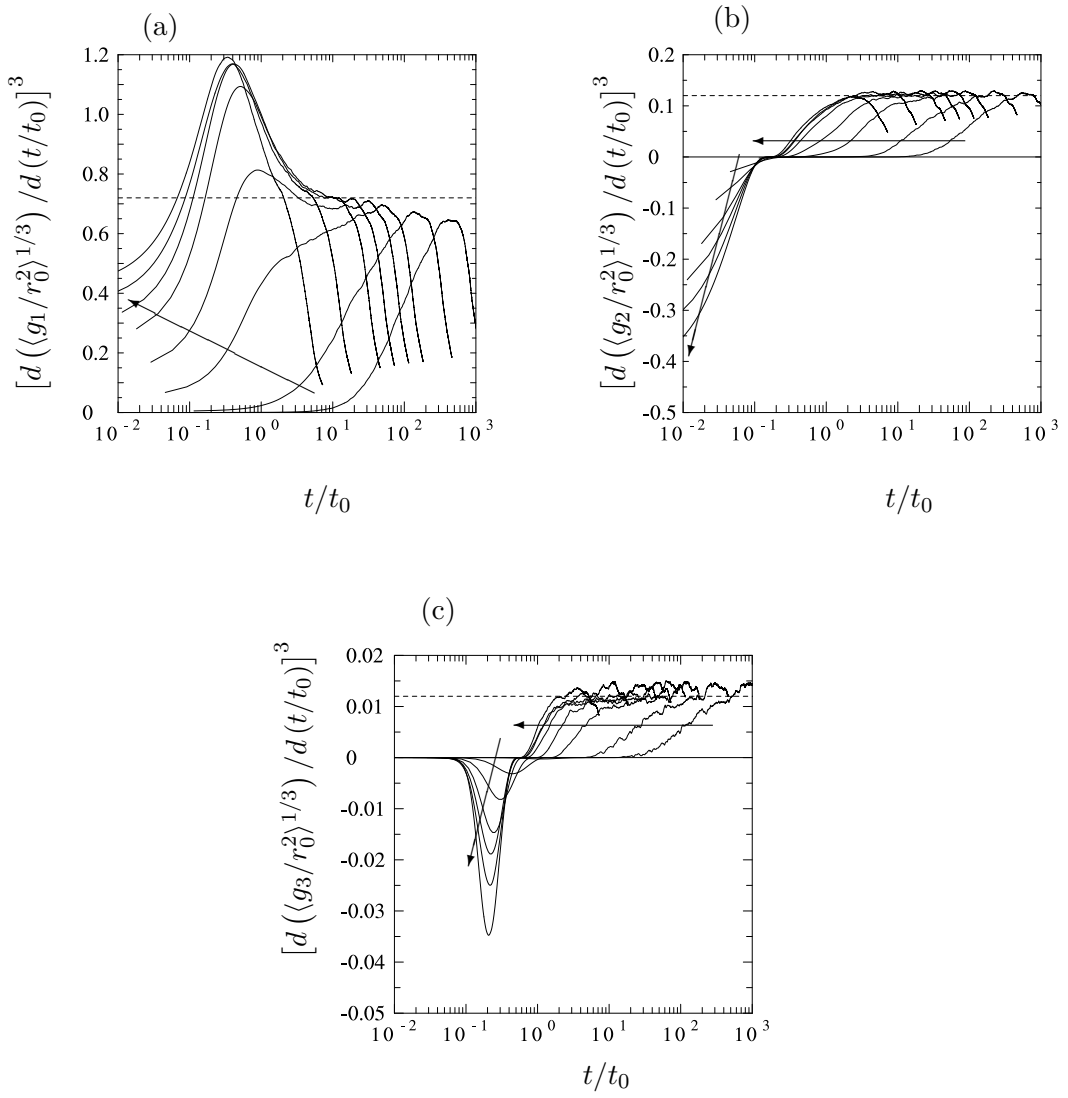

Figure 4.4: Cubed-local-slope plots for the tetrad moment-of-inertia eigenvalues: (a), $\langle g_1 \rangle$; (b), $\langle g_2 \rangle$; and (c), $\langle g_3 \rangle$; all normalized by r_0^2, from the simulation $R_\lambda \approx 1000$. Curves move to the left with increasing r_0/η. Dashed lines denote the estimates $C_{g,1} \approx 0.72$, $C_{g,2} \approx 0.12$, and $C_{g,3} \approx 0.012$. Arrows indicate increasing initial separation.

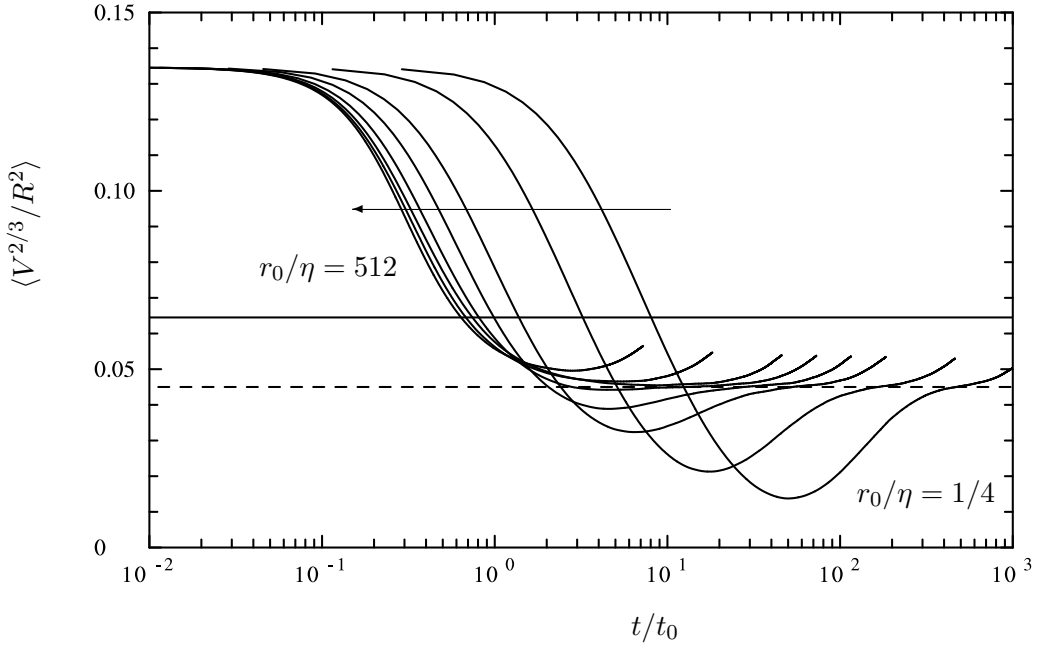

Figure 4.5: Mean value of $\Lambda = V^{2/3}/R^2$ as a function of Batchelor-scaled time, from the simulation at $R_\lambda \approx 1000$. Initial separations are, for curves terminating at the rightmost edge of the plot to the left, $r_0/\eta = 1/4$, 1, 4, 8, 16, 32, 128 and 512. Solid line marks large-time diffusive limit $\langle V^{2/3}/R^2 \rangle \approx 0.0645$, which is determined by Monte Carlo calculations. Dashed line marks observed inertial range value of $\langle V^{2/3}/R^2 \rangle \approx 0.045$. The arrow indicates increasing initial separation.

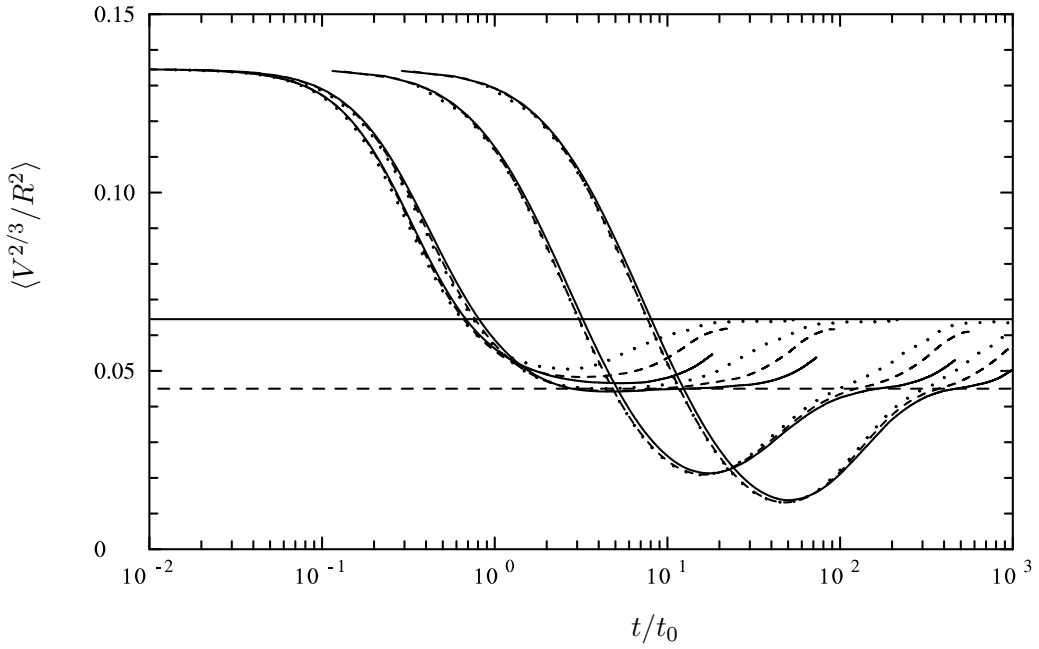

Figure 4.6: Mean value of $\Lambda = V^{2/3}/R^2$ as a function of Batchelor-scaled time at $R_\lambda \approx 390$ (dotted curves), 650 (dashed curves) and 1000 (solid curves). Initial separations are, for curves terminating at the rightmost edge of the plot to the left, $r_0/\eta = 1$, 4, 16, and 128 for all three Reynolds numbers. Solid and dashed lines at levels 0.0645 and 0.045 have the same meanings as in Figure 4.5.

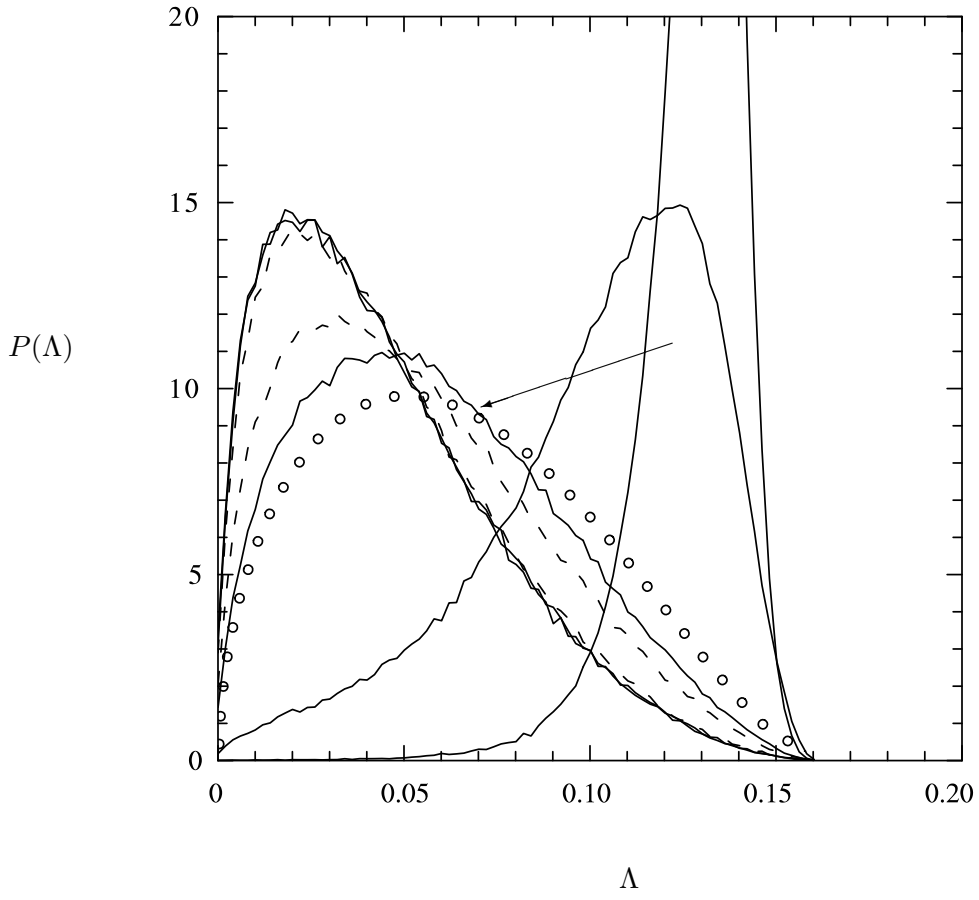

Figure 4.7: PDF of $\Lambda = V^{2/3}/R^2$ for tetrads of $r_0/\eta = 16$ at $R_\lambda \approx 1000$ computed at times $t/t_0 = 0.1$, 0.3, 1, 3, 10, 30 and the final time in the simulation ($t/t_0 = 72$). Dashed curves for times $t/t_0 \geqslant 30$ during approach to the diffusive limit (unconnected circles), which is determined by Monte Carlo calculations. Arrow indicates increasing time in the interval $0.1 \leqslant t/t_0 \leqslant 1$.

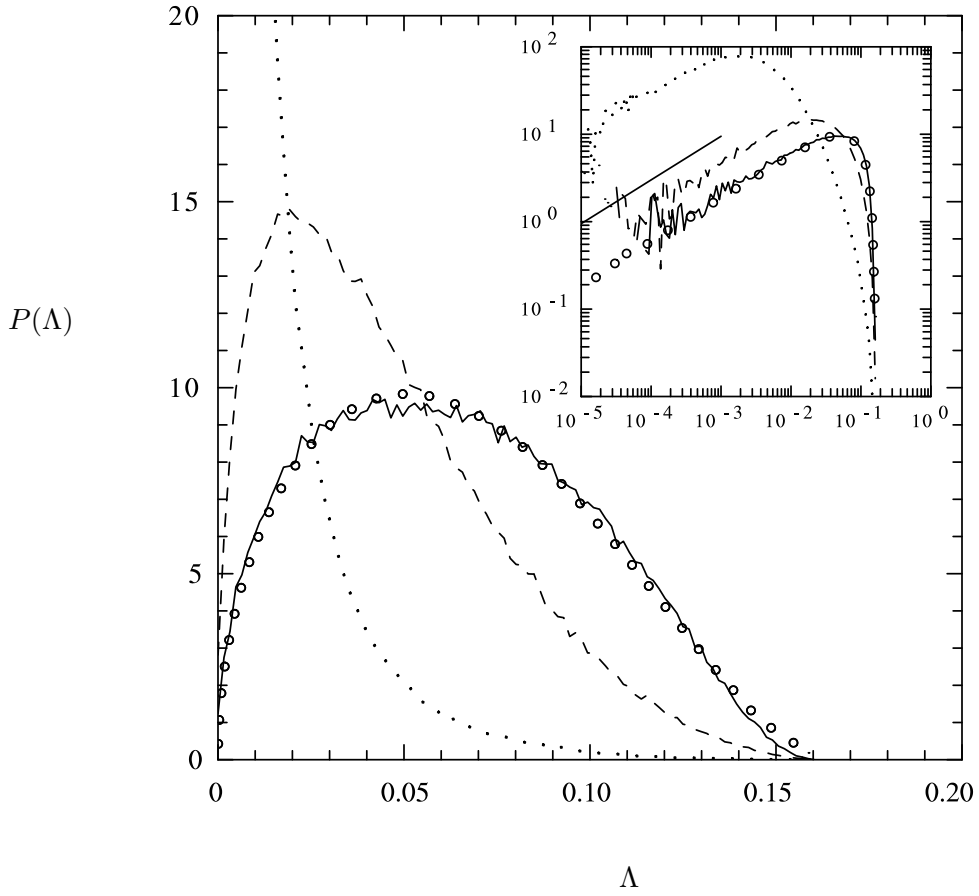

Figure 4.8: PDF of $\Lambda = V^{2/3}/R^2$ for tetrads of $r_0/\eta = 1/4$ in the simulation at $R_\lambda \approx 1000$, computed at times when $\langle\Lambda\rangle$ first crosses the diffusive value 0.0645 ($t/t_0 = 8$, solid curve), when $\langle\Lambda\rangle$ attains its minimum value of 0.0137 ($t/t_0 = 50$, dotted curve), and when $\langle\Lambda\rangle$ shows an inflection point at the inertial range value 0.045 ($t/t_0 = 471$, dashed curve). Unconnected circles have same meaning as in Figure 4.7. The inset shows the same data on logarithmic scales, with a solid line of slope 1/2 for reference.

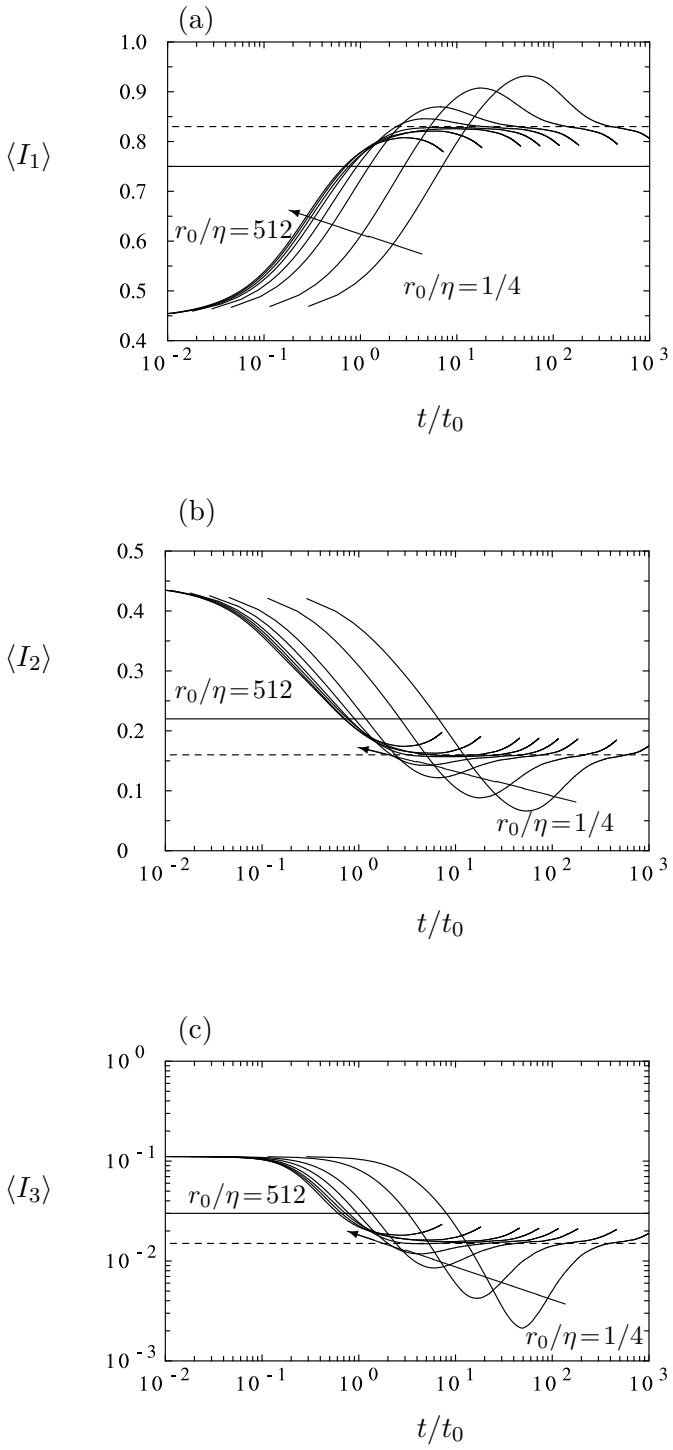

Figure 4.9: Mean tetrad shape factors as functions of Batchelor-scaled time in the simulation at $R_\lambda \approx 1000$. for $r_0/\eta = 1/4$, 1, 4, 8, 16, 32, 128 and 512: (a) $\langle I_1 \rangle$. (b) $\langle I_2 \rangle$. (c) $\langle I_3 \rangle$. Curves for smallest r_0 terminate at largest t/t_0. Horizontal solid and dashed lines denote diffusive and inertial range values respectively, as listed in Table 4.3. Arrows point towards increasing initial separation.

Table 4.3: Mean shape parameters in the inertial and diffusive regimes. Inertial range values are based on data from the simulation at $R_\lambda \approx 1000$. as seen in Figures 4.5 and 4.9 for tetrads, and Figure 4.13 and 4.14 for triangles. Diffusive range values are taken from Monte Carlo calculations where all position coordinates are normally-distributed.

	Tetrads				Triangles		
	$\langle V^{2/3}/R^2 \rangle$	$\langle I_1 \rangle$	$\langle I_2 \rangle$	$\langle I_3 \rangle$	$\langle I_2 \rangle$	$\langle w \rangle$	$6\langle \chi \rangle/\pi$
Inertial	0.045	0.825	0.16	0.015	0.12	0.55	0.45
Diffusive	0.065	0.75	0.22	0.03	0.16	2/3	1/2

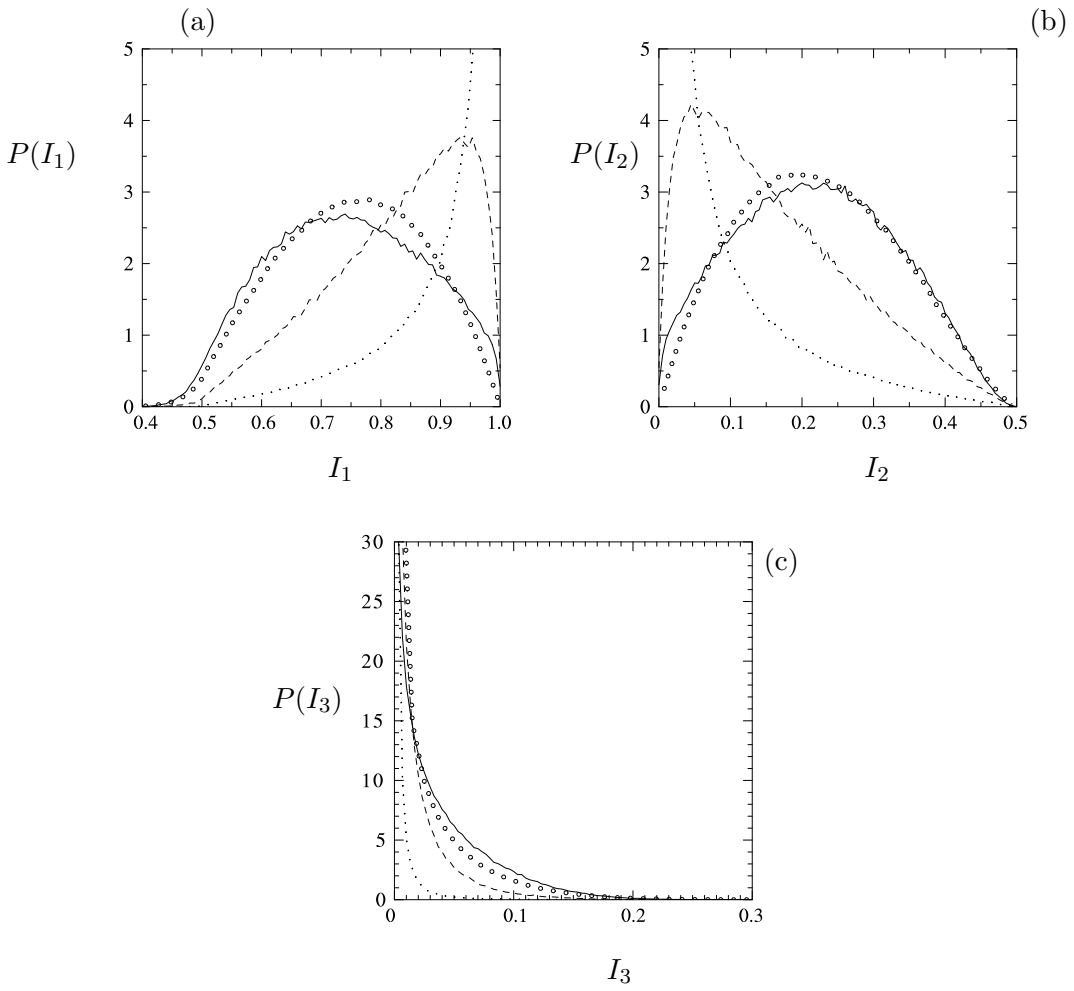

Figure 4.10: PDFs of tetrad shape factors (a) I_1, (b) I_2 and (c) I_3 for $r_0/\eta = 1/4$ in the simulation at $R_\lambda \approx 1000$, computed at times when $\langle I_2 \rangle$ first crosses its diffusive value ($t/t_0 = 6.7$, solid curve), when $\langle I_2 \rangle$ attains its minimum ($t/t_0 = 53$, dotted curve), and when $\langle I_2 \rangle$ reaches its inertial-range inflection point ($t/t_0 = 587$, dashed curve). The PDF in the diffusive limit is shown with unconnected circles for each shape factor.

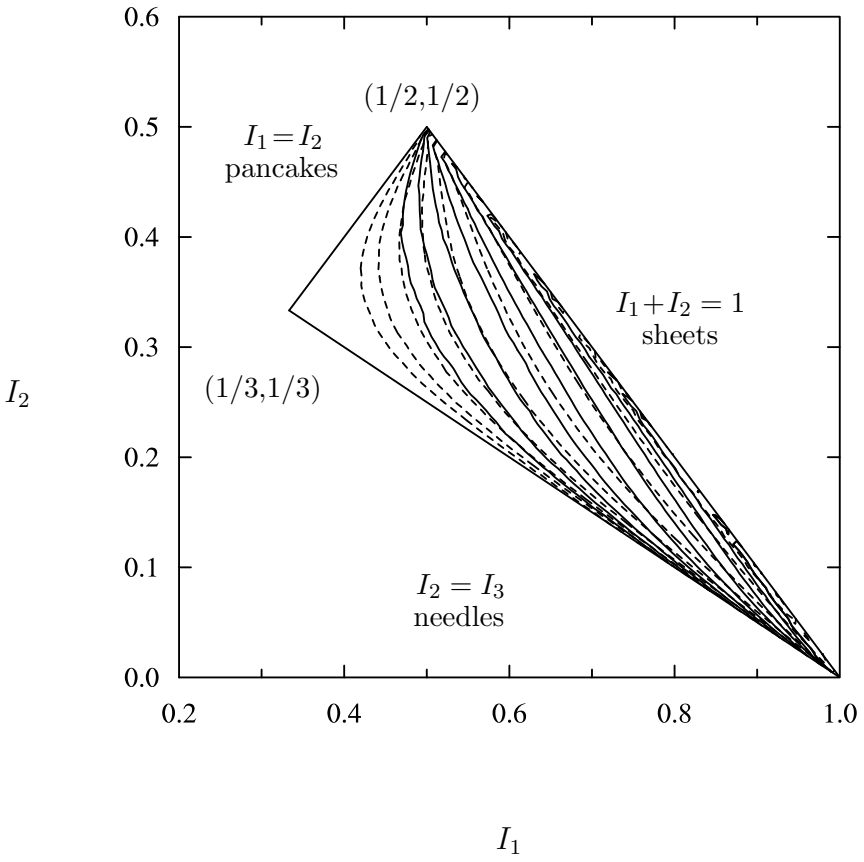

Figure 4.11: Contour plot of joint PDF of I_1 and I_2: solid curves for DNS data on tetrads of $r_0/\eta = 16$, averaged over inertial range times $2.6 \leqslant t/t_0 \leqslant 36.2$ in the simulation at $R_\lambda \approx 1000$; dashed curves for diffusive regime result obtained by Monte-Carlo calculations. Straight lines mark the realizability boundaries of $I_1 + I_2 = 1$, $I_1 = I_2$ and $I_1 > I_2 = I_3$. Contour levels are highest (maximum 128) near the line $I_1 + I_2 = 1$ and decrease in powers of 2 to $P(I_1, I_2) = 1/4$.

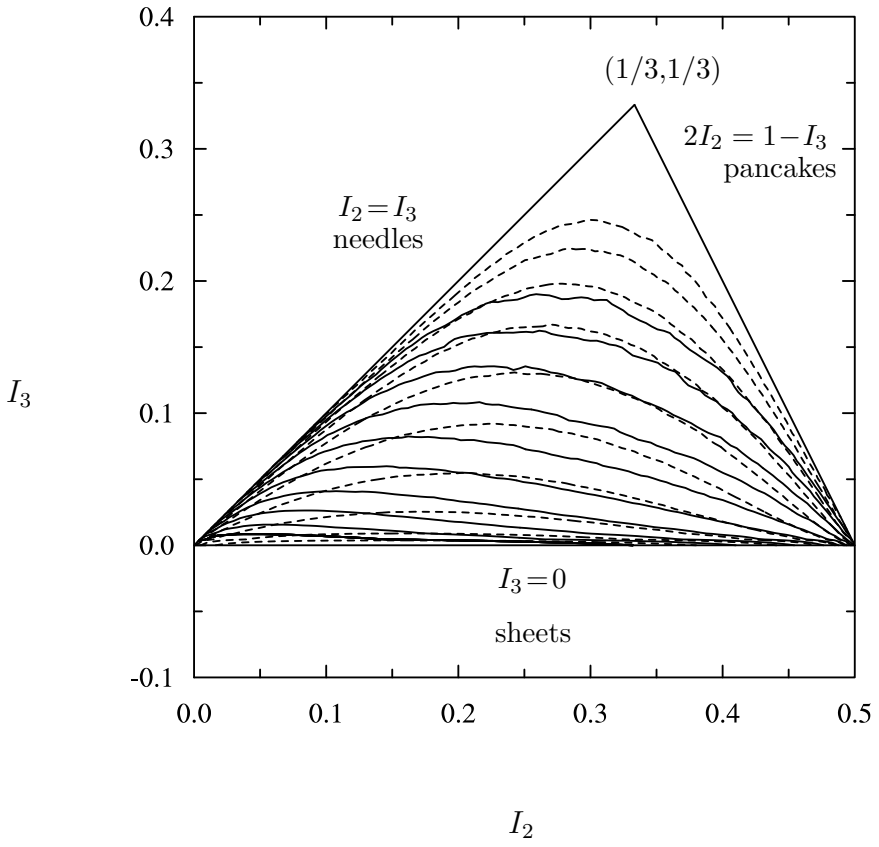

Figure 4.12: Joint PDF of I_2 and I_3 under the same conditions as Figure 4.11. Solid lines mark realizability boundaries of $I_2 = I_3$, $I_1 = I_2 > I_3$, and $I_3 = 0$. Contour levels are highest near the line $I_3 = 0$ and decrease successively in powers of 2.

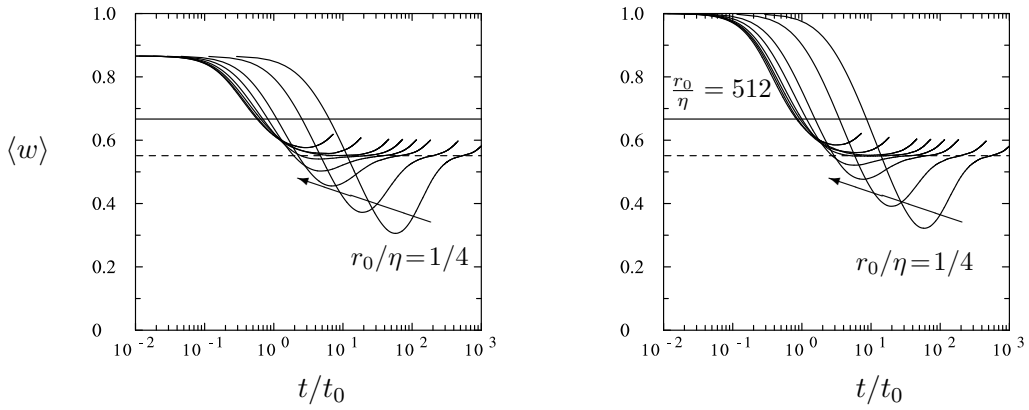

Figure 4.13: Evolution of $\langle w \rangle$ as a function of Batchelor-scaled time for $r_0/\eta = 1/4$, 1, 4, 8, 16, 32, 128 and 512, from the simulation at $R_\lambda \approx 1000$. (*left*) initially isosceles right-angled triangles; (*right*) initially equilateral triangles. Curves for smallest r_0 terminate at largest t/t_0. Solid line at 2/3 indicates asymptotic value in the diffusive limit $t \gg T_L$. Dashed line at 0.55 indicates observed inertial range value.

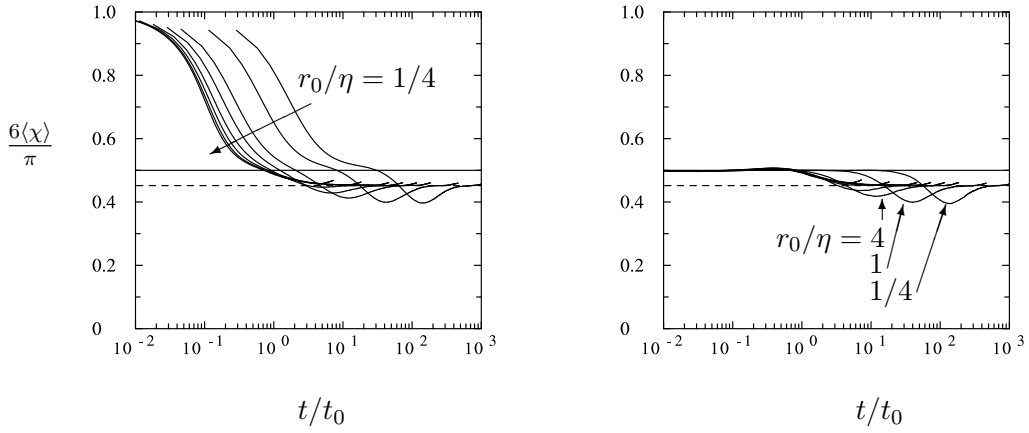

Figure 4.14: Evolution of $\langle\chi\rangle$ under the same conditions as in Figure 4.13, normalized by the maximum realizable value of $\pi/6$: (*left*) initially right-angled isosceles triangles. (*right*) initially equilateral triangles. Solid line is placed at $\langle\chi\rangle = \pi/12$ for asymptotic value in the diffusive limit, while dashed line at $\langle\chi\rangle = 0.45\pi/6 \approx 0.24$ indicates observed inertial range value. The arrow in the left plot indicates increasing initial separation.

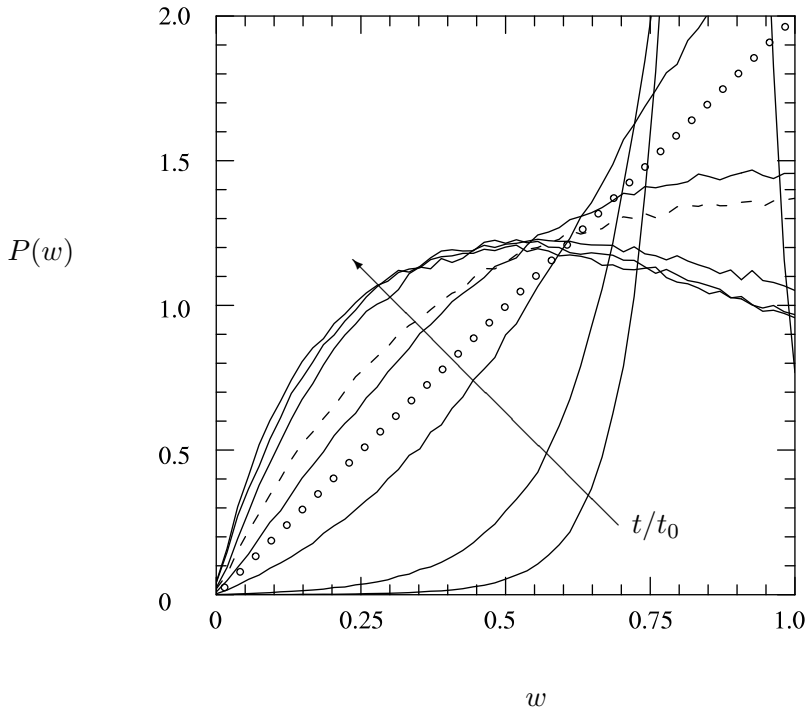

Figure 4.15: PDF of w for initially isosceles right-angled triangles of size $r_0/\eta = 16$, from the simulation at $R_\lambda \approx 1000$. The data are taken at times $t/t_0 = 0.1$, 0.2, 0.5, 1, 2, 5 and 10 (solid lines starting close to a delta function at $w_0 = \sqrt{3}/2$), and at the final simulation time, $t/t_0 = 72$ (represented by a dashed curve). The (linear) late-time asymptotic form of this PDF is shown as a line of unconnected circles. Arrow indicates increasing time in the interval $0.1 \leqslant t/t_0 \leqslant 10$.

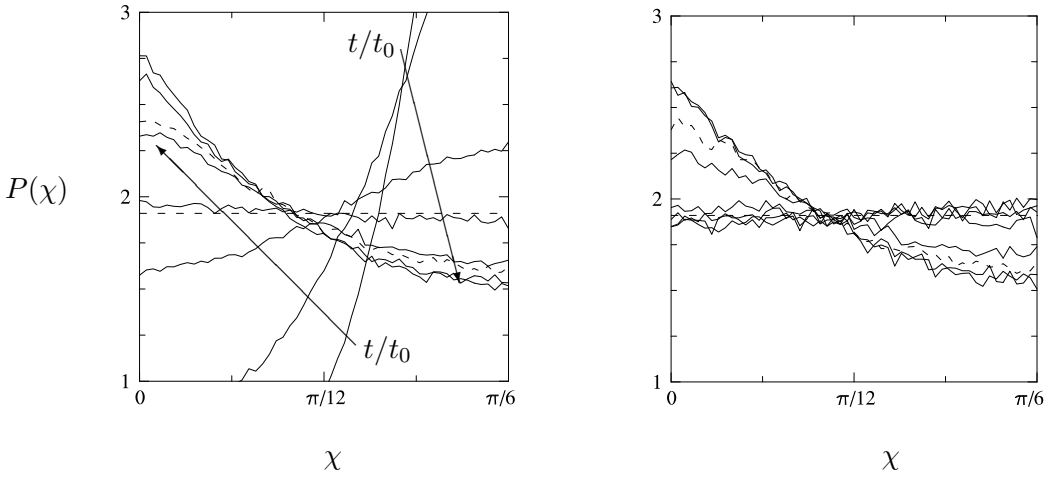

Figure 4.16: PDF of χ under the same conditions as in Figure 4.15, for initially isosceles right-angled triangles (*left*) and equilateral triangles (*right*). The late-time diffusive limit is shown as a dashed horizontal line (partly hidden) for comparison. Arrows indicate increasing time in the interval $0.1 \leqslant t/t_0 \leqslant 10$.

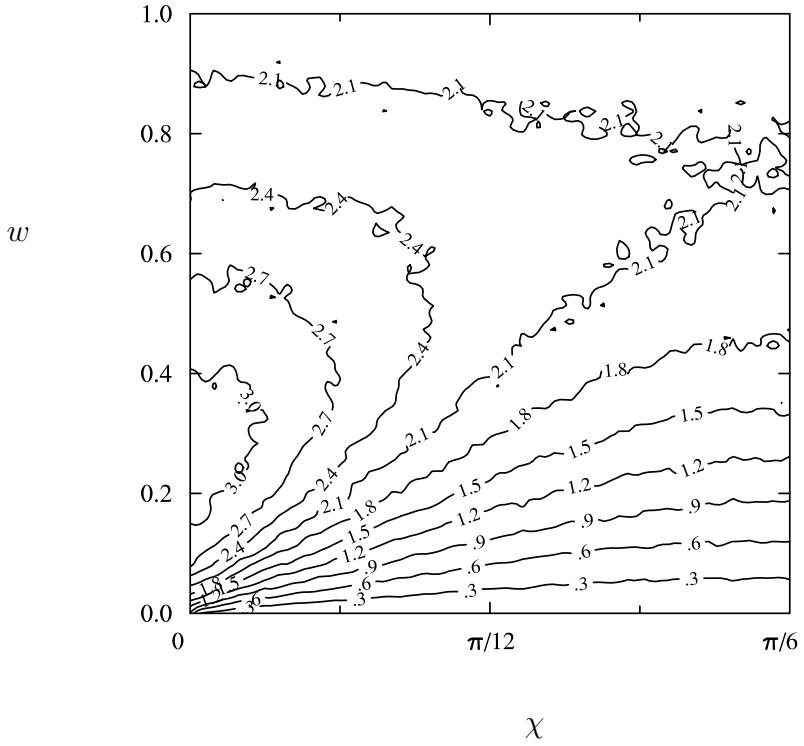

Figure 4.17: Contour plot of joint PDF of χ and w under inertial range conditions ($R_\lambda \approx 1000$, $r_0/\eta = 16$) for initially isosceles right-angled triangles. To improve the sampling, local time averaging from $t/t_0 = 2.2$ to 36.2 based on Figures 4.13–4.14 has been performed. The contour levels chosen are spaced linearly, from 0.3 to 3.0. Some sampling noise remains in lines at the highest contour levels.

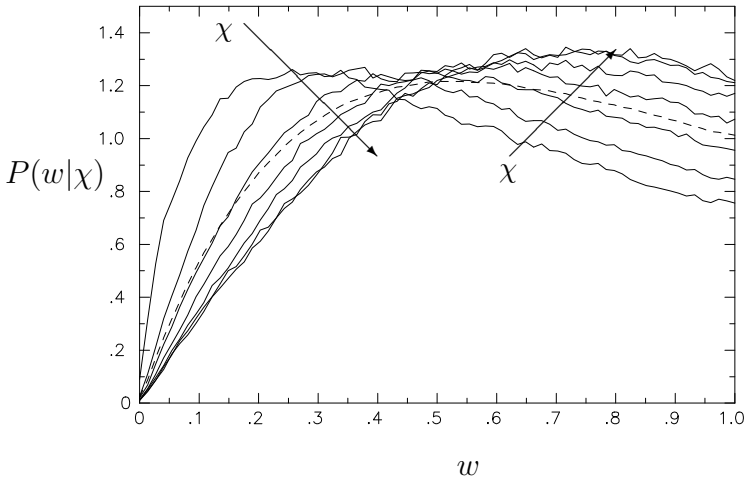

Figure 4.18: Conditional PDF, $P(w|\chi)$, corresponding to Figure 4.17, for $\chi \approx 0.0071$ to 0.517 in six uniform increments. The unconditional PDF is shown as a dashed curve for comparison. Arrows show direction of increasing value of χ.

CHAPTER V

EXIT TIMES

The preceding analyses of relative dispersion in Chapters 3 and 4 involved the time dependence of moments and distributions of parameters of cluster size and shape. Long transitional regimes between scaling regimes at asymptotically early and late time have motivated the study of the dynamics of dispersion at a fixed length scale instead of through instantaneous functions of time t. The observed overlap shared by, for example, the inertial and diffusive ranges can be attributed to a significant minority of rapidly-separating pairs of particles becoming uncorrelated with each other before $t \gg T_L$. Therefore, the long transition into the diffusive regime could be interpreted as the premature influence of the large scales (which control such rapidly-separating pairs earlier than the rest of the ensemble) at times that would otherwise be associated with the inertial subrange. Since the turbulent field at scales comparable to the separation distance have such a marked effect on pair dispersion (§3.2.1), it may be interesting to find some way of sampling pair separation statistics at fixed length scale.

The exit time $T_\rho(r)$ is the simplest quantity that may be computed at a fixed length scale and is defined to be the difference between the first time a particle pair's separation reaches r and the first time it reached r/ρ, where $\rho > 1$ is a prescribed parameter that determines the spacing between the fixed thresholds at which exit events are evaluated. Thus, the scales of motion driving dispersion are treated as independent variables while the time taken for particle pairs to cross these thresholds becomes a random variable. Exit times were introduced by [58] and have since grown into an alternate method of examining turbulent dispersion in two [59, 88] and three [56, 57] dimensions.

We briefly present the necessary mathematical background to use and study exit times in relative dispersion, including a brief discussion of the diffusion model introduced by Richardson [12] for the PDF of pair separation distance. The application of Kolmogorov's

1941 theory to moments of exit times introduces a hierarchy of scaling constants at fixed thresholds in the inertial subrange. The scaling constants for the first moment $\langle T_\rho \rangle$ and the inverse third moment $\langle T_\rho^{-3} \rangle$ are particularly interesting. The mean exit time $\langle T_\rho \rangle$ may be thought of as a time scale for particle pairs to be "trapped" within scales of motion $r_n/\rho \leqslant r \leqslant r_n$ assuming particle pairs approaching one another for extended periods of time are rare. Mean exit time is also important for model estimates of Richardson's constant g [57]. Inverse moments of exit time are dominated by rapidly separating particle pairs with small values of T_ρ and could show the effect of large extensive strain rates at scales r_n. Furthermore, $\langle T_\rho^{-3} \rangle$ has scaling under the Kolmogorov similarity hypotheses that is the fundamental intermittency-free counterpart to Equation 1.1[28, 89, 57, 60]. Determining universal scaling ranges in r_n for $\langle T_\rho^{-3} \rangle$ could quantify the connection between the range of Eulerian scales in r and their impact on inertial range scaling in relative dispersion statistics. An example would be to relate the width of the inertial subrange in Eulerian statistics to the pair separation distances r that may be considered to lie in the inertial subrange as well. The differences between g predicted from mean exit time and the results for g in §3.2.3 demonstrate the limitations of Richardson diffusion as a description of inertial subrange dispersion.

The results for $\langle T_\rho^{-3} \rangle$ in our simulations do not agree well with Kolmogorov predictions. To better compare our results to the existing literature on exit times in DNS, we compare an ensemble of pairs tracked using linear interpolation to an ensemble tracked using cubic spline interpolation (§2.2.1) in a highly resolved simulation at $R_\lambda \approx 235$. The chapter concludes with some possible approaches to improving the use of these new methods in DNS.

5.1 Definitions and theoretical predictions for exit times

5.1.1 Exit times and scaling constants

Exit times are successively computed for an ordered set of fixed thresholds $r_n = \rho^n r_0$, $n = 1, 2, \ldots$, so that $T_\rho(r_n)$ may be thought of as the time taken for a particle pair to first reach a separation of r_n (at $t_2(r_n)$) from the time it first reached a separation of r_{n-1} (at

$t_1(r_{n-1})$). Scaling laws for moments of exit time in the inertial subrange at high Reynolds numbers are consequences of Kolmogorov similarity theory and can be written as [60]

$$\langle T_\rho^p(r)\rangle = C_{r,p}\langle\varepsilon\rangle^{-p/3} r^{2p/3}, \quad \eta \ll r \ll L, \quad \eta \ll r/\rho \ll L \tag{5.1}$$

for any integer power p. The cases $p = 1$, which is simply the mean exit time, and $p = -3$, the third moment of inverse exit time, are most interesting. The case of $p = -3$ is interesting because it is dimensionally equivalent to the corresponding instantaneous result of Equation 1.1. Both scaling laws are linear in the dissipation rate and may be derived only from the Kolmogorov similarity hypotheses, making them immune to the effects of intermittency on Lagrangian statistics [28].

In principle, the PDF of exit time $p_E(T_\rho)$ may be determined by differentiating the probability that a given pair lies within a given threshold $[r/\rho, r]$ (see § 5.2.7 of Gardiner [90] for a general derivation and Boffetta & Sokolov [59] for the specific case of exit times in relative dispersion):

$$p_E(T_\rho) = -\frac{d}{dT_\rho}\int_{r/\rho}^{r} p(r', T_\rho)dr'. \tag{5.2}$$

5.1.2 Richardson diffusion

Richardson [12] first identified what is now understood to be the probability density function (PDF) of pair separation distance $p(r,t)$ and proposed a diffusion equation to model its evolution which may be written as

$$\frac{\partial p(r,t)}{\partial t} = \frac{1}{r^2}\frac{\partial}{\partial r}\left(r^2 K_p \frac{\partial p(r,t)}{\partial r}\right). \tag{5.3}$$

Richardson was particularly concerned about the form of the eddy diffusivity K_p in Equation 5.3 and proposed, based on a review of atmospheric measurements available at the time, that $K_p(r) \sim r^{4/3}$. This was the first recognition that pair separation distance (and thus cluster size) is increased most by the actions of eddies at the same scale of motion as r. Remarkably, Richardson's four-thirds law, as $K_p \sim r^{4/3}$ has come to be known, is also a possible consequence of Kolmogorov's similarity hypotheses. If K_p can only depend on mean dissipation rate $\langle\varepsilon\rangle$ and pair separation distance r, then

$$K_p(r) = k_0\langle\varepsilon\rangle^{1/3} r^{4/3} \tag{5.4}$$

for some dimensionless constant k_0 (see §24.4 of Monin & Yaglom [9]). The solution to Equation 5.3 with diffusivity given by Equation 5.4 under the initial conditions $p(r,0) = \delta(r)$ is

$$p(r,t) = \frac{\left[(3/2)^8/\Gamma(9/2)\right] r^2}{\left(k_0\langle\varepsilon\rangle^{1/3}t\right)^{9/2}} \exp\left(-\frac{9r^{2/3}}{4k_0\langle\varepsilon\rangle^{1/3}t}\right), \tag{5.5}$$

implying a PDF of pair separation with wide tails if the dispersion begins at sufficiently small scales [12, 9, 56]. Equation 5.5 may be multiplied by r^2 and integrated to obtain mean-square separation, recovering Equation 1.1 with

$$g = \frac{1144}{81}k_0^3. \tag{5.6}$$

The solution, Equation 5.5, to Richardson's diffusion equation, Equation 5.3, with K_p given by Equation 5.4, may be substituted into Equation 5.2, and, upon integration for the first moment of exit time, determines the proportionality constant for the coefficient $C_{r,1}$ appearing in Equation 5.1 for $p = 1$ to be [57]

$$C_{r,1} = \frac{\rho^{2/3} - 1}{2k_0\rho^{2/3}}. \tag{5.7}$$

Substituting Equation 5.7 into Equation 5.1 with $p = 1$ and combining with Equation 5.6 connects mean exit time to Richardson's constant under the assumptions of Richardson's four-thirds law:

$$g = \frac{143}{81}\frac{\left(\rho^{2/3} - 1\right)^3}{\rho^2}\frac{r^2}{\langle\varepsilon\rangle\langle T_\rho(r)\rangle^3}. \tag{5.8}$$

At large scales, independent particle motion means that relative dispersion is described by single-particle diffusion. The counterpart to Equation 3.14 may be derived for exit times at very large scales. Assuming a diffusion equation with constant diffusivity $K_p = 6u'^2T_L$ [90], mean exit time at large scales is

$$\langle T_\rho(r)\rangle = \frac{\rho^2 - 1}{18u'^2T_L}r^2, \quad r \gg L, \quad r/\rho \gg L\ . \tag{5.9}$$

Observation of $\langle T_\rho\rangle \sim r^2$ scaling requires $T_{\text{sim}} \gg T_L$ by an even greater margin than diffusive scaling for fixed-time statistics like Equation 3.14. The simulations at $R_\lambda \approx 140$, 235, 390 and the second simulation at $R_\lambda \approx 650$ (Table 3.1) are sufficiently long to show convincing diffusive scaling in $\langle T_\rho\rangle$. The other simulations do not have any thresholds at

$r_n \gg L$ reached by all pairs. Mean exit time computed at such thresholds is artificially reduced since only the faster particle pairs in the ensemble reach these thresholds before the end of the simulation.

The concept of diffusivity appears in more than one form in the study of relative dispersion, and it is important to keep the ramifications of diffusion in the inertial subrange distinct from its appearance at very large scales. When we speak of the "diffusive regime" when $t \gg T_L$, we refer to an asymptotic limit at large time in which the particles making up a cluster move independently from one another and independently of their initial configuration. Their dynamics on scales comparable to their separation distances approach the limiting case of a diffusion process with diffusivity determined by the r.m.s. velocity of the turbulence, which is a large-scale quantity [11]. Such asymptotic dynamics depend only on the homogeneity of the turbulence. However, any use of a diffusion equation like Equation 5.3 in the inertial subrange actually entails assuming that relative dispersion is well-approximated by a Markov process [60, 9] even when the positions and relative velocities of particles in a given cluster are still correlated with each other. This is usually regarded as a modeling assumption, and other forms for K_p besides the scale-dependent choice in Equation 5.4 have been proposed based on additional hypotheses about the dispersion process (notably by Batchelor [16]). Any choice of α in the power law $K_p \sim t^{3\alpha/2} r^{4/3-\alpha}$ produces a solution to Equation 5.3 whose moments recover the scaling law for mean-square separation in Equation 1.1, but is usually unlike Equation 5.5 [59]. However, the t^3 law in Equation 1.1 does not depend on any assumptions about the stochastic structure of the dispersion process; it may be obtained from the Kolmogorov similarity hypotheses alone.

Finally, we note our use of Equation 3.6 in Equations 5.1, and 5.8. When isolating $C_{r,p}$ in Equation 5.1,

$$C_{r,p} = \langle T_\rho^p(r) \rangle \langle \varepsilon \rangle^{p/3} r^{-2p/3}, \tag{5.10}$$

Equation 3.6 would be consistent with the following interpretation of the mean dissipation rate $\langle \varepsilon \rangle$:

$$\langle \varepsilon \rangle^{p/3} \langle T_\rho^p(r_n) \rangle = \left\langle \left(\int_{t_1(r_{n-1})}^{t_2(r_n)} \varepsilon(t')^{1/3} dt' \right)^p \right\rangle. \tag{5.11}$$

In Equation 5.11, the space-averaged dissipation rate ε is integrated in time during each exit event before these events are ensemble averaged. We use this procedure, which has little effect on the contributions of rapidly-separating particle pairs to exit times through closely-spaced thresholds, throughout this chapter in tests of Equation 5.10 and 5.8.

5.2 Analysis of moments of exit time

5.2.1 Mean exit time

In Figure 5.1, mean exit time from successive shells of radius $r_n = \rho^n r_0, n = 1, \ldots N_{\text{exit}}$, is shown at $R_\lambda \approx 390$ ($N_{\text{exit}} = 41$) and 650 ($N_{\text{exit}} = 51$) for all initial separations listed for each case in Table 3.1. In contrast with results like those shown for compensated mean-square pair separation $\langle r^2 \rangle$ at fixed time in Figure 3.2, initial separation has almost no effect on the values obtained except at the largest fixed scales. In the log scales used for Figure 5.1, a regime of inertial-range scaling (a dashed line at $\langle T_\rho \rangle \sim r^{2/3}$) seems to be shared by dispersion at both Reynolds numbers for all initial separations. Transition to independent motion begins at large scales ($r_n/\eta \approx 600$) at $R_\lambda \approx 390$, where mean exit time approaches r_n^2 scaling at the solid line drawn at the prediction of Equation 5.9 for this case. The simulation at $R_\lambda \approx 650$ was not run sufficiently long to begin approaching this limit as distinctly as the case at $R_\lambda \approx 390$. The fraction of the particle pairs that have crossed a given threshold at r_n is shown for these two cases in Figure 5.2. For the purposes of this discussion, $r_n/\eta \leqslant 900$ is considered to be fully converged for both cases.

The estimate of Richardson's constant g given in Equation 5.8 requires Richardson's PDF Equation 5.5 to hold during all exit events at inertial-range fixed scales. The utility of this description of relative dispersion has been the subject of extensive investigation and debate [60, 91]. In Figure 5.3 we plot the estimate of g given by Equation 5.8 for the cases shown in Figures 5.1 and 5.2 and find that the maximum value attained through this method is slightly lower than $g \approx 0.56$, which is more directly observed in the cube-root-slope of mean-square separation in Figure 3.5. The plateau in the computed values of Equation 5.8 at $R_\lambda \approx 390$ for $100 \leqslant r_n/\eta \leqslant 200$ in Figure 5.3 becomes a region in which this estimate of g increases with r_n until the onset of the diffusive regime at $r_n/\eta \approx 600$ at $R_\lambda \approx 390$ and

$r_n/\eta \approx 900$ at $R_\lambda \approx 650$. At this point, the estimate of g (itself a constant multiple of $C_{r,1}$ in Equation 5.10) decreases (provided all pairs have crossed all thresholds, which is not the case for $r_0/\eta > 1000$) since mean exit time begins to increase at a rate faster than $r_n^{2/3}$.

The other major result for Equation 5.8 is due to Biferale *et al.* [56] at $R_\lambda \approx 284$. Their evaluations (Figure 5 [56]) of Equation 5.8 produced an inflection point at $g \approx 0.5$ at $r_n/\eta \approx 100$. The results in Figure 5.3 at higher Reynolds number do not have the artificial increase in $C_{r,1}$ due to insufficient simulation time. Nevertheless, $g \approx 0.47$ can be inferred from Figure 5.3 at $r_n/\eta = 100$, but this is accompanied by some ambiguity that warrants further scrutiny.

5.2.2 Moments of inverse exit time

The appearance of a positive slope with respect to r_n/η at all initial separations smaller than $r_0/\eta = 512$ at $R_\lambda \approx 650$ in Figure 5.3 suggests a slight departure from the Kolmogorov similarity prediction of Equation 5.10. Such growth of the estimate of g with respect to r_n at $R_\lambda \approx 650$ in Figure 5.3 is a source of ambiguity in using mean exit time to infer Richardson's constant through the use of the Richardson diffusion equation (Equation 5.3). Based on the fully converged mean exit times in our DNS database, we do not know if the left-hand-side of Equation 5.8 will increase further with r_n at progressively higher R_λ or if it will plateau at some value of $g > 0.5$ and converge towards the values observed in the more conventional statistics of Chapter 3.

The scaling constant in Equation 5.10 for the inverse third moment of exit time $C_{r,-3}$ is a more direct analogy to Equation 1.1. Assessments of it would provide a baseline, free from the effects of intermittency, that would assist interpretation of the anomalous scaling in $C_{r,1}$ shown somewhat indirectly in Figure 5.3. However, direct tests of Kolmogorov scaling in the third moment of inverse exit time are even less robust than such tests for the mean exit time in Figures 5.1 and 5.3. In Figure 5.4 we show $C_{r,-3}$ at the same two Reynolds numbers, $R_\lambda \approx 390$ and 650, that were shown in Figures 5.1 and 5.3. No collapse with initial separation is observed at all but the largest scales, and only intermediate initial separations at $R_\lambda \approx 650$ show any sign of a plateau representing a constant value of $C_{r,-3}$ consistent

with the Kolmogorov 1941 similarity hypotheses. Due to the linearity of dissipation for $p = -3$ in Equation 5.10, this moment is not affected by intermittency [28, 57]. These results are markedly different from the plateau behavior for $C_{r,-3}$ obtained in the synthetic field of Boffetta *et al.* [89], the DNS of Biferale *et al.* [56], and the Lagrangian stochastic modeling of Sawford [60]. Some other mechanism must be responsible for the negative slope observed at r_n that are too small for independent particle motion.

Although exit times were originally proposed to remove the effects of disparate scales of motion on statistics of relative dispersion by changing the independent variable from time to a series of length scales, direct tests of Richardson-Obukhov scaling in $\langle r^2 \rangle$ (Figure 3.2) and $\langle T_\rho^{-3} \rangle$ (through $C_{r,-3}$ in Equation 5.1, shown in Figure 5.4) show dependence on initial separation and Reynolds number. To better understand this, we study the PDF of exit time $p_E(T_\rho)$. The PDF of mean-normalized exit time is shown in Figure 5.5 at $R_\lambda \approx 390$. The wide tails of this PDF at the initial separation shown in this plot, $r_0/\eta = 16$, is self-similar within the inertial range inferred from Figure 5.1. Similar behavior has been observed in other simulations at other Reynolds numbers [59, 56]. Boffetta & Sokolov [59] derived an expression for this tail by taking the long-time asymptotic limit of $p_E(T_\rho)$ obtained by substituting Equation 5.5 into Equation 5.2. In three-dimensional turbulence, this expression, presented by Biferale *et al.* [56], is

$$p_E(T_\rho) \sim \exp\left[-\kappa \frac{\rho^{2/3} - 1}{\rho^{2/3}} \frac{T_\rho}{\langle T_\rho(r) \rangle}\right], \quad T_\rho \gg \langle T_\rho(r) \rangle, \tag{5.12}$$

where $\kappa \approx 2.72$ is taken from the terms of an eigenfunction expansion[59] of $p_E(T_\rho)$ that dominate the slower exit events.

The PDF of exit time in Figure 5.5 shows that, although exit times do isolate the scales of motion acting on pairs of particles, "slowly-separating" pairs at the tails of the exit time PDF behave very differently from "fast" pairs at the core. The tails of this PDF approach the PDF (Equation 5.12) derived from Richardson diffusion (Equation 5.5), and the positive moments of exit time that are dominated by slowly separating pairs. But the "rapidly-separating" pairs dominate inverse moments of exit times and may cross closely spaced thresholds at low ρ in a "ballistic" fashion. Thus, direct tests of Equation 5.1 for

$p = -3$ are dominated by rapidly separating pairs that are fundamentally inconsistent with Richardson diffusion. This is associated with a much greater departure from Kolmogorov scaling given by Equation 5.1 in Figure 5.4 than is apparent in the results derived from mean exit times in Figures 5.1 and 5.3.

5.3 Linear interpolation

The simulations described here have inverse moments of exit time substantially different from those reported by Biferale *et al.* [56] even at comparable Reynolds numbers. Biferale *et al.* did report, for the smallest r_0/η in the inertial subrange, an inflection point in $C_{r,-3}$ that they interpreted (along with Boffetta & Sokolov [57]) as an incipient plateau for the emerging inertial subrange in $\langle T_\rho^{-3} \rangle$. Although many of these differences may be attributed to the shorter duration of the DNS of Biferale *et al.* , cubic spline interpolation for particle velocities may be capturing details in the trajectories of rapidly separating pairs that the choice of linear interpolation used by Biferale *et al.* does not resolve. Cubic spline interpolation is compared to linear interpolation to better understand these differences as they appear in statistics at fixed scale.

It is seen in Figure 5.6 that the interpolation algorithm has only a small effect on exit time statistics at the same grid resolution at the closest Reynolds number $R_\lambda \approx 235$, to the simulation presented by Biferale *et al.* [56]. There is no difference in the value of g inferred from mean exit time using Equation 5.8 in Figure 5.6(a) and negligible differences in computed values of $C_{r,-3}$ in Figure 5.6(b). We cannot attribute the departure from Equation 5.1 in our results at $p = -3$ to fortuitous plateaus in $C_{r,-3}$ brought about by linear interpolation of particle velocities. There are differences in small-scale quantities, but these do not accumulate appreciably in computations of exit time at inertial subrange scales.

The differences between spline and linear interpolation schemes are only apparent in those statistics most dependent on accurately capturing the effects of small-scale velocity gradients on the statistics of relative dispersion at small time and small initial separation.

Figure 5.7 shows the standard deviation of pair separation distance σ_r as well as the separation speed flatness factor for the test case. Pair separation speed is defined by $u_r = \mathbf{r} \cdot \mathbf{w}/r$ where $\mathbf{w}$ is the relative velocity between the two particles. The ensemble tracked with spline interpolation has behavior close to the results of Yeung & Borgas [49] (albeit with a different forcing scheme than the one used in that work). Differences introduced by the linear interpolation scheme appear to be readily noticeable only at $r_0/\eta \leqslant 1$. The standard deviation of pair separation distance departs from ballistic t^2 scaling until $t \approx \tau_\eta$. This error, representing an artificial initial growth in the pair separation distance, is due to the increased number of pairs with large separation speeds introduced by the linear interpolation scheme. This is shown by the wider tails of the PDF of separation speed at the first available time instant. By $t \gg \tau_\eta$, the differences have become negligible.

These results are due to the non-differentiability of the piecewise linear velocity field underlying the linear interpolation scheme. For particle pairs located near grid points with local maximum or minimum velocity, splines have small rates of changes near these points. The corresponding relative velocities are small since relative velocities of narrowly-separated particles are approximated by velocity gradients between them. However, a piecewise linear reconstruction are peaked at the nearest grid point to this pair. The slope of the linear element is greater than the gradient of the spline. Hence, the relative velocities are greater.

5.4 Summary

The mean exit time through fixed thresholds of particle pair separation distance demonstrates better scaling according to the diffusion model of Richardson[12] (Equation 5.3 and 5.4) and similarity hypotheses of Kolmogorov 1941 than the inverse third moment does. The PDF of exit time has tails consistent with the Richardson diffusion equation, but the core of this PDF does not follow such simple model relations. The solution to this diffusion equation using $K_p \sim r^{4/3}$ (Equation 5.4) allows us to estimate Richardson's proportionality constant g for t^3 mean-square pair separation scaling to the same order as the cube-local-slope method. However, ambiguities due to intermittency and the limitations of the diffusion model introduce uncertainties that are peculiar to exit times and are not

shared by inferences from more conventional statistics.

Substantial work remains to discern universal features in moments of exit time, especially the inverse third moment $\langle T_\rho^{-3} \rangle = C_{r,-3} \langle \varepsilon \rangle r^{-2}$. Preliminary analysis of the PDF of exit time suggests that separation speed plays a critical role in determining if the conditions of Kolmogorov similarity theory are approached by a given ensemble of particle pairs or not. Linear interpolation, used by other workers in this field, does not significantly alter these results, but does introduce errors in small-time relative dispersion at small initial separations.

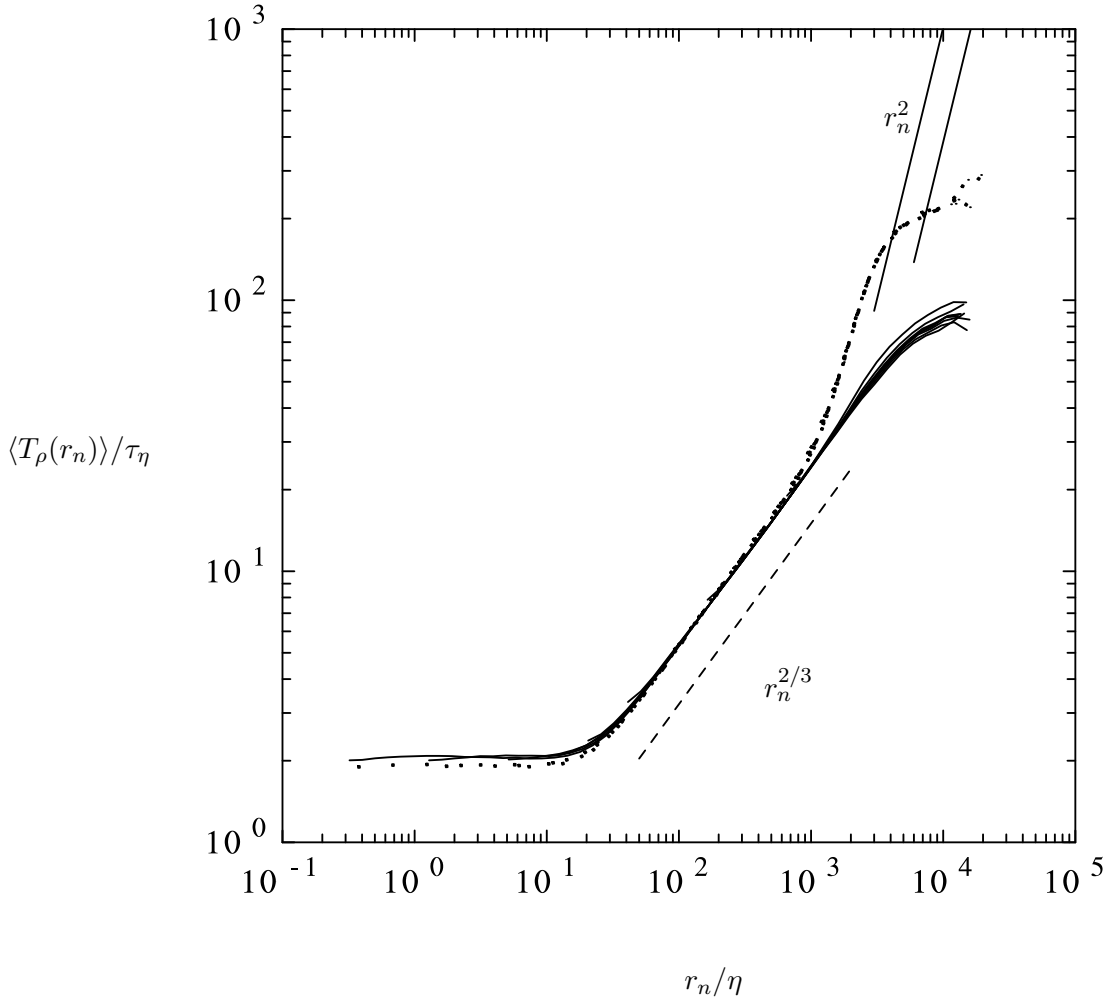

Figure 5.1: Mean exit time at $\rho = 1.25$ for the simulation at $R_\lambda \approx 390$ (dots) and 650 (solid curves). Dashed line is for inertial-range scaling $\langle T_\rho \rangle \sim r^{2/3}$. Solid lines are the independent-motion limits in Equation 5.9 for $R_\lambda \approx 390$ and 650. Initial separation r_0/η from Table 3.1 and increases to the right.

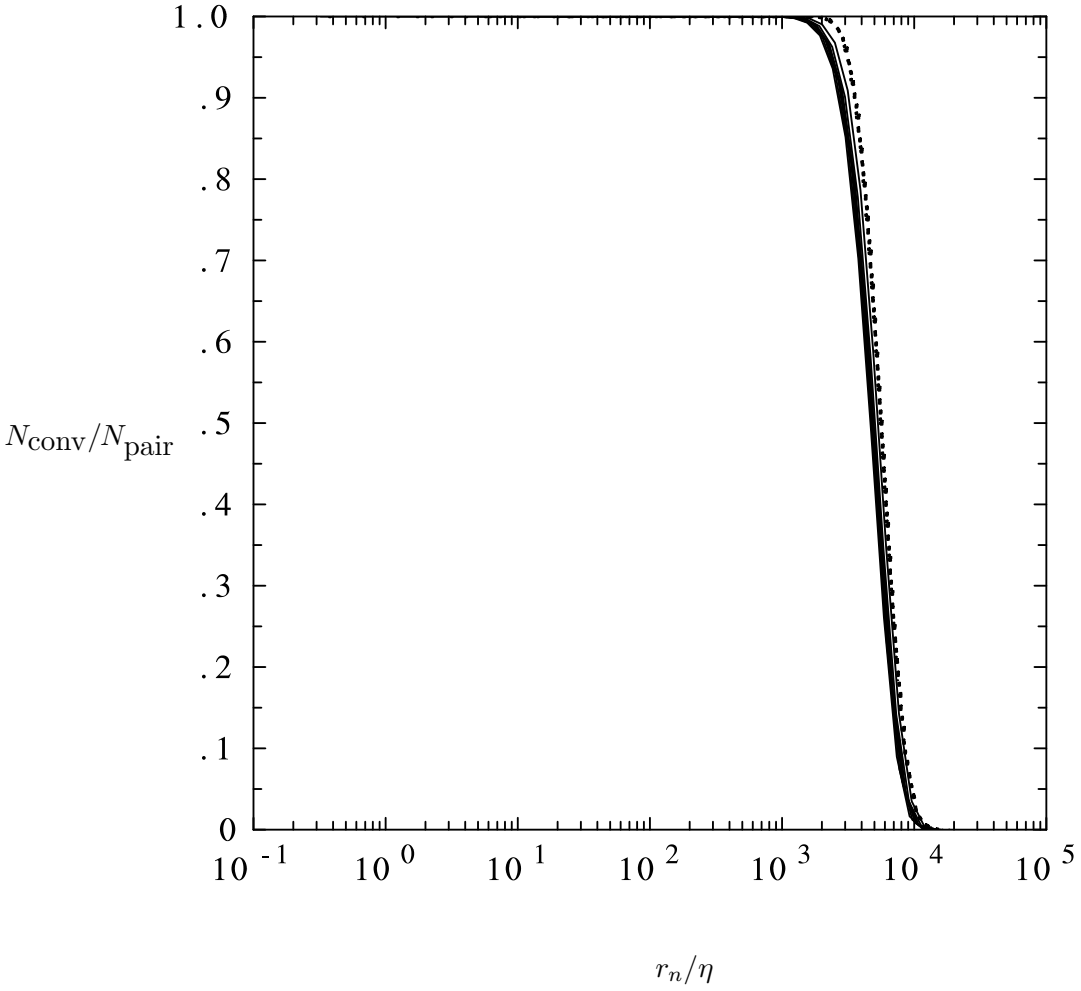

Figure 5.2: Fraction of particle pairs crossing both thresholds of exit events of increasing r_n for the simulations at $R_\lambda \approx 390$ (dots) and 650 (solid curves). Initial separation r_0/η from Table 3.1 and increases to the right.

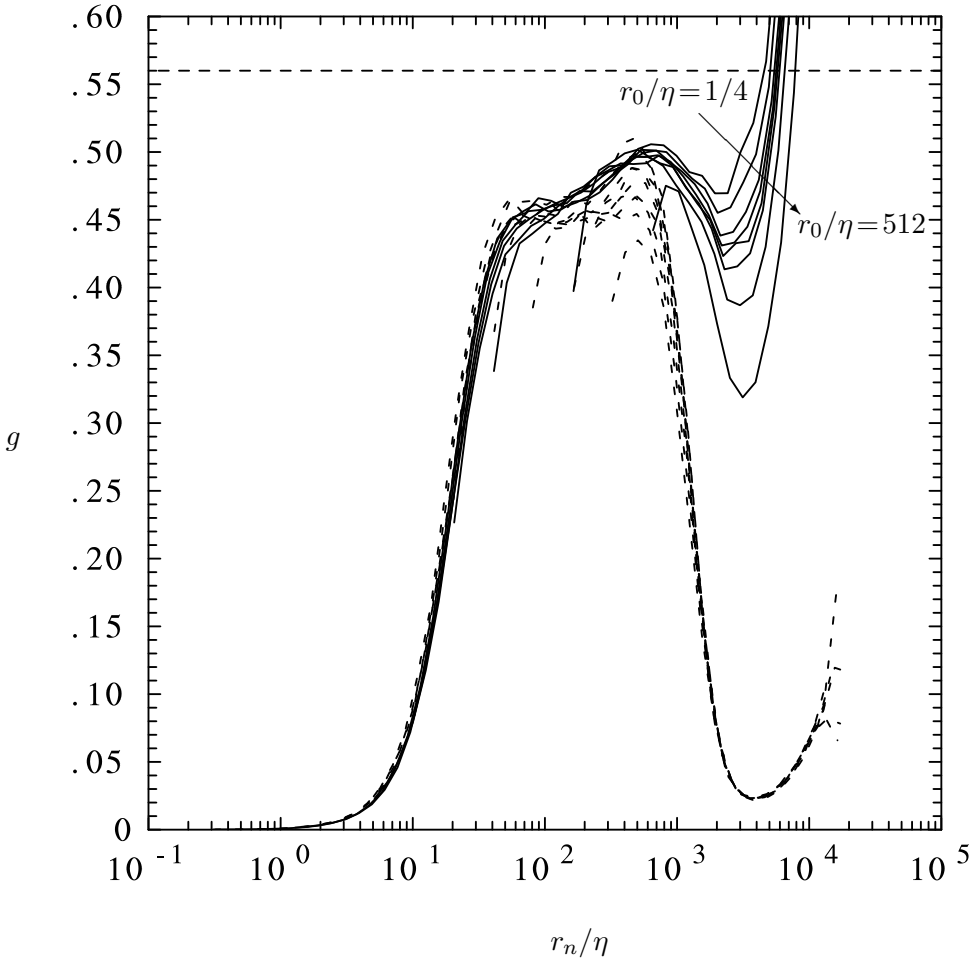

Figure 5.3: Estimate for Richardson's constant g from mean exit time using Equation 5.8 from the simulations at $R_\lambda \approx 390$ (dashed curves) and 650 (solid curves). A dashed line is placed at the observed valued of $g \approx 0.56$ in Chapter 3. Initial separation r_0/η from Table 3.1 and increases to the right. Arrow indicates increasing initial separation at $R_\lambda \approx 650$ in the unconverged regime if thresholds at $r_n/\eta > 1000$.

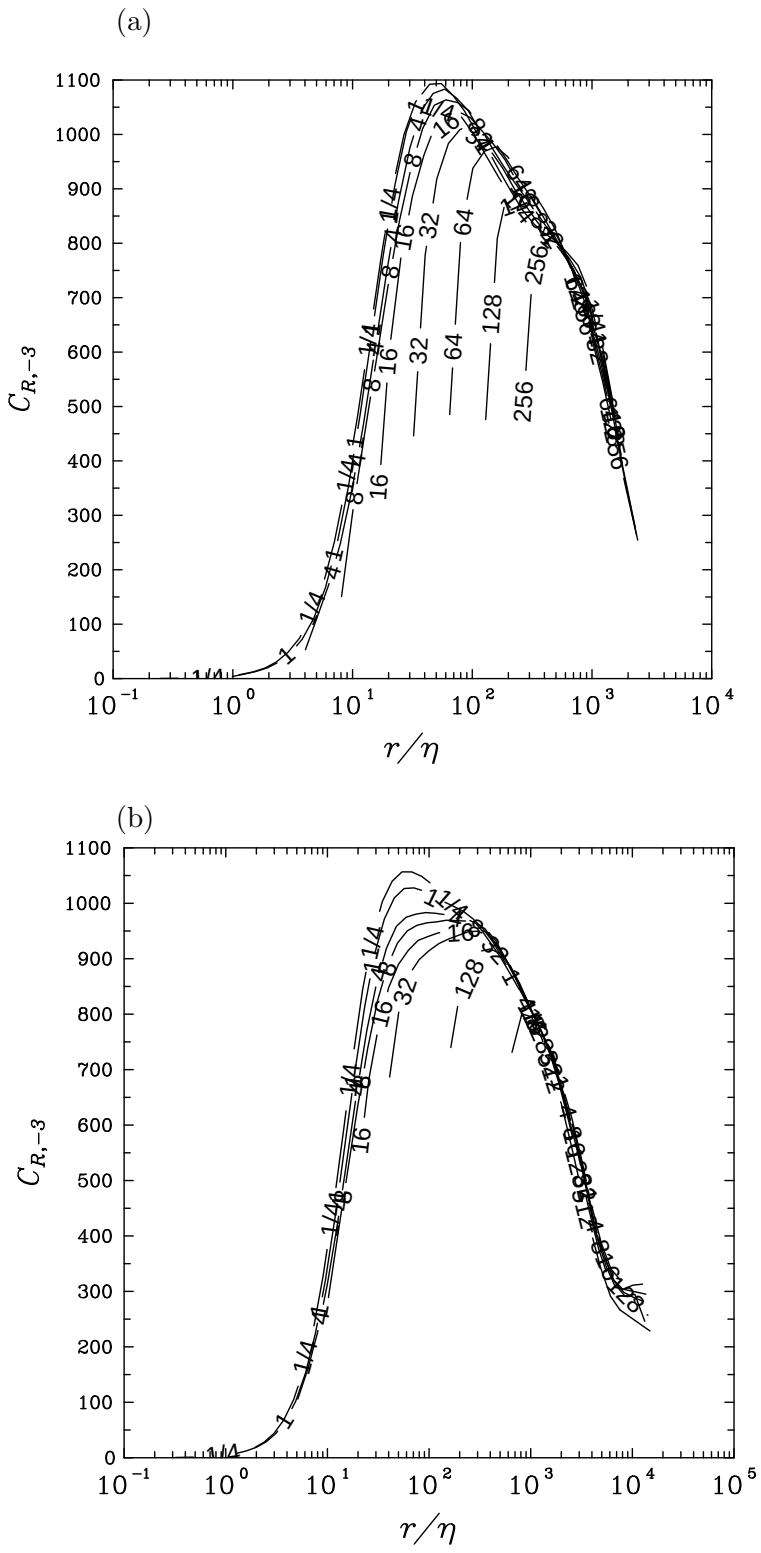

Figure 5.4: Third moment of inverse exit time ($p = -3$ in Equation 5.10) at two values R_λ. a: $R_\lambda \approx 390$. b: $R_\lambda \approx 650$. Both plots have curves labeled by their initial separation r_0/η. $\rho = 1.25$ for both cases.

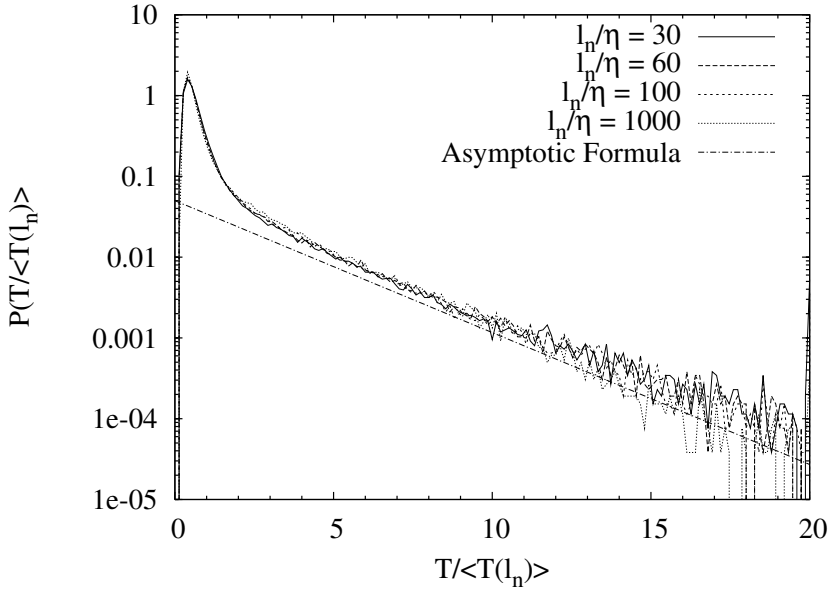

Figure 5.5: PDF of mean-normalized exit time at $R_\lambda \approx 390$, $r_0/\eta = 16$, $\rho = 1.25$. The straight line is Equation 5.12.

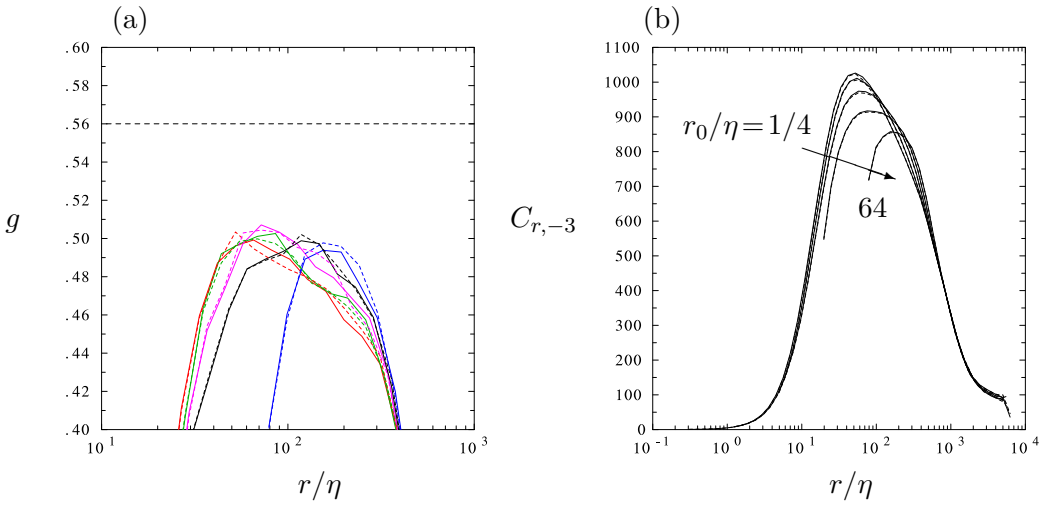

Figure 5.6: Results for exit time at $\rho = 1.25$ for the interpolation test at $R_\lambda \approx 235$. Solid curves are for spline interpolation, dashed curves are for linear interpolation. a: Derived estimate of Richardson's constant g from mean exit time using Equation 5.8. The dashed line at $g = 0.56$ is the fixed-time observation of g from the mean-square pair displacements in Chapter 3. Colors denote $r_0/\eta = 1/4$ (red), 1 (green), 4 (magenta), 16 (black) and 64 (blue). b: Third moment of inverse exit time ($p = -3$ in Equation 5.1). Initial separation ($r_0/\eta = 1/4, 1, 4, 16, 64$) increases to the right in both plots, with an arrow pointing towards larger r_0/η in (b).

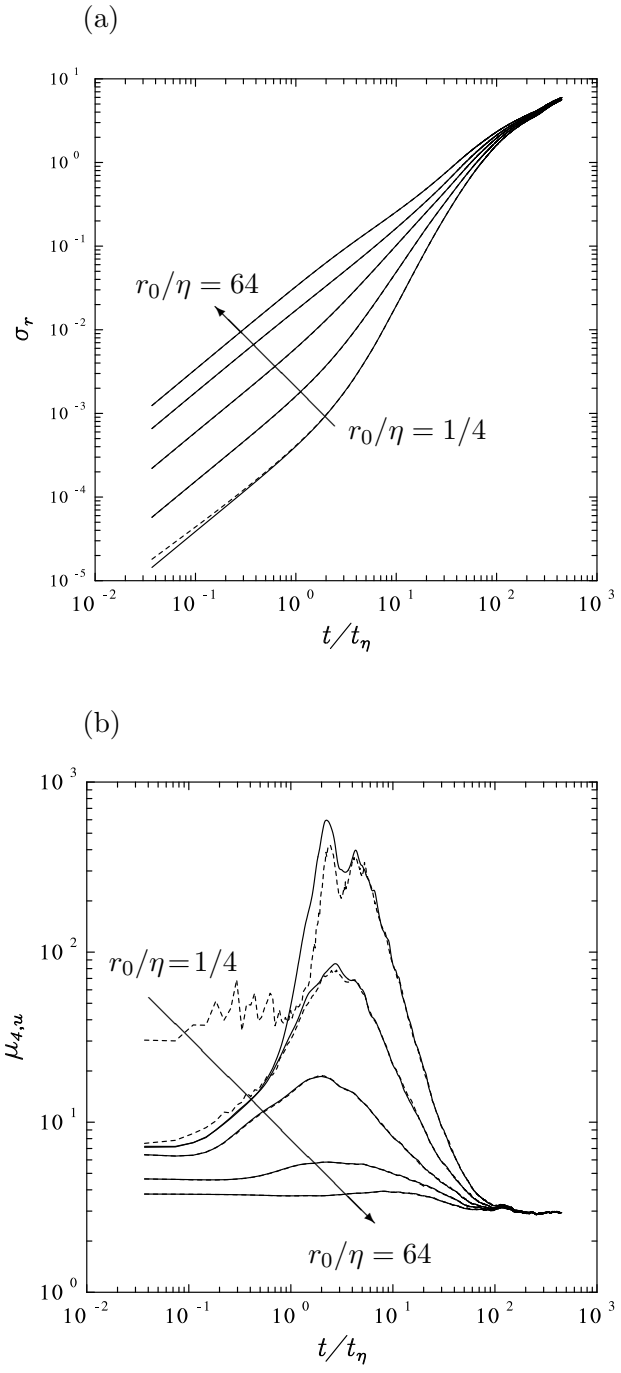

Figure 5.7: Effect of interpolation scheme on relative dispersion at $R_\lambda \approx 235$. Solid curves are for spline interpolation, dashed curves are for linear interpolation. a: Standard deviation of pair separation distance σ_r at (from bottom to top) $r_0/\eta = 1/4$, 1, 4, 8, 16 and 64. b: Flatness factor of separation speed $\mu_4 = \langle (u_r - \langle u_r \rangle)^4 \rangle / \sigma_{u_r}^4$ at (from top to bottom) $r_0/\eta = 1/4$, 1, 4, 8, 16 and 64. Arrows point towards increasing initial separation.

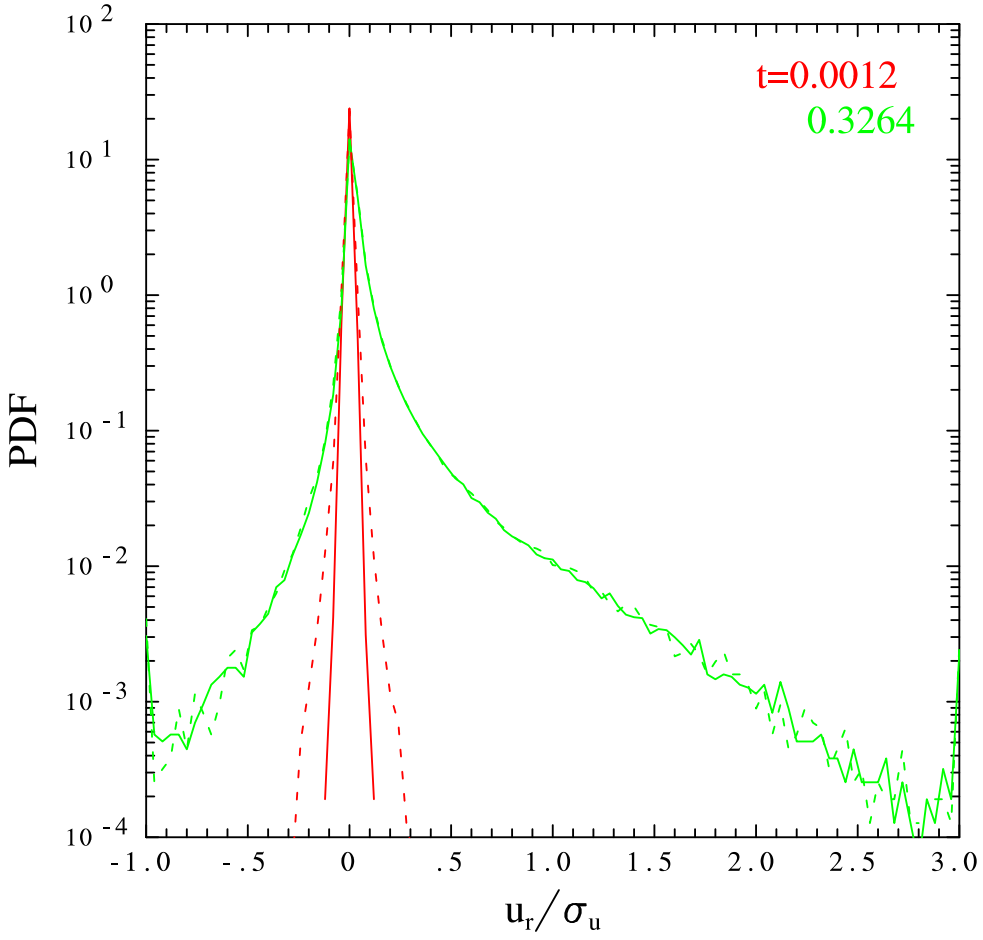

Figure 5.8: PDF of separation speed u_r normalized by one-component r.m.s. velocity at the first available output time (red) and $t/\tau_\eta = 10$ (green) in the interpolation test case at $R_\lambda \approx 235$. Solid curves are for spline interpolation, dashed curves are for linear interpolation.

CHAPTER VI

CONCLUSIONS

This thesis has covered current results from a database of direct numerical simulations over a decade of Taylor-scale Reynolds number and their contributions to the search for universality in turbulent relative dispersion. The largest and most recent simulations have required the development and testing of pipeline algorithms to partition the particles over a large number of processing elements and parallelize the cubic spline method used to interpolate particle velocities. In this chapter we summarize the findings of this thesis and identify open questions and directions for future research.

6.1 Findings

We have reviewed the challenging demands on scale separation encountered in tests of Kolmogorov's hypotheses, which, when applied to the mean-square pair separation distance $\langle r^2 \rangle$, predict the cubic time dependence expressed by the Richardson-Obukhov law $\langle r^2 \rangle = g\langle\varepsilon\rangle t^3$. The cube-local-slope method of differentiating the $\langle r^2 \rangle^{1/3}$ with respect to time has been useful in clarifying observations of t^3 scaling during intermediate times and initial separation distances consistent with the postulate of the inertial subrange. Such analysis, when carried out for the highest Reynolds number ($R_\lambda \approx 1000$) available in the database, refines estimates of Richardson's constant ($g \approx 0.56$) previously obtained by observations of relative displacements. The scalings observed at very small time (in the ballistic regime) and very late time (in the diffusive regime) are also consistent with the universal predictions of Batchelor [16] and Taylor [11], respectively. The slow transitions out of the ballistic regime and into the diffusive regime have been identified as scale cross-over effects that obscure the inertial subrange, but diminish at high Reynolds number.

The distortion of clusters of three and four particles (triangles and tetrads, respectively) is quantified by the eigenvalues of a moment-of-inertia-like matrix whose product may be

related to the ratio $\Lambda = V^{2/3}/R^2$. Statistics of these quantities are invariant during intermediate time intervals, and we associate this invariance with inertial subrange scaling. These regimes of invariance are more readily observed than unambiguous intervals of t^3 scaling in cluster size parameters such as the mean-square gyration radius $\langle R^2 \rangle$, even appearing in incipient form for clusters initialized in the dissipation subrange. For triangles, these statistics (as well as statistics of alternate shape parameters derived from the singular value decomposition of the moment-of-inertia matrix) are also insensitive to differences in initial shape. This is further evidence that universal inertial subrange scaling of the shapes of multiparticle clusters is more robust than it is for the spatial extent of the clusters. We find that turbulence has a tendency to flatten and elongate multiparticle clusters in the inertial subrange, with little preference for or against symmetry. Inertial subrange distortion is less severe than it is in the dissipation subrange.

We have also presented the results of an effort to reduce the interference from very large and very small scales on statistics in the inertial subrange through the use of the exit time of particle pairs between fixed thresholds of pair separation r_{n-1} and $r_n = \rho^n r_0$. There is a wide regime of distinct scaling in the mean exit time $\langle T_\rho \rangle$ that is very close to predictions consistent with the Kolmogorov 1941 similarity hypotheses; it is almost completely independent of initial separation. Furthermore, there is very little effect due to the Reynolds number, which mostly determines the width of the inertial subrange in $\langle T_\rho \rangle$. These universal features systematically depart from Kolmogorov predictions slightly, interfering with our ability to infer g from $\langle T_\rho \rangle$ through model assumptions of a scale-dependent diffusion process in the inertial subrange.

The departure of the inverse third moment $\langle T_\rho^{-3} \rangle$ from the predictions of Kolmogorov similarity theory cause particular concern since they are, in principle, analogous to the Richardson-Obukhov law and free from intermittency. Furthermore, they should not suffer from scale contamination effects like dispersion statistics expressed as functions of time do. Unlike the mean exit time, $\langle T_\rho^{-3} \rangle$ increases with inertial subrange r_n for some initial separations and decrease for others. This variation occurs in different ways for different values of R_λ, making inference of universal inertial subrange scaling even more difficult for

$\langle T_\rho^{-3} \rangle$ than it is for $\langle r^2 \rangle$. Differences in the dynamics of rapidly-separating pairs and slowly-separating pairs (whose exit times through inertial subrange thresholds actually approach scaling corresponding to Richardson's [12] diffusion equation) are possible reasons for the observed departure of $\langle T_\rho^{-3} \rangle$ from Kolmogorov similarity behavior.

The simulation reported by Biferale *et al.* [56] had results for $\langle T_\rho^{-3} \rangle$ more consistent with Kolmogorov scaling at initial separations comparable to the ones used in this thesis, but it was not run long enough to truly approach the diffusive regime at asymptotically late time. Additionally, they used linear interpolation to obtain particle velocities. We tested linear interpolation against spline interpolation for conditions at $R_\lambda \approx 240$ using resolution comparable to that used by Biferale *et al.* [56]. Interpolation scheme did not have an appreciable effect on the results for moments of exit time, but did introduce substantial errors in the ballistic regime of dissipation-range particle pairs.

6.2 Discussion and future work

Although we have successfully applied the pipeline method introduced in Chapter 2 to simulations involving millions of particles on tens of thousands of CPU cores, substantial work in improving the performance and scaling of these methods remains. The failure of the pipelines to overlap communication with computation as permitted by the MPI standard is of great concern. Direct memory access is expected to be a crucial technology for the sort of point-to-point communication used here, and the methodology discussed in §2.2.4 needs development to exploit improvements in the networking architecture of supercomputers.

The results presented in Chapter 3 constitute a reinforcement of the applicability of the Kolmogorov 1941 similarity hypotheses to relative dispersion. Should the case for universal inertial-subrange scaling in moments of pair separation distance become stronger with further simulations and measurements, conditions in which it is observed could be identified in relative dispersion with improved confidence. The range of Reynolds numbers in this thesis can be used to identify trends that could be expected to continue to higher Reynolds numbers. One result consistent with Kolmogorov (1941) phenomenology is the emergence of an inertial subrange in $\langle r^2 \rangle$, even at smaller r_0/η that do not have Batchelor

scaling in the ballistic regime $t \ll t_0$ (Equation 3.15), at higher Reynolds number. The tendency towards this scaling is associated with the increase in the maximum value of the cubed local slope of $\langle r^2 \rangle$ (Equation 3.9) for the smaller values of r_0/η that did not have an unambiguous plateau or inflection point in Figure 3.5. The maximum value of CLS($\langle r^2 \rangle$) is shown as a function of R_λ for $r_0/\eta \leqslant 4$ in Figure 6.1. There are some uncertainties at $R_\lambda \approx 235$ ($r_0/\eta = 4$) and $R_\lambda \approx 390$ ($r_0/\eta = 1/4$) that could be related to the variability of the forcing scheme or the lower number of tetrads used in these particular simulations (Table 3.2), but the notable feature of convergence towards $g \approx 0.56$, which appears as a horizontal dotted line in Figure 6.1, is not obscured by these irregularities in the data. It would not be unreasonable to suppose that CLS($\langle r^2 \rangle$) could reach $g \approx 0.56$ for all three of these initial separations in DNS at $R_\lambda \approx 1500$, adding evidence of inertial range scaling in a size statistic to the incipient inertial-range scaling observed in the shape statistics at dissipation-range r_0/η in Chapter 4 (Figure 4.9).

As stated in Chapter 4, the clear statistical invariance of quantities related to tetrahedron shape is associated with inertial subrange scaling. Choosing the moment-of-inertia tensor's normalized eigenvalues (Equation 4.4) as examples of a statistical measure of tetrahedron shape, and letting Δt_{I_2} represent the interval during which $\langle I_2 \rangle$ is within 2% of its inertial subrange value of 0.16 (Table 4.3), we show the growth of the plateaus in $\langle I_2 \rangle$ with $T_L/t_0 \sim$ in Figure 6.2. Consistent with the results of Chapter 4 (§4.2.1), $r_0/\eta = 16$ represents the widest inertial subrange at multiple Reynolds numbers in our simulations. The linear scaling of Δt_{I_2} with T_L/t_0 is only meant for guidance and rough comparison. Larger initial separations $r_0/\eta > 16$ do not support the idea of a linear growth rate in the width of the inertial subrange plateau with T_L/t_0, but this may be an effect of insufficient Reynolds number at larger initial separations. Since, at high R_λ, $T_L/\tau_\eta \propto R_\lambda$ [50] and $t_0/\tau_\eta = (r_0/\eta)^{2/3}$ (Equation 3.8), T_L/t_0 is expected to grow linearly with R_λ for a fixed r_0/η. We expect the width of the inertial subrange $\Delta t_{I_2}/t_0$ to be proportional to T_L/t_0 as well, a result supported at only $r_0/\eta = 16$ in Figure 6.2.

The Batchelor time is an additional time scale for the dispersion process, and T_L/t_0 is an additional scale ratio that must be large ($T_L/t_0 \sim O(10^1)$ or larger [37]) for an inertial

subrange to exist for relative dispersion. Since shape statistics have been found to present inertial subrange features more readily than size statistics in this thesis [64], the existence of statistical invariance in I_2 only for those cases (R_λ and r_0/η) with $T_L/t_0 > 10$ further reinforces our interpretation of statistical invariance as inertial subrange scaling.

The low-order moments of pair separation distance r (such as $\langle r^2 \rangle$ in this thesis) are still not as well-understood as comparable single-particle and Eulerian statistics; thus, detailed statistical structure of r requires further research to test and scrutinize competing claims about the probability density function of r and the dynamical processes controlling it. How well a diffusion equation like Equation 5.3 applies to inertial subrange relative dispersion is still not well-understood [60], and even the choice of diffusivity [12, 16] is not a settled question. Alternate stochastic models of the dispersion process, notably Lévy flight [92, 93] have not been tested by DNS as much as more conventional diffusion models have been. Further improvement in observed inertial range scaling in the mean-square pair separation distance would permit more detailed examination of the statistical structure of relative velocity and separation speed.

There are very few results, theories or models (with the notable exception of the coarse-grained velocity gradient tensor model of turbulent straining due to Chertkov *et al.* [23]) for the shapes that turbulence imposes on multiparticle clusters. The reasons for clearer inertial subrange scaling encountered in statistics of distortion parameters like Λ and the normalized eigenvalues of the moment-of-inertia in Chapter 4 are still only partially understood, and existing distinctions between descriptions of cluster "shape" and cluster "size" are incomplete. Though cumbersome, extending the singular value decomposition in Equation 4.2 to clusters of four or more particles and computing the statistics of the corresponding Euler angles would represent progress in this direction. Finally, statistics of the moment-of-inertia-like tensor for clusters of more than four particles could establish a hierarchy of multiparticle statistics as the number of particles in a cluster is increased. It is expected that the information added by successive particles diminishes as an asymptotic limit is approached; if so, a finite number of particles could be used to model the behavior of clouds of

arbitrary numbers of particles. Although the results on triangles have shown inertial subrange independence from initial shape, the distortion and strain due to turbulence would be better understood by examining ballistic-regime dispersion of tetrads and triangles with a wide range of initial shapes. The rates at which volume and area grow for initially planar tetrahedra and initially collinear triangles (respectively) could be related to the strain field and stagnation point structure of the turbulence [94, 95].

We have encountered many unexpected challenges in our work in exit times of pair separation distance across fixed thresholds of length in Chapter 5. The mean exit time remains the only statistic the improves upon the mean-squared separation distance in its ability to approach inertial range scaling in some interval of fixed thresholds for a wide range of initial separations and Reynolds numbers. The inverse third moment scaling constant $C_{r,-3}$ has proved to be more difficult to measure than Richardson's constant, and we have established that this difficulty is not exacerbated or ameliorated by different choices of interpolation scheme. The spacing threshold ρ needs to be a widely-varied parameter. It is possible that different choices of ρ could moderate the influence of extremely rapidly-separating pairs on $\langle T_\rho^{-3} \rangle$, and scaling laws like Equation 5.1 may have additional constraints on ρ or some as-yet unidentified measure of separation speed to satisfy the conditions of inertial range scaling in inverse moments of exit time.

We close with a brief description of future work in related topics that could benefit from the findings in this thesis. First, it would be interesting to consider more ways to use a tetrahedron made up of fluid particles as a dynamic region in which to study turbulence at scales smaller than the gyration radius R of the tetrahedron. Chertkov *et al.* [23] (and others) extended the Cantwell's [96] model for velocity gradients to a "coarse-grained" velocity gradient tensor defined based on the differences between the velocities of the four particles in a tetrahedron taken pairwise. In addition to further tests of this model, it would be interesting to use Lagrangian tetrahedra as configurations for other statistical measurements. An important topic in research on intermittency in turbulence is the scaling of the local average $\varepsilon_r = \int_V \epsilon \, d\mathbf{r}$ of the instantaneous energy dissipation rate ϵ over a volume V characterized by linear dimension r. Under the refined similarity hypotheses of

Kolmogorov [97, 98], the n^{th} moment of the local average of dissipation,

$$\langle \varepsilon_r^n \rangle \langle \epsilon \rangle^n \propto \left(\frac{r}{L} \right)^{-\nu_n} , \tag{6.1}$$

is expected to scale with r raised to the power $-\nu_n$, where ν_n is a universal constant related to the fractal dimension of turbulent structures of scale r [3, 99]. It would be interesting to average the Eulerian field of dissipation rate ϵ over the volume of a tetrad of particles and treat the result as a local average of dissipation rate ε_R. Should $\langle \varepsilon_R \rangle$, ensemble-averaged over many such tetrads, exhibit power-law scaling with increasing gyration radius R, it would be interesting to compare the scaling exponents of $\langle \varepsilon_R \rangle$ to ν_n observed for more conventional statistics obtained from averaging over volumes fixed in space (cubes, spheres, etc.). This would show the effect of "sweeping" of tetrahedra by scales larger than their gyration radius on local averages of the Eulerian field encased within them. Sensitivity of $\langle \varepsilon_R \rangle$ to the shapes (parameterized by Λ) of the tetrahedra used to compute it could also improve understanding of filter anisotropy in large eddy simulation (LES).

In the introduction we motivated the study of fluid particles by noting their connection to the Eulerian statistics of admixtures in turbulence. We have also made used the notion of a "cloud" of particles to illustrate several features of turbulent dispersion. In this work, fluid particles have been materially indistinguishable from the fluid treated as a continuum from the Eulerian point of view. Yet contaminants in turbulent flows frequently consist of dispersed phases of liquids and solid particles that are moved around by the flow, but not at the Eulerian velocity. Their positions are integrated according to the top of Equation 2.10, but they have finite mass, and an additional equation [100] for their acceleration under the action of the Eulerian velocity field of the carrier fluid (which imposes drag on the particle) must be solved. The inertia of a particle is parameterized by the Stokes number,

$$S_t = \tau_p / \tau_\eta, \tag{6.2}$$

where τ_p is a particle response time scale, and the density ratio $\beta = 3\rho / (2\rho_p + \rho)$ for particle density ρ_p (see [41] and the works cited therein). Even neglecting body forces, particle collisions and wake effects on the carrier flow velocity field (thus considering only very dilute

mixtures), the statistical dynamics of such particles are dependent on regimes of S_t and β. There are preferential concentrations of inertial particles in turbulent flows that distinguish them from fluid particles, and light particles ($\beta = 3$, resembling very small gas bubbles in a liquid medium) cluster onto very different geometric configurations (possibly fractal sets [101, 102]) from heavy particles ($\beta = 0$, resembling fine sprays of liquid in a carrier gas) [103]. The relative motion of inertial particles is a frontier in turbulence research, and, compared to the relative dispersion of fluid particles, there is little understanding of what form the mean-squared pair separation distances would be consistent with Kolmogorov 1941 phenomenology at a given S_t and β [104, 105]. Recent simulations by Bec *et al.* [106] has identified a rich structure for ballistic-regime dispersion of heavy particles, and further investigation of the inertial subrange structure would benefit greatly from larger-scale simulations at higher Reynolds numbers.

The computational power of current and emerging supercomputers holds great promise in this field. Only recently have we become more comfortable with the oldest and simplest theoretical predictions about relative dispersion, and simulations have played a crucial role in this development. They will continue to do so if the methods used to track particles and the analytical techniques used to understand the statistical character of particle trajectories continue to improve.

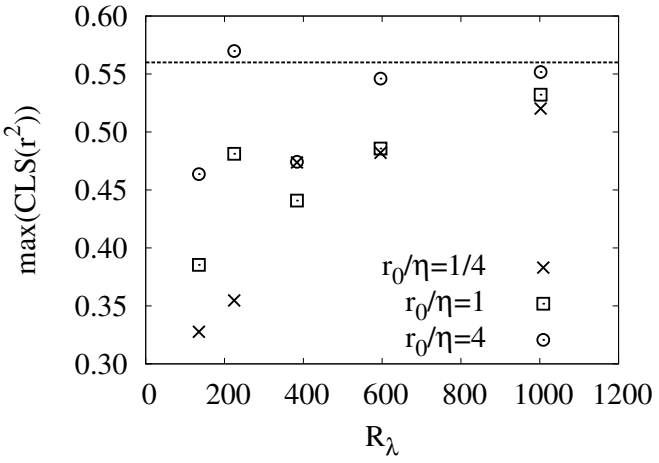

Figure 6.1: Maximum value attained by the cube-local-slope of $\langle r^2 \rangle$ at dissipation-range initial separations as a function of R_λ. The horizontal line indicates the inferred value of Richardson's constant $g \approx 0.56$.

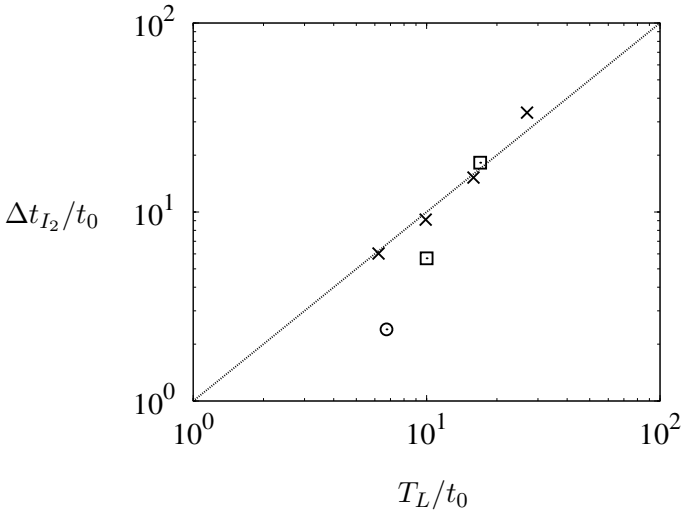

Figure 6.2: Batchelor-scaled width Δt_{I_2} of the plateau defined to be the time interval during which $\langle I_2 \rangle$ is within $\pm 2\%$ of 0.16, the value identified with inertial subrange scaling in Table 4.3. Symbols represent $r_0/\eta = 16$ at $235 \leqslant R_\lambda \leqslant 1000$ ($\times$), $r_0/\eta = 32$ at $650 \leqslant R_\lambda \leqslant 1000$ ($\square$), and $r_0/\eta = 128$ at $R_\lambda \approx 1000$ ($\odot$). Straight line at $\Delta t_{I_2}/t_0 \propto T_L/t_0$ represents large-R_λ limit of scaling in the inertial subrange at a given r_0/η.

APPENDIX A

REYNOLDS NUMBER DEPENDENCE OF RELATIVE DISPERSION STATISTICS IN ISOTROPIC TURBULENCE

B. L. Sawford, P. K. Yeung, and J. F. Hackl. *Physics of Fluids* **20**, 065111 (2008).

Abstract

Direct numerical simulation results for a range of relative dispersion statistics over Taylor-scale Reynolds numbers up to 650 are presented in an attempt to observe and quantify inertial subrange scaling and, in particular, Richardson's t^3 law. The analysis includes the mean-square separation and a range of important but less-studied differential statistics for which the motion is defined relative to that at time $t = 0$. It seeks to unambiguously identify and quantify the Richardson scaling by demonstrating convergence with both the Reynolds number and initial separation. According to these criteria, the standard compensated plots for these statistics in inertial subrange scaling show clear evidence of a Richardson range but with an imprecise estimate for the Richardson constant. A modified version of the cube-root plots introduced by Ott and Mann [J. Fluid Mech. **422**, 207 (2000)] confirms such convergence. It has been used to yield more precise estimates for Richardson's constant g which decrease with Taylor-scale Reynolds numbers over the range of $140 - 650$. Extrapolation to the large Reynolds number limit gives an asymptotic value for Richardson's constant in the range $g = 0.55 - 0.57$, depending on the functional form used to make the extrapolation.

APPENDIX B

MULTI-PARTICLE AND TETRAD STATISTICS IN NUMERICAL SIMULATIONS OF TURBULENT RELATIVE DISPERSION

J. F. Hackl, P. K. Yeung, and B. L. Sawford. *Physics of Fluids* (2011) (*in press*).

Abstract

The evolution in size and shape of three and four-particle clusters (triangles and tetrads, respectively) in isotropic turbulence is studied using direct numerical simulations at grid resolution up to 4096^3 and Taylor-scale Reynolds numbers from 140 to 1000. A key issue is the attainment of inertial range behavior at high Reynolds number, while the small- and large-time limits of ballistic and diffusive regimes, respectively, are also considered in some detail. Tetrad size expressed by the volume (V) and (more appropriately) the gyration radius (R) is shown to display inertial range scaling consistent with a Richardson constant close to 0.56 for two-particle relative dispersion. For tetrads of initial size in a suitable range moments of shape parameters, including the ratio $V^{2/3}/R^2$ and normalized eigenvalues of a moment-of-inertia-like dispersion tensor, show a regime of near-constancy which is identified with inertial-range scaling. Sheet-like structures are dominant in this period, while pancakes and needles are more prevalent at later times. For triangles taken from different faces of each tetrad effects of the initial shape (isosceles right-angled or equilateral) are retained only for about one Batchelor time scale. In the inertial range there is a prevalence of nearly isosceles triangles of two long sides and one short side, representing one particle moving away from the other two which are still close together. In general, measures of shape display asymptotic scaling ranges more readily than measures of size. With some caveats, the simulation results are also compared with the limited literature available for multiparticle cluster dispersion in turbulent flow.

REFERENCES

[1] V. Eswaran and S. B. Pope. An examination of forcing in direct numerical simulations of turbulence. *Comput. and Fluids*, 16:257–278, 1988.

[2] D. A. Donzis and P. K. Yeung. Resolution effects and scaling in numerical simulations of passive scalar mixing in turbulence. *Physica D*, 239:1278–1287, 2010.

[3] U. Frisch. *Turbulence: the legacy of A. N. Kolmogorov*. Cambridge University Press, Cambridge, U. K., 1995.

[4] P. A. Davidson. *Turbulence: An Introduction for Scientists and Engineers*. Oxford University Press, New York, 2004.

[5] A. N. Kolmogorov. Local structure of turbulence in an incompressible fluid for very large Reynolds numbers. *Dokl. Akad. Nauk. SSSR*, 30:299–303, 1941.

[6] A. Bennett. *Lagrangian Fluid Mechanics*. Cambridge University Press, New York, 2006.

[7] B. L. Sawford. Turbulent relative dispersion. *Annu. Rev. Fluid Mech.*, 33:289–317, 2001.

[8] S. Corrsin. Theories of turbulent dispersion. In *Mécanique de la turbulence*, pages 27–52, Coll. Intern. du CNRS á Marseille, 1962. Éd. CNRS.

[9] A. S. Monin and A. M. Yaglom. *Statistical Fluid Mechanics*, volume II. MIT Press, Cambridge, MA, 1975.

[10] P. K. Yeung. Lagrangian investigations of turbulence. *Annu. Rev. Fluid Mech.*, 34:115–142, 2002.

[11] G. I. Taylor. Diffusion by continuous movements. *Proc. Lond. Math. Soc. Ser. 2*, 20:196, 1921.

[12] L. F. Richardson. Atmospheric diffusion shown on a distance-neighbour graph. *Proc. R. Soc. Lond., Ser. A*, 110:709–737, 1926.

[13] J. L. Lumley. Theories of turbulent dispersion. In *Mécanique de la turbulence*, pages 17–26, Coll. Intern. du CNRS á Marseille, 1962. Éd. CNRS.

[14] G. K. Batchelor. Diffusion in a field of homogeneous turbulence. I. Eulerian analysis. *Aust. J. Sci. Res.*, 2:437–450, 1949.

[15] S. Corrsin. Heat transfer in isotropic turbulence. *J. Appl. Phys.*, 23:113–118, 1952.

[16] G. K. Batchelor. Diffusion in a field of homogeneous turbulence. II. The relative motion of particles. *Proc. Camb. Phil. Soc.*, 48:345–362, 1952.

[17] D. J. Thomson. A stochastic model for the motion of particle pairs in isotropic high-reynolds-number turbulence, and its application to the problem of concentration variance. *J. Fluid Mech.*, 210:113–153, 1990.

[18] M. S. Borgas and B. L. Sawford. A family of stochastic models for two-particle dispersion in isotropic homogeneous stationary turbulence. *J. Fluid Mech.*, 279:69–99, 1994.

[19] O. A. Kurbanmuradov and K. K. Sabelfeld. Stochastic Lagrangian models of relative dispersion of a pair of fluid particles in turbulent flows. *Monte Carlo Meth. App.*, 1:106–136, 1997.

[20] A. G. Lamorgese, S. B. Pope, P. K. Yeung, and B. L. Sawford. A conditionally cubic-Gaussian stochastic Lagrangian model for acceleration in isotropic turbulence. *J. Fluid Mech.*, 582:423–448, 2007.

[21] S. B. Pope. Lagrangian PDF methods for turbulent flows. *Annu. Rev. Fluid Mech.*, 26:23–63, 1994.

[22] U. Frisch, A. Mazzino, A. Noullez, and M. Vergassola. Lagrangian method for multiple correlations in passive scalar advection. *Phys. Fluids*, 11:2178–2186, 1999.

[23] M. Chertkov, A. Pumir, and B. I. Shraiman. Lagrangian tetrad dynamics and the phenomenology of turbulence. *Phys. Fluids*, 11:2394–2410, 1999.

[24] L. Mydlarski, A. Pumir, B. I. Shraiman, E. D. Siggia, and Z. Warhaft. Structures and multipoint correlators for turbulent advection: predictions and experiments. *Phys. Rev. Lett.*, 81:4373–4376, 1998.

[25] A. Celani and M. Vergassola. Statistical geometry in scalar turbulence. *Phys. Rev. Lett.*, 86:424–427, 2001.

[26] A. Pumir, B. I. Shraiman, and M. Chertkov. The Lagrangian view of energy transfer in turbulent flow. *Europhys. Lett.*, 56:379–385, 2001.

[27] A. M. Obukhov. Spectral energy distribution in a turbulent flow. *Izv. Akad. Nauk SSSR, Ser. Geogr. Geofiz.*, 5:453–466, 1941.

[28] M. S. Borgas. The multifractal Lagrangian nature of turbulence. *Phil. Trans.: Phys. Sci. and Eng.*, 342:379–411, 1993.

[29] P. Julian, W. Massman, and N. Levanon. The TWERL experiment. *Bull. Am. Meteorol. Soc.*, 58:936–948, 1977.

[30] M. Arhan, A. C. de Verdiére, and H. Mercier. Direct observations of the mean circulation at 48° N in the Atlantic Ocean. *J. Phys. Oceanography*, 19:161–181, 1989.

[31] M. Ollitrault, C. Gabillet, and A. C. de Verdiére. Open ocean regimes of relative dispersion. *J. Fluid Mech.*, 533:381–407, 2005.

[32] J. P. L. C. Salazar and L. R. Collins. Two-particle dispersion in isotropic turbulent flows. *Annu. Rev. Fluid Mech.*, 41:405–432, 2009.

[33] J. Er-El and R. L. Peskin. Relative diffusion of constant-level balloons in the southern hemisphere. *J. Atmos. Sci.*, 38:2264–2274, 1981.

[34] F. Pasquill and F. B. Smith. *Atmospheric Diffusion.* Ellis Horwood, Chichester, UK, 3rd edition, 1983.

[35] S. Ott and J. Mann. An experimental investigation of the relative diffusion of particle pairs in three-dimensional turbulent flow. *J. Fluid. Mech.*, 422:207–223, 2000.

[36] G. A. Voth, A. La Porta, A. M. Crawford, J. Alexander, and E. Bodenschatz. Measurement of particle accelerations in fully developed turbulence. *J. Fluid. Mech.*, 469:121–160, 2002.

[37] M. Bourgoin, N. T. Ouellette, H. Xu, and E. Bodenschatz. The role of pair dispersion in turbulent flow. *Science*, 311:835–838, 2006.

[38] N. T. Ouellette, H. Xu, M. Bourgoin, and E. Bodenschatz. An experimental study of turbulent relative dispersion models. *New J. Phys.*, 8:1–23, 2006.

[39] B. Lüthi, S. Ott, and J. Mann. Lagrangian multi-particle statistics. *J. Turbulence*, 8(45):45, 2007.

[40] G. A. Voth, A. La Porta, A. M. Crawford, E. Bodenschatz, C. Ward, and J. Alexander. A silicon strip detector system for high resolution particle tracking in turbulence. *Rev. Sci. Instrum.*, 72:4348–4353, 2001.

[41] F. Toschi and E. Bodenschatz. Lagrangian properties of particles in turbulence. *Annu. Rev. Fluid Mech.*, 41:375–404, 2009.

[42] P. Moin and K. Mahesh. Direct numerical simulation: a tool in turbulence research. *Annu. Rev. Fluid Mech.*, 30:539–578, 1998.

[43] J. J. Riley and G. S. Patterson. Diffusion experiments with numerically integrated isotropic turbulence. *Phys. Fluids*, 17:292–297, 1974.

[44] P. K. Yeung. Direct numerical simulation of two-particle relative diffusion in isotropic turbulence. *Phys. Fluids*, 6:3416–3428, 1994.

[45] A. Pumir, B. I. Shraiman, and M. Chertkov. Geometry of Lagrangian dispersion in turbulence. *Phys. Rev. Lett.*, 85:5324–5327, 2000.

[46] M. Yokokawa, K. Itakura, A. Uno, T. Ishihara, and Y. Kaneda. 16.4-Tflops direct numerical simulation of turbulence by a Fourier spectral method on the Earth Simulator. In *Supercomputing '02: Proceedings of the 2002 ACM/IEEE conference on Supercomputing*, pages 1–17, Los Alamitos, CA, USA, 2002. IEEE Computer Society Press.

[47] P. K. Yeung, S. B. Pope, and B. L. Sawford. Reynolds number dependence of Lagrangian statistics in large simulations of isotropic turbulence. *J. Turbulence*, 7(58):58, 2006.

[48] J. O. Hinze. *Turbulence.* McGraw-Hill, New York, 2nd edition, 1975.

[49] P. K. Yeung and M. S. Borgas. Relative dispersion in isotropic turbulence. Part 1. Direct numerical simulations and Reynolds-number dependence. *J. Fluid Mech.*, 503:93–124, 2004.

[50] B. L. Sawford, P. K. Yeung, and J. F. Hackl. Reynolds number dependence of relative dispersion statistics in isotropic turbulence. *Phys. Fluids*, 20:065111, 2008.

[51] V. I. Tatarskii. Radiophysical methods of investigating atmospheric turbulence. *Izv. Vyssh. Uchebn. Zaved. Radiofisix*, 4:551–583, 1960.

[52] S. R. Hanna, G. A. Briggs, and S. Else. Handbook of Atmospheric Diffusion. *Tech. Rep. DE82002045*, U.S. Dept. of Energy, U. S. Dept. of Commerce, Springfield, VA, 1982.

[53] P. K. Yeung and S. B. Pope. Lagrangian statistics from direct numerical simulations of isotropic turbulence. *J. Fluid. Mech.*, 207:531–586, 1989.

[54] http://www.top500.org, 2011.

[55] T. Ishihara and Y. Kaneda. Relative dispersion of a pair of fluid particles in the inertial subrange of turbulence. *Phys. Fluids*, 14:L69–L72, 2002.

[56] L. Biferale, G. Boffetta, A. Celani, B. J. Devenish, A. Lanotte, and F. Toschi. Lagrangian statistics of particle pairs in homogeneous isotropic turbulence. *Phys. Fluids*, 17:115101, 2005.

[57] G. Boffetta and I. M. Sokolov. Relative dispersion in fully developed turbulence: The Richardson's law and intermittency corrections. *Phys. Rev. Lett.*, 88:1–4, 2002.

[58] V. Artale, G. Boffetta, A. Celani, M. Cencini, and A. Vulpiani. Dispersion of passive tracers in closed basins: Beyond the diffusion coefficient. *Phys. Fluids*, 9:3162–3171, 1997.

[59] G. Boffetta and I. M. Sokolov. Statistics of two-particle dispersion in two-dimensional turbulence. *Phys. Fluids*, 14:3224–3232, 2002.

[60] B. L. Sawford. A study of the connection between exit-time statistics and relative dispersion using a simple Lagrangian stochastic model. *J. Turbulence*, 7(13):13, 2006.

[61] P. Castiglione and A. Pumir. Evolution of triangles in a two-dimensional turbulent flow. *Phys. Rev. E*, 64:056303, 2001.

[62] L. Biferale, G. Boffetta, A. Celani, B. J. Devenish, A. Lanotte, and F. Toschi. Multi-particle dispersion in fully developed turbulence. *Phys. Fluids*, 17:111701, 2005.

[63] H. Xu, N. T. Ouellette, and E. Bodenschatz. Evolution of geometric structures in intense turbulence. *New J. Phys.*, 10:013012, 2008.

[64] J. F. Hackl, P. K. Yeung, and B. L. Sawford. Multi-particle and tetrad statistics in numerical simulations of turbulent relative dispersion. *Phys. Fluids*, in review, 2011.

[65] P. K. Yeung and S. B. Pope. An algorithm for tracking fluid particles in numerical simulations of homogeneous turbulence. *J. Comp. Phys.*, 79:373–416, 1988.

[66] S. A. Orszag and G. S. Patterson. Numerical simulation of three-dimensional homogeneous isotropic turbulence. *Phys. Rev. Lett.*, 28:76–79, 1972.

[67] R. S. Rogallo. Numerical Experiments in Homogeneous Turbulence. *NASA TM-81315*, page NASA Ames Research Center, 1981.

[68] C. Canuto, M. Y. Hussaini, A. Quarteroni, and T.A. Zang. *Spectral Methods in Fluid Dynamics*. Springer-Verlag, New York, 1988.

[69] G. S. Patterson and S. A. Orszag. Spectral calculations of isotropic turbulence: Efficient removal of aliasing interactions. *Phys. Fluids*, 14:2538–2541, 1971.

[70] S. B. Pope. *Turbulent Flows*. Cambridge University Press, New York, 2000.

[71] M. Snir, S. Otto, S. Huss-Lederman, and D. Walker. *MPI-The Complete Reference: Volume 1, The MPI Core*. MIT Press, Cambridge, MA, 1998.

[72] W. Gropp, E. Lusk, and A. Skjellum. *Using MPI: Portable parallel programming with the message-passing interface*. MIT Press, Cambridge, MA, 2nd edition, 1999.

[73] D. A. Donzis, P. K. Yeung, and D. Pekurovsky. Turbulence simulations on $O(10^4)$ processors. In *TeraGrid '08 Conference*, pages 1–8, Las Vegas, NV, June 2008.

[74] C. deBoor. *A Practical Guide to Splines*. Springer, Berlin, 1994.

[75] http://www.nccs.gov, 2011.

[76] http://www.www.nics.tennessee.edu, 2011.

[77] B. L. Sawford, P. K. Yeung, and M. S. Borgas. Comparison of backwards and forwards relative dispersion in turbulence. *Phys. Fluids*, 17:095109, 2005.

[78] K. R. Sreenivasan. On the universality of the Kolmogorov constant. *Phys. Fluids*, 7:2778–2784, 1995.

[79] P. K. Yeung and Y. Zhou. On the universality of the Kolmogorov constant in numerical simulations of turbulence. *Phys. Rev. E*, 56:1746–1752, 1997.

[80] P. K. Yeung, S. Xu, M. S. Borgas, and B. L. Sawford. Scaling of multi-particle Lagrangian statistics in direct numerical simulations. 2004.

[81] R.M. Johnson. On a theorem stated by Eckart and Young. *Psychometrika*, 28:259–263, 1963.

[82] B. I. Shraiman and E. D. Siggia. Anomalous scaling for a passive scalar near the batchelor limit. *Phys. Rev. E*, 57:2965–2977, 1998.

[83] A. Pumir. Structure of the three-point correlation function of a passive scalar in the present of a mean gradient. *Phys. Rev. E.*, 57:2914–2929, 1998.

[84] A. Celani, M. Cencini, A. Mazzino, and M. Vergassola. Active and passive fields face to face. *New. J. Phys.*, 6 (72), 2004.

[85] P. K. Yeung. Lagrangian characteristics of turbulence and scalar transport in direct numerical simulations. *J. Fluid Mech.*, 427:241–274, 2001.

[86] P. K. Yeung. One- and two-particle acceleration correlations in numerically simulated homogeneous turbulence. *Phys. Fluids*, 9:2981–2990, 1997.

[87] F. Nicolleau and A. ElMaihy. Effect of the Reynolds number on three- and four-particle diffusion in three-dimensional turbulence using kinematic simulation. *Phys. Rev. E*, 74:046302, 2006.

[88] G. Boffetta and A. Celani. Pair dispersion in turbulence. *Physica A*, 280:1–9, 2000.

[89] G. Boffetta, A. Celani, A. Crisanti, and A. Vulpiani. Pair dispersion in fully developed synthetic turbulence. *Phys. Rev. E*, 60:6734–6741, 1999.

[90] C. W. Gardiner. *Handbook of Stochastic Methods: for Physics, Chemistry and the Natural Sciences*. Springer, Berlin, 3rd edition, 2004.

[91] E. A. Novikov. Two-particle description of turbulence, Markov property, and intermittency. *Phys. Fluids A*, 1:326–330, 1989.

[92] J. Klafter, A. Blumen, and M. F. Shlesinger. Stochastic pathway to anomalous diffusion. *Phys. Rev. A.*, 35:3081–3085, 1987.

[93] M. F. Shlesinger, B. J. West, and J. Klafter. Lévy dynamics of enhanced diffusion: application to turbulence. *Phys. Rev. Lett.*, 58:1100–1103, 1987.

[94] J. Dávila and J. C. Vassilicos. Richardson's pair diffusion and the stagnation point structure of turbulence. *Phys. Rev. Lett.*, 91:144501, 2003.

[95] S. Goto and J. C. Vassilicos. Particle pair diffusion and persistent streamline topology in two-dimensional turbulence. *New Journal of Physics*, 6:65, 2004.

[96] B. J. Cantwell. Exact solution of a restricted Euler equation for the velocity gradient tensor. *Phys. Fluids A*, 4:782–793, 1991.

[97] A. N. Kolmogorov. A refinement of previous hypotheses concerning the local structure of turbulence in a viscous incompressible fluid at high Reynolds numbers. *J. Fluid Mech.*, 13:82–85, 1962.

[98] A. M. Obukhov. Some specific features of atmospheric turbulence. *J. Fluid Mech.*, 13:77–81, 1962.

[99] K. R. Sreenivasan and R. A. Antonia. The phenomenology of small-scale turbulence. *Annu. Rev. Fluid Mech.*, 29:435–472, 1997.

[100] M. R. Maxey and J. J. Riley. Equation of motion for a small rigid sphere in a nonuniform flow. *Phys. Fluids*, 26:883–889, 1983.

[101] J. Bec. Fractal clustering of inertial particles in random flows. *Phys. Fluids*, 15:L81–L84, 2003.

[102] J. Bec, L. Biferale, M. Cencini, A. Lanotte, S. Musacchio, and F. Toschi. Heavy particle concentration in turbulence at dissipative and inertial scales. *Phys. Rev. Lett.*, 98:084502, 2007.

[103] E. Calzavarini, M. Kerscher, D. Lohse, and F. Toschi. Dimensionality and morphology of particle and bubble clusters in turbulent flows. *J. Fluid. Mech.*, 607:13–24, 2008.

[104] L. P. Wang and D. E. Stock. Dispersion of heavy particles by turbulent motion. *J. Atmos. Sci.*, 50:1897–1913, 1993.

[105] I. Fouxon and P. Horvai. Separation of heavy particles in turbulence. *Phys. Rev. Lett.*, 100:040601, 2008.

[106] J. Bec, L. Biferale, A. S. Lanotte, A. Scagliarini, and F. Toschi. Turbulent pair dispersion of inertial particles. *J. Fluid. Mech.*, 645:497–528, 2010.